Numerical methods for coupled processes in fractured porous media

Runar Lie Berge

Thesis for the degree of Philosophiae Doctor (PhD)
University of Bergen, Norway
2019

UNIVERSITY OF BERGEN

Numerical methods for coupled processes in fractured porous media

Runar Lie Berge

Thesis for the degree of Philosophiae Doctor (PhD)
at the University of Bergen

Date of defense: 15.11.2019

Year: 2019

Title: Numerical methods for coupled processes in fractured porous media

Name: Runar Lie Berge

Print: Skipnes Kommunikasjon / University of Bergen

Preface

This thesis is submitted as a partial fulfillment of the requirements for the degree of Philosophiae Doctor (Ph.D.) at the University of Bergen. The advisory committee has consisted of Inga Berre (University of Bergen), Eirik Keilegavlen (University of Bergen), and Jan M. Nordbotten (University of Bergen).

The Ph.D. project has been financially supported by the Research Council of Norway, TheMSES project, grant number 250223.

Acknowledgments

There are many who deserve to be thanked at the end of my three years as a Ph.D. student. First and foremost, I would like to thank my three supervisors Inga Berre, Eirik Keilegavlen, and Jan Martin Nordbotten, who have given me indispensable help and guidance. My main supervisor, Inga Berre, has been a source of endless motivation and support throughout my time as a Ph.D. candidate. I am also thankful to my co-supervisor Eirik Keilegavlen for his immense support. His door has always been open, and our many discussions have given me great insight and motivation. Jan Martin Nordbotten's advice and intuition helped me overcome many of the difficult problems I encountered during my research.

I would also like to thank the remainder of the porous media group at the University of Bergen for welcoming me and making my time in the group unforgettable. I am especially grateful to Ivar, with whom I shared an office, many lengthy discussions, and questions, and as he was patiently listening to my complaints when I could not find the bugs in my code. I am also grateful to all my co-authors that have contributed to the papers. The financial support by the Research Council of Norway through the TheMSES project, grant number 250223 is appreciated.

I am also thankful to Barbara Wohlmuth for hosting me at the Technical University of Munich for three months and introducing me to the field of contact mechanics.

Finally, I would like to thank my family and Ingvild who have supported me during the time I spend as a Ph.D. candidate.

Runar Lie Berge
Bergen, August 2019

Abstract

Numerical simulations have become essential in the planning and execution of operations in the subsurface, whether this is geothermal energy production or storage, carbon sequestration, petroleum production, or wastewater disposal. As the computational power increases, more complex models become feasible, not only in the form of more complicated physics, but also in the details of geometric constraints such as fractures, faults and wells. These features are often of interest as they can have a profound effect on different physical processes in the porous medium.

This thesis focuses on modeling and simulations of fluid flow, transport and deformation of fractured porous media. The physical processes are formulated in a mixed-dimensional discrete fracture matrix model, where the rock matrix, fractures, and fracture intersections form a hierarchy of subdomains of different dimensions that are coupled through interface laws.

A new discretization scheme for solving the deformation of a poroelastic rock coupled to a Coulomb friction law governing fracture deformation is presented. The novelty of this scheme comes from combining an existing finite-volume discretization for poroelasticity with a hybrid formulation that adds Lagrange multipliers on the fracture surface. This allows us to formulate the inequalities as complementary functions and solve the corresponding non-linear system using a semi-smooth Newton method.

The mixed-dimensional framework is used to investigate non-linear coupled flow and transport. Here, we study how highly permeable fractures affect the viscous fingering in a porous medium and show that there is a complex interplay between the unstable viscous fingers and the fractures.

The computer code of the above contributions of the thesis work has been implemented in the open-source framework PorePy. The introduction of fractures is a challenge to the discretization and the implementation of the governing equations, and the aim of this framework is to enable researchers to overcome many of the technical difficulties inherent to fractures, allowing them to easily develop models for fractured porous media.

One of the large challenges for the mixed-dimensional discrete fracture matrix models is to create meshes that conform to the fractures, and we present a novel algorithm for constructing conforming Voronoi meshes. The proposed algorithm creates a mesh hierarchy, where the faces of the rock matrix mesh conform to the cells of the fractures, and the faces of the fracture mesh conform to the cells of the fracture intersections.

The flexibility of the mixed-dimensional framework is exemplified by

the wide range of applications and models studied within this thesis. While these physical processes might be fairly well known in a porous medium without fractures, the results of this thesis improves our understanding as well as the models and solution strategies for fractured porous media.

List of papers

A **Reactivation of Fractures in Subsurface Reservoirs – A numerical approach using a static-dynamic friction model**
Runar L. Berge, Inga Berre, Eirik Keilegavlen
In proceedings of European Conference on Numerical Mathematics and Advanced Applications, 25-29 September 2017, Voss, Norway
DOI: 10.1007/978-3-319-96415-7_60

B **Finite volume discretization for poroelastic media with fractures modeled by contact mechanics**
Runar L. Berge, Inga Berre, Eirik Keilegavlen, Jan-Martin Nordbotten, Barbara Wohlmuth
Accepted to International Journal for Numerical Methods in Engineering
DOI: 10.1002/nme.6238

C **Viscous fingering in fractured porous media**
Runar L. Berge, Inga Berre, Eirik Keilegavlen, Jan-Martin Nordbotten
In preparation

D: **PorePy: An Open-Source Software for Simulation of Multiphysics Processes in Fractured Porous Media**
Eirik Keilegavlen, Runar L. Berge, Alessio Fumagalli, Michele Starnoni, Ivar Stefansson, Jhabriel Varela, Inga Berre
Submitted to Computational Geosciences
arXiv:1908.09869 [math.NA]

E: **Unstructured Voronoi grids conforming to lower dimensional objects**
Runar L. Berge, Øystein S. Klemetsdal, Knut-Andreas Lie
Computational Geosciences, volume 23, issue 1, pp 169–188, 2019
DOI: 10.1007/s10596-018-9790-0

Contents

Part I

Background

Chapter 1

Introduction

A porous medium is a material filled with small pores that fluids can flow through. Porous media are found everywhere around us; man-made materials such as concrete or mortars [66] and natural materials such as rocks, soils, and biological tissues [23, 50] can all be considered porous media. While there are many different types of porous media, the main focus of this thesis is on porous media in the form of subsurface fractured rocks. The terminology used in this thesis follows from that. However, even if the focus of this thesis is on fractured rocks, many of the main ideas and contributions can be extended to other applications, and the content should therefore be of interest to a broader audience.

The first section of this chapter motivates the topic of this thesis. The following section list the main contributions of this thesis, while the final section gives an outline of the remainder of the thesis.

1.1 Motivation

The study of fluid flow, transport, and deformation of porous media is of importance to many different subsurface applications, including subsurface energy storage, geothermal systems, oil and gas production, CO_2 storage, and wastewater disposal and management. In all of these applications, mathematical modeling and numerical simulations play an important role when assessing the financial and environmental risks and benefits of different scenarios. Mathematical models can also help us to understand and explain physical processes and direct measurements.

The first mathematical model of fluid flow through a porous medium

was formulated by Darcy [25], and the model describes a single-phase fluid flowing through homogeneous sand. When the first computers became available for scientific computing, the same equation was solved on a grid consisting of tens or so grid cells. In the decades that followed, the computational resources underwent a revolutionary change. Today, the state of the art simulations can solve three-dimensional (3d) multi-component models with hundreds of millions of grid cells [29]. The growth in computer power has not only increased the feasible number of cells in the computations, but also allowed for more complex features to be included in the models.

One of these features is macroscopic fractures in the porous medium, which over the last three decades have seen an increase in attention. Fractured porous media is of importance in many subsurface applications. Perhaps the most known is hydraulic fracturing, where fluids are injected into shale reservoirs at high pressures in order to create new fractures. This process has allowed for the extraction of shale oil and gas that previously have been inaccessible [7]. Another important subsurface application is enhanced geothermal systems (EGS), where the natural temperature gradient of the earth's crust is utilized to harness the internal energy of the earth. In EGS, cold water is pumped into the geothermal reservoir and hot water retrieved. The reservoirs used for EGS are typically naturally highly fractured, however, the permeability is usually very low. In order to achieve economically viable flow rates, the reservoir must be stimulated. A common stimulation technique is low-pressure hydraulic stimulation that induces shear slip of the fractures. This result in a dilation of the fracture aperture, which increases the effective permeability of the reservoir [84]. The drawback is that the stimulation process may cause seismic activity [22, 63], and concerns about the damage caused by seismicity have caused the shutdown of EGS projects [26]. In addition to producing energy from subsurface reservoirs, it has been proposed to use permeable layers such as saline aquifers or depleted oil and gas reservoirs to store energy. Hot fluids are then injected at elevated pressures during spikes in the energy production, and the energy can be retrieved at a later time. This is seen as a possible solution to compensate the energy production spikes that will occur as the fraction of renewable energy sources increases.

Development of mathematical models and simulations tools is important for engineering of all subsurface resources; see e.g., [80]. Numerical simulations can help answer key questions that can increase the efficiency and evaluate the risk of subsurface operations. Common for the examples mentioned above is that flow in and deformation of fractures play impor-

tant roles for the processes of interest. Fractures may form the main flow paths through the reservoir, and it is important to include them in the model to get the correct hydraulic and thermal properties of the reservoir. Further, the fractures are not only static constraints that affect the fluid flow through the reservoir, but the fractures are also evolving. Including fractures in the numerical simulations thus introduces several challenges: First of all, fractures may have large aspect ratios, the aperture is typically on the order of millimeters, while the fracture lengths can span hundreds of meters [10, 91], which makes them difficult to represent numerically. Secondly, the properties and/or physical processes in the fractures are often (very) different from those in the surrounding rock matrix. The permeability in the fractures can be orders of magnitude higher than in the rock matrix, or if the fractures contains sediments, they can block the fluid from crossing them [57]. In some cases both highly conductive fractures and blocking fractures can exist in the same domain, which requires robust numerical methods [33, 24, 34, 79]. Further, fractures act as discontinuities for the deformation of the rock as they can open or slide under friction [52, 41]. Thirdly, the physical processes of interest in a fractured porous medium are often nonlinear coupled multiphysics problems, such as interaction between flow, geo-chemistry, and geo-mechanics. Lastly, the geometry of fractures and fracture networks are often complex and dynamic, which must be accounted for in the mesh generation and numerical discretizations.

Due to the reasons mentioned above, developing new mathematical models and numerical schemes for fractured porous media can be a tremendous task. Despite the efforts already given to fractured porous media, the development of reliable numerical methods and simulation tools for fractured porous media remains a formidable challenge. This thesis tackles parts of these challenges by considering three main issues.

The first issue is modeling of fracture deformation in a poroelastic medium. We limit our discussion to the deformation of pre-existing fractures in the form of sliding or opening of fractures, and we do not consider the growth or nucleation of fractures. The major modeling efforts of fractured poroelastic rocks have been given to open fractures [73, 72]. This might be due to the fact that this is a common assumption in hydraulic-fracturing scenarios where the injected fluid pressure is higher than the maximum principle stress. On the other hand, the models of the low-pressure stimulation used for EGS consider fractures under compression, however, the pore-pressure effect on the rock deformation outside the fractures is usually disregarded [96, 67]. Only limited attention is given to

fractured poroelastic rock under compression [38], and we develop a new discretization scheme to solve poroelastic rock deformation coupled to fracture deformation governed by a Coulomb friction law.

The second issue is coupled non-linear flow in fractured porous media. We study unstable displacement processes in the form of viscous fingering, which is related to many important applications in the subsurface. In CO_2 storage, unstable displacement can greatly improve the mixing rates of the CO_2 with water [31], which improves storage security. In high temperature EGS, the viscosity difference between the injected cold water and hot water can be large, which must be considered in the numerical models. Solving the non-linear equations resulting from the unstable displacement in a fractured porous medium requires a robust framework and advanced numerical schemes, which are developed in this thesis.

The third issue is meshing of fractured porous medium. The geometric constraints imposed by fracture networks can be extremely complicated, and in order to simulate realistic domains and fracture networks, a robust meshing algorithm is needed. A new meshing algorithm that creates Voronoi meshes conforming to fractures is presented.

Finally, to solve the governing equations in a porous media one often has to resort to numerical approximations due to complicated geometries and spatially varying parameters. In addition, the processes in the subsurface often give non-linear couplings that must be handled by robust numerical schemes. This has led to a wide range of softwares that are specialized at solving models of porous media, see, e.g., the TOUGH2 [102] family of codes, DuMux [32], MOOSE [39], OpenGeoSys [97], PFLOTRAN [42], Flow123d [20], MRST [61], and PorePy [47]. All methods developed in this thesis project have been implemented and are available in PorePy and MRST.

1.2 Main contributions

The main contributions of this thesis are:

A new finite-volume discretization for coupled poromechanics and contact mechanics. First, Paper A presents an improvement to the estimation of a step-length parameter in an iteration scheme used to solve the inequality constraints resulting from the contact problem with friction in an fractured elastic domain [96]. However, this iteration scheme has several drawbacks, and in order to improve the speed and accuracy of the solution procedure, a new discretization of the problem

is developed and presented in Paper B. More precisely; an existing finite-volume discretization suitable for poroelastic deformation is coupled to Lagrangian multipliers on the fracture interfaces. This allows for solving the Biot equations in the rock matrix coupled to the fracture deformation through a hybrid formulation. The fracture deformation is governed by a nonpenetration condition and a Coulomb-type friction law, which results in a set of inequality constraints. The inequalities are reformulated as complimentary functions, and a semi-smooth Newton method is used to solve the system of equations.

A study of the effect of fractures on viscous fingering. Fractures can act as highly permeable channels through a porous rock, and despite their relative small volumes compared to the rock matrix, the fractures can have a profound effect on the flow paths through the domain. A fundamentally different type of preferential flow path is formed by viscous fingers that might occur when a less viscous fluid is displacing a more viscous fluid. By employing the numerical tools described in Paper D, the interaction of fracture networks and the highly nonlinear viscous fingering is studied in Paper C. We identify the dimensionless numbers governing the behavior of the system, and while clear viscous fingering and fracture flow regimes appear in the limiting cases, the crossover regime shows a complex interaction between the two physical processes.

Open-source code for mixed-dimensional DFM models. The computer code developed in the above contributions is implemented in the open-source software PorePy[1]. The conceptual ideas behind the modeling framework and its realization in form of PorePy is presented in Paper D. Paper D and PorePy is the joint effort of several authors, and this thesis can only take a fraction of the credits. To be specific, the implementations done in PorePy related to this thesis are:

- Improvements, development, and maintenance of the finite-volume discretizations for flow and mechanics.
- Implementation of the contact mechanics module (which has been extended by other authors).
- Implementation of the automatic differentiation module.
- Models for coupled multiphysics models of flow, transport and deformation.
- Post-possessing of the mesh returned from Gmsh (splitting the fracture faces).

[1] https://github.com/pmgbergen/porepy

- Implementing parts of the mortar meshes (mortars between subdomains of equal dimension).
- General code maintenance.

Algorithm for creating conforming Voronoi meshes. In Paper E, new techniques are developed to create unstructured Voronoi meshes conforming to geological structures. Two types of conformity are considered: (i) control-point alignment of the cell-centers to represent, e.g., multilateral wells, and (ii) boundary alignment where the faces of the mesh conform to cells defined by lower-dimensional surfaces (e.g., fractures). The algorithm presented builds the mixed-dimensional mesh (as defined in Chapter 4) from the lowest-dimension to the highest-dimension in such a way that the faces of each consecutive dimension conform to the cells of the lower dimension.

1.3 Outline

This thesis is divided into two parts. Part I is an introduction to the physical models, mathematical formulations, and numerical methods used in Part II. The main scientific contribution is presented in Part II in the form of three papers that are either published or submitted to scientific journals, one peer reviewed book chapter, and one journal article in preparation.

The remainder of Part I is organized as follows:

Chapter 2 gives a brief overview of different conceptual models for fractured porous media, where the main focus is on the mixed-dimensional discrete fracture matrix model that is used in this thesis.

Chapter 3 describes the mathematical equations for fluid flow, transport, and poroelastic deformation in fractured porous media.

Chapter 4 introduces the discretizations of the mathematical models given in Chapter 3.

Chapter 5 gives a summary of each of the papers in Part II and their scientific contributions.

Chapter 2

Conceptual models for fractured porous media

The purpose of a conceptual model is to describe a set of physical processes and/or geometrical structures relevant for a specific purpose and scale of interest. A conceptual model is only an approximation of the reality. However, a model can give important insight in physical processes and allow for representation of the quantity of interest at the scale of interest sufficiently well. The conceptual model defines the framework of the mathematical models, the discretization of the mathematical models, and the implementation in a computer program, thus, the choice of conceptual model must be discussed in light of the complete modeling process.

In this chapter, the most common macroscopic models for a fractured porous medium are described based on the discussion in [28, 89]. After the introduction to the different models, Section 2.2 gives more details on the mixed-dimensional Discrete Fracture Matrix (DFM) model that is used throughout this thesis. The purpose of this thesis is not to describe and develop new conceptual models, and this chapter rather serves as a brief introduction to prepare the reader for the mathematical modeling concepts in Chapter 3 and the discretization in Chapter 4, which both depend on the choice of conceptual model.

2.1 Macro-scale models

The following paragraphs discuss different conceptual models for fractured porous media. For a visual summary, see Figure 2.1.

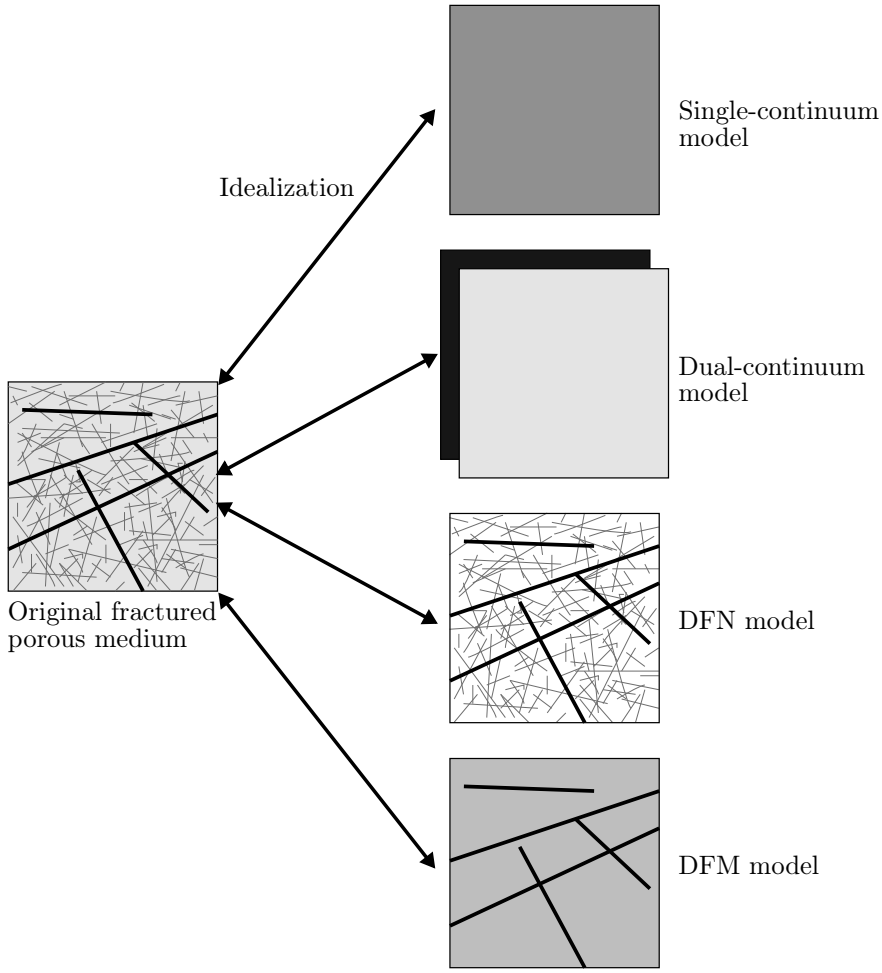

Figure 2.1: Conceptual models of a fractured porous medium. The full complexity of the porous medium is too demanding to resolve. Instead, different idealized models can be used depending on the relative importance of small-scale and large-scale fractures and rock matrix permeability. The figure is adapted from Figure 1.4 in [89]

A porous rock consists of microscopic pores between rock grains and fractures within the rock that allow for fluid flow. Despite the enormous increase in computer power the latest decades, it is not feasible to include an explicit description of micro-scale features in a porous medium, except in some special small-scale cases such as core samples. Moreover, the geometry of the microscopic pore structure is usually not available, and models that require explicit knowledge of the pore-structure would be in vain. Instead, macroscopic models consider the average behavior of the micro-scale features, and the quantity of interest is the upscaled behavior of the medium. This gives rise to continuum models. For fluid flow, the prevalent continuum model reduces the complex structures of a porous medium to a single number (in general a tensor) called the permeability [9]. This conceptual model has been extended to a wide range of applications, such as, inhomogeneous, anisotropic porous media, multi-phase flow, reactions, and transport.

The first attempts to model fractures in a porous medium tried to fit the fractures into the same conceptual model as the rock matrix pore-structure. Similar to the pore-structure, the dynamical processes in the fractures were upscaled and represented as a continuum [8]. For small-scale and poorly connected fracture networks, a single continuum might represent both the flow in the rock matrix and the fractures. However, due to the fundamentally different structures and dynamics in the fractures versus the rock matrix, it is difficult to represent the combined structure with a single continuum. E.g., the time-scale of transport in the fractures can be orders of magnitude different from the time-scale of transport in the rock matrix. For densely populated fracture networks, a better approach is to represent the fractures and rock matrix by different continuum models, where the interaction between the continuum is handled by constitutive interaction laws. This gave rise to the dual-continuum model pioneered by Barenblatt et al. [6]. In order to handle non-isothermal and multiphase flow, the multiple interacting continua (MINC) models were developed [83]. This concept can be further generalized by multi-continuum models that allows for fractures on more than one scale [28].

While the continuum models have been used with great success, they have several drawbacks. First of all, fractures in a porous medium can span all length scales, including the reservoir scale, which makes upscaling of the fractures to a continuum unfeasible. Thus capturing the preferential flow paths defined by macroscopic fractures can be difficult, or even impossible, in standard grid-block numerical models. Secondly, the accuracy of the model is dependent on the upscaling procedure, which can be challenging

for nonlinear flow and complex geometries. This is illustrated by the flow paths of the viscous fingering in the fracture networks presented in Paper C. Thirdly, without an explicit representation of the fractures, it is difficult to model fracture evolution effects; the models for fracture slip and opening presented in Papers A, B, and D are highly dependent on the fracture geometry and the orientation of the fractures in the stressfield.

To overcome some of these problems, a different conceptual model is needed. Instead of considering the averaged behavior of the fractures, fractures are explicitly represented in the model. These models are called discrete fracture models (as opposed to continuum) and come in two main categories. The first is the Discrete Fracture Network (DFN), model where it is assumed that the physical processes in the rock matrix are negligible, and only the fractures are represented [87]. The second model is the Discrete Fracture Matrix (DFM) model, which is a combination of the DFN model and the continuum approach for the rock matrix [76, 28]. In the DFM model, small-scale fractures are typically upscaled into an effective permeability and represented either as a single continuum together with the background permeability of the rock matrix, or as a dual-continuum [81], and the large-scale dominant fractures are represented explicitly in the model.

2.2 Mixed-dimensional DFM model

The work of this thesis is concerned with the macro-scale behavior of fractured porous media, and the conceptual model is chosen with this in mind. We consider a mixed-dimensional DFM model; the small-scale fractures are upscaled into an effective matrix permeability, and the macro-scale fractures are represented explicitly as lower-dimensional surfaces. The effective matrix permeability takes into account both the upscaled small-scale fractures and the background permeability of the pores in the rock matrix. Two assumption are made for the explicitly represented fractures in the mixed-dimensional DFM model; see Figure 2.2. The first assumption is that the microscopic structure of the fractures can be upscaled into effective fracture parameters, and the second assumption is that fractures can be assumed lower-dimensional.

The motivation of the first assumption is similar to how the pore-structure of the rock matrix is upscaled to effective parameters. The structure of a fracture surface is in general not known, in addition, the spatial variation of fracture parameters can be orders of magnitude smaller than the macroscopic scale of interest. As an example of such upscaling, the

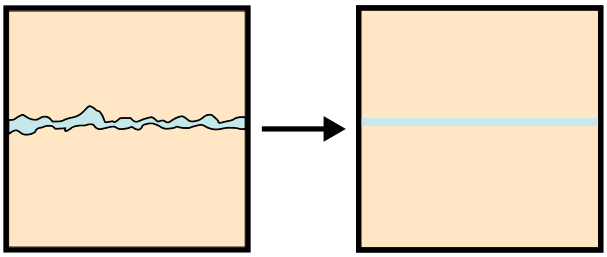

Figure 2.2: A fracture (left) in a mixed-dimensional DFM model (right). The fracture is represented by a lower-dimensional surface (in this case a 1d line in the 2d rock matrix) by integrating the properties in the fracture over the width. The small-scale features of the fracture are upscaled into effective fracture parameters.

fluid flow in the fractures can often be represented by Darcy's law, where the roughness of the fractures (together with potential mineral deposits) is upscaled and represented by an effective permeability [86, 104].

In addition to upscaling the properties of fractures, the dimensionality of the fractures is reduced by the second assumption made in the mixed-dimensional DFM model [35, 85, 79]. The ratio of the length scale of the fractures and the aperture (the width) of the fractures can be orders of magnitude. Resolving the averaged spatial width of the fractures in the computational mesh would require very small cells in and around the fractures, which in most cases would be computational infeasible. Under the assumption that fractures are thin inclusions in the rock matrix, the variability of quantities across a fracture (e.g., the fluid pressure) is approximately constant compared to the lateral variation, thus, it is reasonable to model fractures as lower-dimensional surfaces. The properties represented in the fractures must therefore be considered as integrated over the fracture aperture.

Fractures in a porous medium can intersect in complex patterns which can induce headache to anyone who wish to set up a model, mesh the domain, and discretize the corresponding equations. As an example of some of the difficulties that must be handled, the fracture network in Figure 2.3 has Y-intersections, X-intersections, and T-intersections. For flow and transport, intersections define direct connections between fractures, and it can be crucial to include the connections in the model. A consequence of modeling fractures as lower-dimensional surfaces of co-dimension one with respect to the rock matrix, is that the intersection of two fractures

Figure 2.3: The left figure shows an outcrop of a fractured rock where the length scale of the fractures is tens of meters. The middle figure shows the dominant fractures traced by black lines. The right figure shows a conceptual model of an imagined 3d fractured porous medium. In the conceptual model the rock matrix is 3d, the fractures are 2d surfaces, and the intersections of the fractures are 1d (blue) lines.

is a lower-dimensional inclusion of co-dimension one with respect to the fractures. To illustrate this with an example, consider a fracture network embedded in a 3d rock matrix. In general, the full geometry is described by the 3d rock matrix, 2d surfaces (the fractures), 1d lines (the intersections of the fractures), and 0d points (the intersections of the intersections). We call this structure the mixed-dimensional DFM model.

For many practical applications, the main physical processes are restricted to the rock matrix and the fractures, thus, the 1d lines and 0d points can often be neglected. To some extent, this defines a minimum adaptation of fixed-dimensional models (models where the spatial dimension of all subdomains is the same), and has been a popular choice for flow and transport [65, 46, 88, 19]. However, the lack of representation of the intersection lines often has several drawbacks. In particular, it is difficult to account for the interaction between fractures, especially for fractures with different permeabilities, and in 3d where the intersection geometry can be complicated [92].

In this thesis, the full hierarchy of all dimensions is included. Thus, the mathematical models and equations in the following chapter are formulated for the mixed-dimensional domain of rock matrix, fractures and intersections. Correspondingly, Chapter 4 discusses the meshing and discretization of such domains.

Chapter 3

Mathematical models

Conservation laws form the framework of many physical models and include conservation of mass, conservation of energy, conservation of momentum, and conservation of electric charge. While the conservation principles are fundamental and valid in general, they are often not sufficient to describe the physical process of interest. In addition, constitutive laws and boundary conditions have to be included. The constitutive laws are usually based on experiments and/or simplification of physical processes and valid under certain assumptions. As an example, Darcy's law, presented later in this chapter, is valid for creeping flow in a porous medium; if the flow is faster, other constitutive laws should be used (e.g., the Forchheimer equations [98]).

In the mixed-dimensional DFM model, the rock matrix, the fractures, the intersection of fractures, and the intersections of intersections are all described as separate subdomains. To couple the subdomains together we adapt a mortar technique that was first formulated for domain decomposition methods [12, 11], and proposed used for fractures by Martin et al. [65] and Frih et al. [35]. In the mortar formulation, a mortar domain is associated with each interface, and interface variables on the mortar domain couples different subdomains. In the discrete formulation, the mortar domain is assigned a mesh similarly to the subdomains. Specifically, this allows for non-matching meshes between the different subdomains.

The remainder of this chapter is laid out as follows. First, we discuss the mixed-dimensional geometry and define the different geometric objects and the notation used to label them. In Sections 3.2-3.4, we present the equations describing fluid flow, transport, and poroelasticity in a mixed-dimensional DFM model.

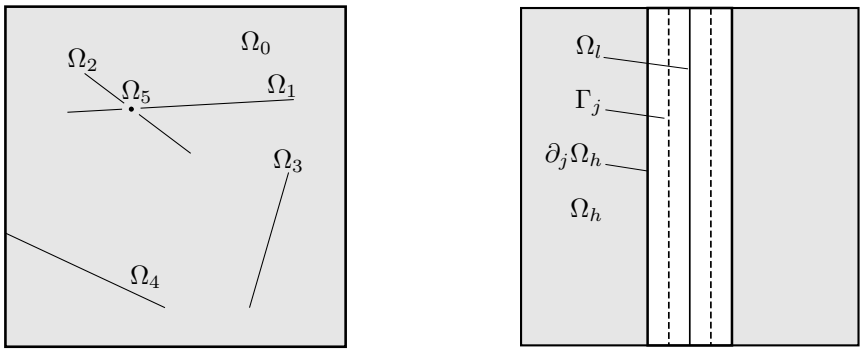

(a) (b)

Figure 3.1: (a) Illustration of a 2d domain containing four fractures and one fracture intersection. (b) Illustration of the interface Γ_j between the lower-dimensional subdomain Ω_l and the higher dimensional subdomain Ω_h. Note that the domain Ω_l, the interface Γ_j, and the boundary $\partial_j\Omega_h$ all coincide geometrically, but they have been offset in the illustration for the purpose of visualization.

3.1 Geometry

Before the mathematical models can be introduced, we present the notation used to describe the geometry of a fractured porous medium, as shown in Figure 3.1. The rock matrix, the fractures, the intersection of fractures, and the intersections of intersections are all described as separate subdomains. A generic subdomain is marked by the subscript i and denoted by Ω_i. A generic interface between two subdomains is denoted Γ_j, identified by the subscript j. When the couplings between subdomains are discussed, the higher-dimensional subdomain is denoted by Ω_h and the-lower dimensional subdomain is denoted by Ω_l. Finally, the part of the boundary of Ω_h that coincides with the interface Γ_j is denoted by $\partial_j\Omega_h$.

In the mathematical models formulated in this chapter, the interaction between subdomains can only happen through an interface. Thus, to describe couplings between two subdomains, we define projection operators between subdomains and interfaces; see Figure 3.2. A projection operator from an interface to a subdomain is denoted by Ξ, and a projection operator from a subdomain to an interface is denoted by Π. The projection operators are given a subscript, j, to indicate the interface and a superscript, i, to indicate the subdomain. The exact construction of the

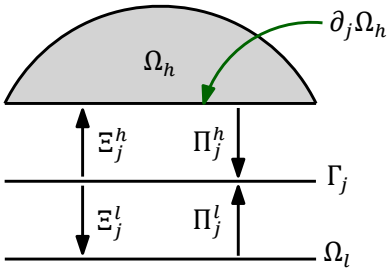

Figure 3.2: Conceptual representation of a higher-dimensional subdomain, Ω_h, a lower-dimensional subdomain, Ω_l and the interface, Γ_j coupling them together. The projection operators Ξ_j^h and Ξ_j^l maps from the interface to the subdomains and the projection operators Π_j^l and Π_j^h maps from the subdomains to the interface. The figure is taken from Paper D

projection operator will depend on the structure of the specific problem. In this thesis we only consider the lowest-order projections, and the discrete construction of the operators can be done by identifying overlapping areas between cells and faces. The actual implementation of the projection needs to consider the nature of the variable to project, being of intensive or extensive kind.

In the continuous case, the projection operators maps variables between different subdomains. Let Ω_l be the lower-dimensional subdomain that coincides with the interface Γ_j, and let $L^2(\Omega_l)$ and $L^2(\Gamma_j)$ be the space of square integrable functions in Ω_l and on Γ_j, respectively. The projection

$$\Xi_j^l : L^2(\Gamma_j) \to L^2(\Omega_l),$$

maps functions on the interface onto the lower-dimensional subdomain. Similarly, when Ω_h is a higher-dimensional subdomain, the mapping

$$\Xi_j^h : L^2(\Gamma_j) \to L^2(\partial_j\Omega_h),$$

maps functions from the interface, Γ_j, onto the part of the boundary of Ω_h that coincides with the interface. The mappings from the subdomains to the interface are denoted by

$$\Pi_j^l : L^2(\Omega_l) \to L^2(\Gamma_j), \quad \Pi_j^h : L^2(\partial_h\Omega_h) \to L^2(\Gamma_j).$$

For the mechanical problem the vectorized version of these operators are needed; the extension is straightforward.

As a final definition, we divide the set of interfaces associated with the subdomain Ω_i into the set of interfaces that map to lower-dimensinal subdomains and the set of interfaces that map to higher-dimensional subdomains. The first set, denoted by $\check{S}_i$, contains the indices j of all the interfaces that are one dimension lower than the subdomain, Ω_i. The second set, denoted by $\hat{S}_i$, contains the indices j of the interfaces that have the same dimension as Ω_i. Thus, for an interface, $\Gamma_j,\ j \in \check{S}_i$, the projection Ξ_j^i maps to the boundary $\partial_j \Omega_i$. And for an interface, $\Gamma_j,\ j \in \hat{S}_i$, the projection Ξ_j^i maps to the domain of Ω_i.

In the following sections, we will use gradients and divergence operators to state the governing equations. The differential operators of a lower-dimensional subdomain should be interpreted as the operators on the tangent space of that subdomain. Similarly, a vector in a lower-dimensional subdomain should be interpreted as the tangential vector of that subdomain.

3.2 Flow

3.2.1 Conservation of mass

The conservation of mass states that the change in mass within a volume $K \subset \Omega_i$ must equal the sum of the fluxes flowing over the boundary ∂K and any sources and sinks within the volume:

$$\int_K \frac{\partial \phi \rho}{\partial t} \,\mathrm{d}V = -\int_{\partial K} \rho \boldsymbol{v} \cdot \boldsymbol{n} \,\mathrm{d}A + \int_K \tilde{q} \,\mathrm{d}V.$$

Here, ϕ is the porosity of the rock, ρ is the fluid density, $\boldsymbol{v}$ is the fluid flux, $\boldsymbol{n}$ is the outwards pointing normal vector, and $\tilde{q}$ is any sources or sinks. By applying the divergence theorem to the surface integral and using that this is valid for any arbitrary volume K, we can remove the integral, and by rearranging the terms write down the strong form of mass conservation

$$\frac{\partial \phi_i \rho_i}{\partial t} + \nabla \cdot \rho_i \boldsymbol{v}_i = \tilde{q}_i \quad \text{in } \Omega_i.$$

The variables are given the subscript i to indicate that they live in the subdomain, Ω_i. In general, both the porosity and density may depend on the fluid pressure, thus, the mass conservation defines a nonlinear parabolic equation.

In the mixed-dimensional setting, the source/sink term $\tilde{q}_l$ of a lower-dimensional subdomain, Ω_l, does not only consist of external sources q_l

(such as a well), but also includes the mass interchange with the higher-dimension. The fluid flux crossing the interface Γ_j is denoted by λ_j and appears as a source term, $\Xi_j^i \rho_j \lambda_j$, in the mass conservation. Recall that a lower-dimensional subdomain, Ω_l, can have multiple interfaces that couple the lower-dimensional subdomain with a higher-dimensional subdomain, and the interfaces are given by the set $\hat{S}_l$. Thus, a sum over all interfaces in this set appears in the conservation of mass:

$$\frac{\partial \phi_l \rho_l}{\partial t} + \nabla \cdot \rho_l \boldsymbol{v}_l - \sum_{j \in \hat{S}_l} \Xi_j^l \rho_j \lambda_j = q_l \quad \text{in } \Omega_l. \tag{3.1}$$

A similar system is formulated for a higher-dimensional subdomain Ω_h, however, the interaction with a lower-dimensional subdomain though an interface flux λ_j now acts as a Neumann boundary condition:

$$\boldsymbol{v}_h \cdot \boldsymbol{n}_h = \Xi_j^h \lambda_j \quad \text{on } \partial_j \Omega_h. \tag{3.2}$$

3.2.2 Constitutive laws

In addition to the mass conservation given by Equation (3.1), constitutive laws are needed. The most famous equation relating fluid flux to the fluid pressure in porous media flow is Darcy's law. Given the permeability $\mathcal{K}_i$ of the porous medium, the viscosity μ_i of the fluid, and the gravitational acceleration $\boldsymbol{g}$, the fluid flux is given by

$$\boldsymbol{v}_i = -\frac{\mathcal{K}_i}{\mu_i}(\nabla p_i - \rho_i \boldsymbol{g}).$$

There are many common assumptions to simplify the mass accumulation term $\partial \phi_i \rho_i / \partial t$ in the mass conservation equation (3.1); if the rock matrix does not deform we can assume that the porosity, ϕ_i, is constant, and for many fluids (including water) the density is approximated by an exponential dependence on the pressure:

$$\rho_i(p_i) = \rho_0 \exp(-c_p(p_i - p_0)), \tag{3.3}$$

where ρ_0 is the density at the reference pressure, p_0, and c_p the fluid compressibility.

Darcy's law and the pressure dependent density are constitutive laws that are typically used for traditional fixed-dimensional problems. In the mixed-dimensional formulation, a constitutive law for the mortar flux, λ_j,

between the higher-dimensional subdomain, Ω_h, and the lower-dimensional subdomain, Ω_l, is also needed. Here, a Darcy type law is used [65]:

$$\lambda_j = -\frac{\mathcal{K}_j}{\mu_j}(\Pi_j^l p_l - \Pi_j^h \text{tr } p_h) \quad \text{on } \Gamma_j, \tag{3.4}$$

where $\mathcal{K}_j$ is the coupling permeability, and tr the trace operator. We have here assumed a regularity of the pressure p_h such that the trace is in L^2. We note that L^2-functions do not necessary have a trace defined, however, for example functions in the space $H^1(\Omega_i)$ do. Thus, the coupling conditions will require a slightly higher regularity of the pressure solution of the mixed-dimensional problems than of the corresponding fixed-dimensional problem. This is related to the Robin-type nature of the coupling conditions [65, 15].

3.2.3 Boundary conditions

To complete the mathematical model of fluid flow in fractured porous media, the mass conservation and constitutive laws must be supplemented by appropriate boundary conditions. The boundary of a subdomain, Ω_i, can be divided into two disjoint subsets. The first subset is the part of the subdomain that coincides with any interface, and the second subset is the part of the boundary that does not. For the first subset, we set a Neumann-type condition given by the mortar flux, λ_j, as defined by Equation (3.2). The second part of the boundary is further divided in the two parts $\partial_v\Omega_i$ and $\partial_p\Omega_i$, for which a Neumann boundary condition and a Dirichlet boundary condition are enforced, respectively:

$$\boldsymbol{v}_i \cdot \boldsymbol{n}_i = g_v \quad \text{on } \partial_v\Omega_i, \quad p = g_p \quad \text{on } \partial_p\Omega_i. \tag{3.5}$$

The boundary of fractures and intersections of fractures may end inside the rock matrix subdomain, e.g., as the right tip of Ω_4 in Figure 3.1. For these boundaries a zero-flux condition is given, i.e., $\boldsymbol{v}_i \cdot \boldsymbol{n}_i = 0$.

3.2.4 The pressure equation

In most of this thesis, we assume that the fluid is either incompressible (ρ is constant), or slightly compressible ($\boldsymbol{v} \cdot \nabla\rho \ll \rho\nabla \cdot \boldsymbol{v}$), neglect gravitational terms, and assume no external sources and sinks. A simplified linear system of equations is then obtained from the mass conservation, the constitutive laws, and the boundary conditions given in the previous sections. For the convenience of the reader, and as a reference later in this thesis, we write

down the complete mixed-dimensional system of equations for fluid flow here. For any subdomain, Ω_i, the mixed-dimensional pressure equation is given by

$$\begin{aligned}
\frac{\partial \phi_i c_p p_i}{\partial t} + \nabla \cdot \boldsymbol{v}_i - \sum_{j \in \hat{S}_i} \Xi_j^i \lambda_j &= 0 && \text{in } \Omega_i \\
\boldsymbol{v}_i + \frac{\mathcal{K}_i}{\mu_i} \nabla p_i &= 0 && \text{in } \Omega_i \\
\lambda_j + \frac{\mathcal{K}_j}{\mu_j} (\Pi_j^i p_i - \Pi_j^h \text{tr } p_h) &= 0 && \text{on } \Gamma_j, \quad \forall j \in \hat{S}_i \\
\boldsymbol{v}_i \cdot \boldsymbol{n}_i &= \Xi_j^i \lambda_j && \text{on } \partial_j \Omega_i, \quad \forall j \in \check{S}_i \\
\boldsymbol{v}_i \cdot \boldsymbol{n}_i &= g_v && \text{on } \partial_v \Omega_i \\
p_i &= g_p && \text{on } \partial_p \Omega_i.
\end{aligned} \tag{3.6}$$

The careful reader who is familiar with different models for flow in fractured porous media might wonder why the fracture aperture does not appear in Equation (3.6). The answer is that it does, but the aperture is included implicitly in the permeability and porosity; see also [13]. Not only does this make the equations much easier to read, it is also consistent with the mixed-dimensional modeling approach where a fracture is considered a true lower-dimensional subdomain and not just a lower-dimensional approximation. While some authors include this explicit dependence on the aperture in the equations [65, 46], we have chosen to suppress it.

3.3 The transport equation

There exist many types of transport processes in a porous medium, e.g., transport of contaminants, transport of energy, and transport of mass. We refer to transport as all processes governed by advective and diffusive processes. Given the fluid flux field $\boldsymbol{v}_i$ and the diffusivity $\mathcal{D}_i$ in the subdomain Ω_i, the conservation of the scalar quantity c_i is given by the conservation equation

$$\frac{\partial \phi_i c_i}{\partial t} + \nabla \cdot (c_i \boldsymbol{v}_i - \mathcal{D}_i \nabla c_i) = \tilde{q}_c \quad \text{in } \Omega_i, \tag{3.7}$$

where $\tilde{q}_c$ is the source/sink term.

The extension to the mixed-dimensional setting follows the same procedure as for the conservation of mass in Section 3.2.1. The diffusive mortar flux β_j of the interface Γ_j between the two subdomains Ω_l and Ω_h is defined

as

$$\Xi_j^h \beta_j = -n_h \cdot \mathcal{D}_h \nabla c_i \quad \text{on } \partial_j \Omega_h.$$

The advective flux across the interface is given by the concentration multiplied by the fluid flux mortar variable, $c_j \lambda_j$. The conservation equation in the subdomain Ω_l is written as

$$\frac{\partial \phi_l c_l}{\partial t} + \nabla \cdot (c_l \boldsymbol{v}_l - \mathcal{D}_l \nabla c_l) - \sum_{j \in \hat{S}_l} \Xi_j^l (c_j \lambda_j + \beta_j) = q_c \quad \text{in } \Omega_l, \tag{3.8}$$

where q_c are external sources or sinks. The concentration on the interface, denoted by c_j, is given by an upstream weighting, which is discussed further in Chapter 4.

Finally, the constitutive law for the diffusive mortar flux β_j is given by

$$\beta_j = -\mathcal{D}_j (\Pi_j^l c_l - \Pi_j^h \text{tr } c_h) \quad \text{on } \Gamma_j.$$

3.4 Poroelasticity

In the flow problem, the conductive property of the fractures is upscaled and represented as Darcy flow in a lower-dimensional subdomain. Similarly, the material properties of fractures can be modeled as thin inclusion (imagine a plate reinforcement in concrete), e.g., as is done in [16]. This might be relevant when modeling faults and the damage zones around faults, or fractures that are consolidated by a mineral. We do not pursuit these effects within this thesis, and the fractures are not given any elastic properties. Thus, the equations defining the deformation of the domain are only defined in the rock matrix, and fractures are considered as the contact of two surfaces. An interface Γ_j is associated with each fracture, and the two sides of the fracture are denoted by $\partial_j^+ \Omega_i$ and $\partial_j^- \Omega_h$. The mappings from the fracture interface to the two sides are defined by

$$\Xi_j^+ : L^2(\Gamma_j) \to L^2(\partial_j^+ \Omega_h), \quad \Xi_j^- : L^2(\Gamma_j) \to L^2(\partial_j^- \Omega_h),$$

and the inverse mappings are given by

$$\Pi_j^+ : L^2(\partial_j^+ \Omega_h) \to L^2(\Gamma_j), \quad \Pi_j^- : L^2(\partial_j^- \Omega_h) \to L^2(\Gamma_j).$$

We decompose a variable on the fracture interface in a normal component and a tangential component, indicated by the subscripts n and τ,

respectively. Given a generic vector variable $\boldsymbol{\xi}$ on Γ_j, the normal component is defined from the outwards pointing normal vector on the positive side of the fracture:

$$\xi_n = \boldsymbol{\xi}_n \cdot \Pi_j^+ \boldsymbol{n}_h \quad \text{on } \Gamma_j. \tag{3.9}$$

The tangential components of the vector variable are defined by

$$\boldsymbol{\xi}_\tau = \boldsymbol{\xi} - \xi_n \Pi_j^+ \boldsymbol{n}_h \quad \text{on } \Gamma_j. \tag{3.10}$$

The displacement in the higher-dimensional subdomain is denoted by $\boldsymbol{u}_h$ and the displacement jump from the positive to the negative side of a fracture, Γ_j, is given by the jump operator $[\cdot]^j$ as

$$[\boldsymbol{u}_h]^j = \Pi_j^+ \text{tr } \boldsymbol{u}_h - \Pi_j^- \text{tr } \boldsymbol{u}_h \quad \text{on } \Gamma_j.$$

Thus, $[\boldsymbol{u}_h]_n^j$ defines the normal opening of the fracture, and $[\boldsymbol{u}_h]_\tau^j$ defines the tangential slip.

3.4.1 Conservation laws

In a poroelastic material, the fluid flow through the pores and the deformation of the rock matrix form a coupled process. The derivation of the poroelastic equations was first done by Biot [14], and a similar model was presented by Terzaghi [94]. See also the textbook by Coussy [23] for an introduction to poroelasticity.

Momentum

We restrict our attention to the case where inertia and gravity effects can be disregarded. The pressure in the pores acts as an isotropic stress, and the effective stress, or Biot stress, is a combination of the Cauchy stress tensor σ_i and the pore pressure:

$$\sigma_i^p = \sigma_i - \alpha_i p_i \mathcal{I} \quad \text{in } \Omega_i,$$

where $\alpha_i \in [0, 1]$ is the Biot-Willis coefficient, p_i the fluid pressure, and $\mathcal{I}$ the second-order identity tensor. The conserved quantity in Biot's theory is the effective stress, and in the rock matrix subdomain, Ω_h, this gives the conservation law

$$\nabla \cdot \sigma_h^p = \mathbf{0} \quad \text{in } \Omega_h. \tag{3.11}$$

A mortar variable λ_j is associated with the fracture interface Γ_j, and the variable represents the contact pressure on the fracture surfaces:

$$\Xi_j^+ \boldsymbol{\lambda}_j = \sigma_h^p \cdot \boldsymbol{n}_h \quad \text{on } \partial_j^+ \Omega_h.$$

Due to Newton's third law, the forces on the negative side of the fracture have to be equal and opposite to the forces on the positive side:

$$\Xi_j^- \boldsymbol{\lambda}_j = -\sigma_h^p \cdot \boldsymbol{n}_h \quad \text{on } \partial_j^- \Omega_h.$$

We have here chosen a mixed formulation where the mortar variable represents the traction on the interfaces. This is similar to how it is done in Paper B. In Paper D a different approach is taken, and the same problem is stated in a primal formulation where the mortar variable represents displacement. For the finite-volume implementation used in the two papers, these two formulations are equivalent up to the nuances in the implementation of Dirichlet and Neumann boundary conditions.

Fluid mass

The fluid mass conservation given by Equation (3.1) is also valid for a poroelastic domain. In the derivation of the pressure Equation (3.6), it was assumed that the porosity of the rock matrix is constant. This is no longer true for a poroelastic domain, and the porosity is in general dependent on the mechanical deformation of the rock matrix. In the linear elastic regime, the change in volume is linearly dependent on the divergence of the deformation. In the rock matrix subdomain Ω_h, this gives the conservation law for the fluid

$$\nabla \cdot \alpha_h \dot{\boldsymbol{u}}_h + c_0 \dot{p}_h + \nabla \cdot \boldsymbol{v}_h = 0 \quad \text{in } \Omega_h,$$

where c_0 is the specific storage term, and the dot represents the time derivative (e.g., $\dot{p}_h = \partial p / \partial t$).

The mass conservation of the fluid in the fractures is dependent on the displacement jump $[\boldsymbol{u}_h]^j$. It is obvious that as the fracture opens, i.e., $[\boldsymbol{u}_h]_n^j < 0$, the volume available for the fluid increases. In Paper A, we also consider so-called shear dilation where the volume available for flow increases when the fracture slides, i.e., $\|[\boldsymbol{u}_h]_\tau^j\| > 0$. In general, the volume might be dependent on a number of other factors as well [58], e.g., the normal traction, but for the purpose of this introduction it is sufficient to specify that the change in volume is a given function, $a([\boldsymbol{u}_h]^j)$, of the displacement jump. The mass conservation in the fracture subdomain Ω_l is then given by

$$\dot{a}([\boldsymbol{u}_h]^j) + c_0 \dot{p}_l + \nabla \cdot \boldsymbol{v}_l - \sum_{j \in \hat{S}_l} \Xi_j^l \lambda_j = 0 \quad \text{in } \Omega_l.$$

Note that the scalar variable λ_j represents the fluid flux between the lower-dimensional fracture and higher-dimensional rock matrix, and the vector variable $\boldsymbol{\lambda}_j$ represents the surface traction on the fracture boundary of the higher-dimensional subdomain.

3.4.2 Constitutive laws

As for the equations of flow and transport, we have to supplement the conservation equations by constitutive laws. We assume that the relation between the stress and the displacement, denoted by $\boldsymbol{u}_i$, can be written as

$$\sigma_i = \mathbb{C}_i : \nabla_s \boldsymbol{u}_i,$$

where $\mathbb{C}_i$ is a fourth-order symmetric positive definite tensor and $\nabla_s \boldsymbol{u}_i = 0.5(\nabla \boldsymbol{u}_i + (\nabla \boldsymbol{u}_i)^\top)$ is the symmetric gradient. A common assumption is that the material is linear elastic and follows an extension of Hook's law:

$$\sigma_i = \mathbb{C}_i : \nabla_s \boldsymbol{u}_i = G_i(\nabla \boldsymbol{u}_i + (\nabla \boldsymbol{u}_i)^\top) + L_i \mathrm{Tr}(\nabla \boldsymbol{u}_i)\mathcal{I},$$

where G_i and L_i are the Lamé parameters, Tr denotes the trace of a tensor, and $\mathcal{I}$ is the second-order identity tensor.

The fluid flow follows the same constitutive laws as given in Section 3.2.2.

Contact problem

Constitutive laws for the fracture deformation are also needed. In this section we give two laws, one in the direction normal to the fracture (denoted by the subscript n as defined by Equation (3.9)), and one in the tangential plane of the fracture (denoted by the subscript τ). The constitutive laws formulated for fracture deformation are adapted from classical textbooks within contact mechanics [51, 100]. For further references see the survey contribution [99] or the references within Paper B.

The first constitutive law for fracture deformation is the nonpenetration condition that says that the two sides of the fractures cannot penetrate each other:

$$[\boldsymbol{u}_h]_n \leq 0, \quad \lambda_{jn} + \Pi_j^l \alpha_l p_l \leq 0, \quad (\lambda_{jn} + \Pi_j^l \alpha_l p_l)[\boldsymbol{u}_h]_n = 0 \quad \text{on } \Gamma_j.$$

Here, Π_j^l is the projection from the lower-dimensional fracture subdomain to the interface that couples the positive and negative fracture sides, thus, $\boldsymbol{\lambda}_{hn} + \Pi_j^l \alpha_l p_l$ gives the effective normal traction on the fracture. The nonpenetration condition says that: (i) the fracture sides cannot penetrate

each other, (ii) there are no cohesive forces, and (iii) if a fracture is open, the contact pressure is given by the fluid pressure inside the fracture:

$$[\boldsymbol{u}_h]_n < 0 \rightarrow \lambda_{jn} + \Pi_j^l \alpha p = 0 \rightarrow \lambda_{jn} = -\Pi_j^l \alpha_l p_l.$$

The second constitutive law for fracture deformation governs the sliding of the fractures; the displacement jump in the tangential plane of the fracture is given by a Coulomb friction law:

$$\begin{cases} \|\boldsymbol{\lambda}_{j\tau}\| \leq -\mu(\lambda_{jn} + \Pi_j^l \alpha_l p_l) & \\ \|\boldsymbol{\lambda}_{j\tau}\| < -\mu(\lambda_{jn} + \Pi_j^l \alpha_l p_l) \rightarrow [\dot{\boldsymbol{u}}_h]_\tau^j = 0 & \text{on } \Gamma_j, \\ \|\boldsymbol{\lambda}_{j\tau}\| = -\mu(\lambda_{jn} + \Pi_j^l \alpha_l p_l) \rightarrow \kappa \in \mathbb{R},\ \kappa^2 \boldsymbol{\lambda}_{j\tau} = -[\dot{\boldsymbol{u}}_h]_\tau^j & \end{cases}$$

which bounds the tangential contact pressure, $\boldsymbol{\lambda}_{j\tau}$, by the coefficient of friction, F, multiplied by the effective normal contact pressure, $\lambda_{jn} + \Pi_j^l \alpha_l p_l$. The second condition says that if the friction bound is not reached, there is no sliding. The third condition says that if the friction bound is reached, the sliding is parallel to the tangential contact pressure. The Coulomb friction is defined according to the sliding velocity $[\dot{\boldsymbol{u}}_h]^j$.

3.4.3 Boundary conditions

On the external boundary of the rock matrix subdomain Ω_h, appropriate boundary conditions must be given. The boundary $\partial\Omega_h$, is divided into the fracture boundary $\partial_j^{\pm}\Omega_h$, and the non-fracture boundary. The contact laws given in Section 3.4.2 and fluid coupling law in Equation 3.4 give the boundary conditions on the fracture boundary, while the non-fracture part of the boundary has to be given two boundary conditions, one for the fluid and one for the deformation. The fluid is given a pressure (on $\partial_p\Omega_h$) or a flux boundary condition (on $\partial_v\Omega_h$), and the mechanics is given a displacement (on $\partial_u\Omega_h$) or a stress boundary condition (on $\partial_\sigma\Omega_h$):

$$\begin{aligned} \boldsymbol{u}_h &= \boldsymbol{g}_u \text{ on } \partial_u\Omega_h, & \sigma_p \cdot \boldsymbol{n}_h &= \boldsymbol{g}_\sigma \text{ on } \partial_\sigma\Omega_h, \\ p_h &= g_p \text{ on } \partial_p\Omega_h, & \boldsymbol{v}_h \cdot \boldsymbol{n}_h &= g_v \text{ on } \partial_v\Omega_h. \end{aligned} \tag{3.12}$$

For the fluid flow, boundary conditions in the lower-dimensional subdomains must also be given according to Equation (3.5).

Chapter 4

Numerical discretization

As mentioned in Chapter 2, the choice of the conceptual model cannot be chosen independently of the mathematical model. Similarly, the choice of the mathematical formulation restricts the choices for the discretization. Further, the computer implementation and the data-structures should also be chosen accordingly. When the conceptual model, mathematical model, discretization, and implementation are consistent, we avoid ad hoc solutions and may obtain a robust framework that allows for extensions to a wide range of physical models.

The mathematical models presented in Chapter 3 all follow the same structure. The fractured porous medium is divided into subdomains (rock matrix, fractures, and intersections), on which standard conservation and constitutive laws for porous media are stated. The interactions between subdomains are represented by mortar variables that act as source terms in the lower-dimensional subdomains and boundary conditions in the higher-dimensional subdomains. In this chapter, we present the discrete versions of the models presented in Chapter 3, and we take advantage of the given mathematical structure. The discretization can be done in two steps. In the first step, standard fixed-dimensional discretizations are used to discretize the conservation equations separately on each of the subdomains, and in the second step the couplings between subdomains are discretized. As long as the fixed-dimensional discretization in the first step can handle source-terms and internal boundary conditions, the coupling becomes a matter of applying the correct projection operators to the mortar variable.

Generating conforming mixed-dimensional meshes can be a formidable challenge and is often cited as the main drawback of the mathematical formulation used in this thesis. Not all discretizations of DFM models

require conforming meshes; methods that handle non-conforming meshes include the extended finite element method (XFEM) [36, 24], Lagrange multiplier for finite elements [56], and the embedded discrete fracture matrix model (EDFM) [60]. In XFEM and the Lagrange multiplier method, the difficulties of meshing are traded for more complicated numerics [90]. The EDFM method was originally designed to handle highly permeable fractures for single-phase flow, and including blocking fractures or multiphase flow requires adaptation of the method [45]. If the challenges of the meshing are overcome, the numerics on conforming meshes are much easier and flexible, which are demonstrated by the wide range of applications in the Papers A-E, which all fit into the same framework using conforming meshes.

The first topic of this chapter is on the mixed-dimensional meshes used for the discretizations. Sections 4.2 and 4.3 give a brief overview over classical discretizations on fixed-dimensional meshes. For details on the discretizations, we refer to Paper B. Finally, the full discretization of a mixed-dimensional problem is presented in Section 4.4; for further details see Paper D.

4.1 Mixed-dimensional meshes

The discretizations in the following sections require a computational mesh of each subdomain and a mortar-mesh of each interface. It is required that the faces of each mesh conform to all subdomains that are of a lower dimension. I.e., for a 3d problem, the faces of the rock matrix mesh should conform to the fractures, the faces of the fracture meshes should conform to the fracture intersections, and the faces of the fracture intersection meshes should conform to the 0d points corresponding to intersections of intersections. While it is necessary for the faces of a mesh to conform to the geometry of the lower-dimensional manifold, it is not a requirement for the different meshes to be matching. An example of a mixed-dimensional mesh is shown in Figure 4.1. In this example, the faces of the 3d mesh do not match the 2d cells, but the faces do conform to the geometry of the fractures as well as the 1d intersections and 0d point.

There exist many different softwares that can generate simplex meshes conforming to lower-dimensional surfaces [82, 95]. Unless otherwise stated, Gmsh [40] is used for triangular meshes within this thesis. An issue with simplex meshes is that the most used finite volume-discretization in porous media, the two-point flux approximation (TPFA), is not consistent unless the mesh is K-orthogonal [1, 54], which is in general not the case for sim-

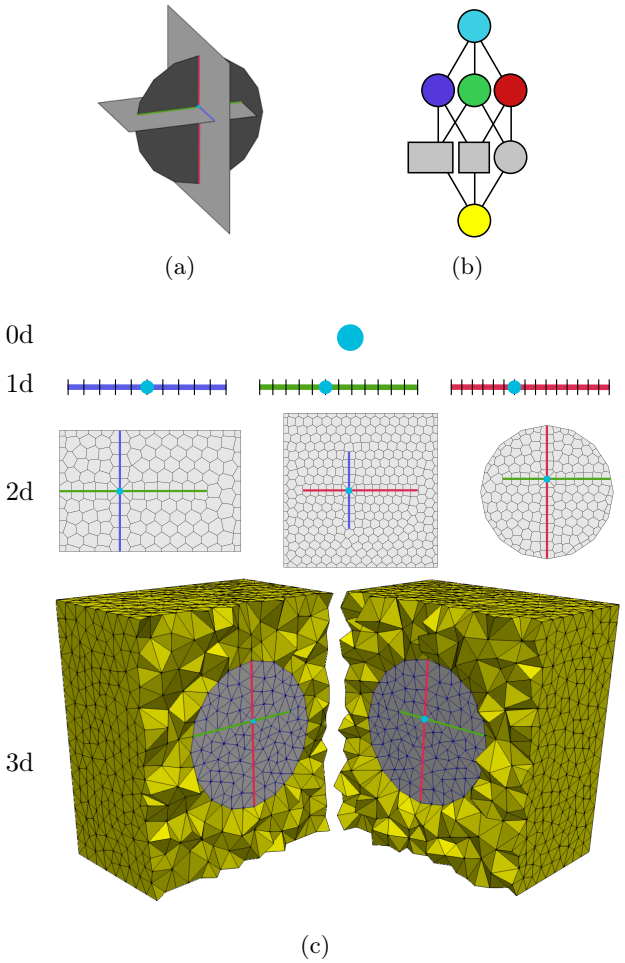

Figure 4.1: (a) A fractured porous medium defined by the 3d rock matrix (not shown), the 2d fractures, the 1d fracture intersections, and the 0d intersection of intersections. (b) Illustration of the graph representation of the mixed-dimensional mesh. The colors of the nodes of the graph correspond to the color of the meshes in (c). The gray nodes correspond to the 2d meshes of the same shape. (c) The corresponding 3d, 2d, 1d and 0d meshes. The 3d mesh is opened along the disk-fracture to reveal the fractures. Note that the 3d mesh conforms to the fracture surfaces, but the faces of the 3d mesh do not match the cells of the 2d mesh. The figure is adapted from Paper E.

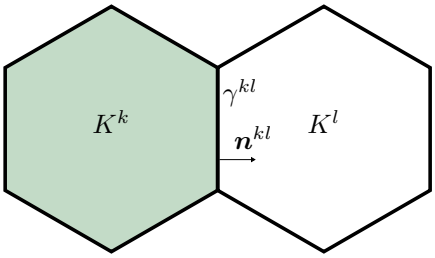

Figure 4.2: Two grid-cells K^k and K^l. Their shared boundary is denoted by γ^{kl} and the normal vector pointing from K^k to K^l is denoted by $\boldsymbol{n}^{kl}$.

plices. There exist modifications to the two-point flux approximation that attempts at resolving this issue, either by placing the degree of freedom at the circumcenter or by introducing a non-linear transmissibility [77]. An alternative is to use conforming polyhedron meshes, which is the main topic of Paper E.

After the meshes of all subdomains are generated, they must be stored in some data-structure. There can be hundreds of fractures and thousands of fracture intersections in a mixed-dimensinal DFM model, and keeping track of the subdomains and interfaces can be overwhelming unless a feasible data-structure is used. The data-structure used in this thesis and implemented in the PorePy software (presented in Paper D) is a graph. Each subdomain is associated with a node in the graph, and the interfaces of the subdomains are associated with the edges of the graph. Examples of the graph structure are shown in Figures 4.1 and 4.3, and this topic is discussed further in Section 4.4.

In the following sections, the fixed-dimensional discretizations are presented, and we conclude this section by giving the notation needed to define the relations between the cells, the faces, and the variables of a given (fixed-dimensional) mesh. Let us consider the two grid-cells K^k and K^l depicted in Figure 4.2. In the finite-volume discretizations presented in this chapter, the discrete variables are all associated with the cell-centers. We refer to a variable associated with the cell-center of cell K^k by a corresponding subscript (e.g., the pressure of cell K^k is denoted p^k). Some discrete quantities are also defined on the faces of the cells. In particular, for the flow and transport equations this will be the fluid flux, $\boldsymbol{v}$, and for the mechanics traction is defined on the faces. The discrete quantity on the face between cell K^k and K^l is identified by the superscript kl (e.g., the fluid flux across face γ^{kl} is denoted v^{kl}).

4.2 Elliptic discretization

In all the papers, finite-volume methods are used to discretize elliptic operators. This includes the pressure equation, the poroelastic equation, and the diffusive part of the transport equation. The general structure of all these equations is equivalent, and to derive a discretization for them we start by defining the general steady-state conservation equation

$$\nabla \cdot \boldsymbol{F} = \tilde{q}, \tag{4.1}$$

where $\boldsymbol{F}$ is the flux of the conserved quantity and $\tilde{q}$ is a source/sink term. We express the conserved quantity in terms of the potential, denoted by ξ,

$$\boldsymbol{F} = -\mathcal{T}\nabla\xi,$$

where $\mathcal{T}$ is a given symmetric positive definite tensor. If we consider the pressure equation given by Equation (3.6), the conserved quantity is the fluid flux, $\boldsymbol{F} = \boldsymbol{v}$, the symmetric positive tensor is the permeability divided by the viscosity, $\mathcal{T} = \mathcal{K}/\mu$, and the potential is the pressure, $\xi = p$.

A finite-volume discretization of Equation (4.1) is obtained by integrating the equation over each computational cell, K, and applying the divergence theorem:

$$-\int_{\partial K} \boldsymbol{F} \cdot \boldsymbol{n} \,\mathrm{d}A = \int_K \tilde{q} \,\mathrm{d}V.$$

The integral over the source term $\tilde{q}$ is easily obtained by appropriate quadrature rules, thus, the main concern here is the approximation of the boundary integral $\int_{\partial K} \boldsymbol{F} \cdot \boldsymbol{n} \,\mathrm{d}A$. In the finite-volume schemes considered in this thesis, the discrete flux over a face γ^{kl}, denoted by F^{kl}, is approximated by the potential, ξ, in the cells:

$$\frac{1}{|\gamma^{kl}|}\int_{\gamma^{kl}} \boldsymbol{F} \cdot \boldsymbol{n} \,\mathrm{d}A \approx F^{kl} = \sum_{m=1}^{n_c} t_m^{kl}\xi^m, \tag{4.2}$$

where $|\gamma^{kl}|$ is the area of the face, n_c is the number of cells, and t_m^{kl} is the face transmissibility. To achieve a sparse discretization, the transmissibilities, t_m^{kl}, are normally different from zero for only a few cells per face. All finite-volume schemes considered in this thesis follow this general structure, the difference is in how the transmissibilies are calculated. For the scalar problems (fluid flow and diffusive flux) the two-point flux approximation [74, 89] and the multi-point flux approximation [2, 30, 53] are

used. For the poroelastic equations (3.11)-(3.12) a generalization of the multi-point stress approximation is used [78, 49]. Paper B gives details on how the transmissibilities are computed and the boundary conditions are included.

Assembling the transmissibilities and considering all control-volumes, we obtain a linear system given by the potential:

$$A\boldsymbol{\xi} = \boldsymbol{b}, \tag{4.3}$$

where A is the discretization matrix, $\boldsymbol{\xi}$ is the vector of potentials associated with each cell, and $\boldsymbol{b}$ is integrated source/sink term as well as possible boundary conditions.

4.3 Hyperbolic discretization

The finite-volume discretization for the transport equation (3.7) is obtained by integrating the equation over a control volume K, and applying the divergence theorem to the advective and diffusive terms:

$$\int_K \frac{\partial \phi c}{\partial t}\,\mathrm{d}V - \int_{\partial K} \boldsymbol{n}\cdot c\boldsymbol{v}\,\mathrm{d}A - \int_{\partial K} \boldsymbol{n}\cdot \mathcal{D}\nabla c\,\mathrm{d}A = \int_K q_c\,\mathrm{d}V.$$

This equation consists of three parts: a time derivative, an advective term and a diffusive term. The diffusive term, $\int_{\partial K} \boldsymbol{n}\cdot\mathcal{D}\nabla c\,\mathrm{d}A$, has an elliptic structure, equivalent to the pressure equation (3.6), and can be discretized by the procedure in Section 4.2. The remainder of this section is therefore concerned with the discretization of the temporal and advective term.

4.3.1 Temporal discretization

Consider the time derivative of an unknown quantity of interest ξ, given by a function S,

$$\frac{\partial \xi}{\partial t} = S(\xi).$$

The time derivative can be approximated by a finite difference scheme. The unknown solution at the next time step, ξ^{k+1}, is obtained from the solution at the current time step, ξ^k, by the theta scheme:

$$\frac{\xi^{k+1}-\xi^k}{\Delta t} = \theta S(\xi^{k+1}) + (1-\theta)S(\xi^k),$$

where Δt is the length of the time step, and θ is a given parameter. If $\theta = 1$ the implicit Euler scheme is obtained, if $\theta = 0$ the explicit Euler scheme is obtained, and if $\theta = 0.5$ the Crank-Nicolson scheme is obtained.

4.3.2 Upwind discretization

The advective flux over a face, kl, is approximated by

$$\frac{1}{|\gamma^{kl}|}\int_{\gamma^{kl}} \boldsymbol{n}^{kl}\cdot c\boldsymbol{v}\,\mathrm{d}A \approx c^{kl}v^{kl},$$

where c^{kl} is the concentration evaluated at the face. We have already obtained a discrete expression for the fluid flux across the face, v^{kl}, given by Equation (4.2). To evaluate the concentration at the face, the natural choice is an upwind scheme [59, 18], that is, the concentration at a face is defined by the cell the fluid is flowing out from:

$$c^{kl} = \begin{cases} c^k, & \text{if } v^{kl} > 0 \\ c^l, & \text{if } v^{kl} \leq 0. \end{cases}$$

4.4 Mixed-dimensional discretization

The brief introduction of the discretizations in the previous sections all consider a fixed-dimensional mesh, and these discretizations form the main building block of the mixed-dimensional discretization. The main question to be answered in this section is how the different fixed-dimensional discretizations can be included in the global system to formulate the complete mixed-dimensional discretization.

At this point it can be beneficial to consider a concrete example. Let the mixed-dimensional subdomain consist of a 2d rock matrix, Ω_h, a single 1d fracture, Ω_l, and the interface connecting them, Γ_j, as shown in Figure 4.3. Let us define the incompressible flow Equation (3.6) in both the rock matrix and fracture subdomain (assuming unit viscosity to simplify notation)

$$\begin{aligned} -\nabla\cdot\mathcal{K}_h\nabla p_h &= 0 && \text{in } \Omega_h, \\ -\nabla\cdot\mathcal{K}_l\nabla p_l &= \Xi_j^l\lambda_j && \text{in } \Omega_l, \\ -\mathcal{K}_h\nabla p_h &= \Xi_j^h\lambda_j && \text{on } \partial_j\Omega_h, \end{aligned} \tag{4.4}$$

and the Darcy type coupling law given by Equation (3.4) on the interface:

$$\lambda_j = -\mathcal{K}_j(\Pi_j^l p_l - \Pi_j^h \mathrm{tr}\ p_h) \quad \text{on } \Gamma_j. \tag{4.5}$$

We can discretize the pressure Equation (4.4) in the two subdomains separately, e.g., by using the finite-volume scheme described in Section 4.2. This results in the two discretization matrices A_h and A_l, as well as the

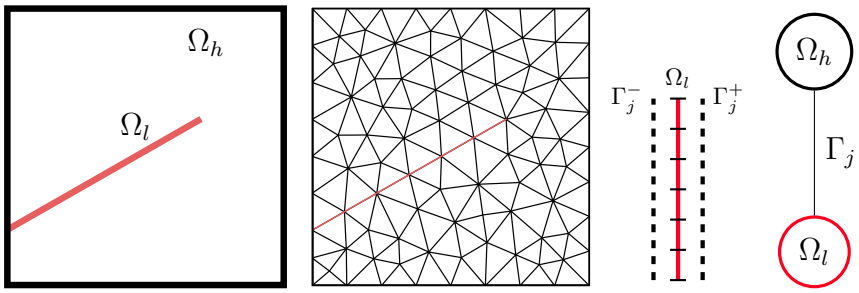

Figure 4.3: (a) A mixed-dimensional subdomain consisting of the 2d rock matrix Ω_h and the single fracture Ω_l. The two subdomains are coupled by the interface Γ_j. (b) The 2d mesh of Ω_h, the 1d mesh of Ω_l, and the interface Γ_j between the two subdomains. The interface Γ_j is given by the union of the two sides of the fracture, Γ_j^+, Γ_j^-. (c) The graph representation of the mixed-dimensional subdomain.

right-hand sides $\boldsymbol{b}_h$ and $\boldsymbol{b}_l$, as given by Equation (4.3). In the lower-dimensional subdomain, the mortar flux λ_j is added as a source contribution, and in the higher dimensional subdomain λ_j is added as a Neumann boundary condition. The discretization of the coupling term given by Equation (4.5) results in the discrete system of equations

$$D_j \boldsymbol{\lambda}_j = -(\Pi_j^l P_l \boldsymbol{p}_l - \Pi_j^h P_h \boldsymbol{p}_h),$$

where P_h is the discrete representation of the pressure trace of Ω_h, and P_l gives the pressure unknowns of the lower-dimensional subdomain Ω_l. The matrix D_j, that has diagonal elements $1/\mathcal{K}_j$, represents the inverse normal permeability of the interface. The global system for the mixed-dimensional discretization then takes the form

$$\begin{bmatrix} A_h & 0 & N_h \Xi_j^h \\ 0 & A_l & S_l \Xi_j^l \\ -\Pi_j^h P_h & \Pi_j^l P_l & D_j \end{bmatrix} \begin{bmatrix} \boldsymbol{p}_h \\ \boldsymbol{p}_l \\ \boldsymbol{\lambda}_j \end{bmatrix} = \begin{bmatrix} \boldsymbol{b}_h \\ \boldsymbol{b}_l \\ \boldsymbol{0} \end{bmatrix},$$

where N_h is the discretization of Neumann boundary conditions on the higher-dimensional grid, Ω_h, and the matrix S_l is the discretization of source terms in the lower-dimensional subdomain, Ω_l. Note that the discrete reconstruction of the pressure trace P_h might for some finite-volume discretizations (e.g., the multi-point flux approximation) have a contribution from the boundary conditions as well as the mortar flux λ_j. The

contribution from the boundary condition gives a non-zero right-hand side for the discrete coupling law, and the dependence of the mortar flux on the pressure trace modifies the matrix D_j.

For the simple example in the previous paragraph it is trivial to write down the equations on each subdomain and assemble them "by hand" in the global discretization matrix. However, for more complicated domains with many fractures and fracture-intersections, this would be a tedious job. Even for the relatively simple domain given in Figure 4.1, there are eight subdomains to be discretized and twelve couplings between subdomains. A good data structure is therefore needed to represent the mixed-dimensional subdomains. As mentioned, we have chosen to represent the geometry as a graph. The mixed-dimensional discretization is then a matter of filling out block matrices as given by the graph structure. First, we loop over all nodes in the graph and discretize the given equations using standard fixed-dimensional discretizations, which fill out the block-diagonal of the global discretization matrix. Then, we loop over all edges of the graph and discretize the coupling equations, which fill out the off-diagonal blocks of the global discretization matrix. See also [48] for more details about the relation between the graph structure and the global discretization.

The incompressible flow example considered above is the simplest of all models presented in this thesis. However, the discretization of the transport equation and poroelasticity follow the same procedure; see Papers B and D for details. This is the great benefit we get from choosing a discretization and implementation that resemble the mathematical models so closely. This framework facilitates code reuse and prototyping of mixed-dimensional PDEs, with no need to invent new complicated numerical methods and discretizations for different physical processes.

Chapter 5

Summary and outlook

5.1 Summary of papers

Paper A

Title:	Reactivation of Fractures in Subsurface Reservoirs – A Numerical Approach Using a Static-Dynamic Friction Model
Authors:	Runar L. Berge, Inga Berre, Eirik Keilegavlen
Book:	Numerical Mathematics and Advanced Applications ENUMATH 2017
DOI:	10.1007/978-3-319-96415-7_60

In Paper A, we consider the deformation of a fractured porous medium due to fluid injections. The problem statement is similar to the problem in Paper B, however, the focus is more towards applications, with stimulation of EGS reservoirs as the main motivation. The porous material is modeled as a linear elastic material, and the deformation of the fractures is governed by a Coulomb friction law. Fluid is injected into the fracture network, and the elevated fluid pressure reduces the effective normal traction on the fractures which causes them to slide. To solve the inequalities resulting from the Coulomb friction, we use an iterative scheme as suggested in [96]. In this scheme, the sliding at each iteration is estimated based on how much the friction bound is violated. The scheme has been popular [68, 69], partly due to its simplicity which makes it easy to implement. The main contribution of Paper A is an improvement to the scheme where we show how a step-length parameter used in the fixed-point scheme is dependent

on the mesh-size, as well as the Lamé parameters. An optimal value for the step-length is suggested, and the choice is confirmed by numerical experiments that show that a significantly reduction in the number of iterations may be obtained.

Paper B

Title: Finite volume discretization for poroelastic media with fractures modeled by contact mechanics.

Authors: Runar L. Berge, Inga Berre, Eirik Keilegavlen, Jan-Martin Nordbotten, Barbara Wohlmuth

Journal: Accepted to International Journal for Numerical Methods in Engineering

DOI: 10.1002/nme.6238

One of the disadvantages of the scheme presented in Paper A is that it still might require many iterations to converge, further, it only approximate the inequality constraints as it overshoots the slip distance. In Paper B, we develop a new discretization for fractured poroelastic rock. The deformation of the fractures is governed by a nonpenetration condition in the normal direction and a Coulomb friction law in the tangential direction. A hybrid formulation is used to discretize the contact mechanics governing fracture deformation [44, 99], and to discretize the poroelastic equations the finite-volume scheme multi-point stress approximation (MPSA) is used [78, 49]. The main contribution of this paper is the combination of the hybrid formulation with MPSA. The discretization introduces additional degrees of freedom on the contact interface in the form of a Lagrange multiplier representing the contact pressure. The Lagrange multiplier is naturally included in the local systems of MPSA as a Neumann boundary condition. One of the desirable features of the discretization is that it is locally mass and momentum conservative despite the cell-centered degrees of freedom.

We observe that the convergence of the Newton solver in Paper B is much faster than the fixed-point type iteration presented in Paper A. Further, the method in Paper B satisfy the discrete inequality constraint exactly. Paper B also shows by numerical experiments that the convergence rates of the MPSA scheme do not deteriorate by the introduction of the Lagrange multiplier by examining both 2d and 3d cases.

The methods developed in Paper B have recently been extended to include thermoelasticity, which is mathematically very similar to poroelasticity [93].

Paper C

Title:	Viscous fingering in fractured porous media
Authors:	Runar L. Berge, Inga Berre, Eirik Keilegavlen, Jan-Martin Nordbotten
Journal:	In preparation

Paper C studies unstable viscous flow through fractured porous media. When a less viscous fluid displaces a more viscous fluid, hydromechanical instabilities can create viscous fingers, and as the fingers grow, they define dynamic preferential flow paths through the porous media [43, 4]. Viscous fingering has been extensively studied, and we refer to the introduction of Paper C, and the references therein, for an overview. Despite all the attention given to viscous fingering, little has been done on the interaction between viscous fingering and fractures. Budek et al. [21] consider viscous fingering in micro channels, but not consider flow in the areas between the channels. Viscous fingering for radial flow in a fractured medium is considered by Zhang et al. [103], where they employ a fractal growth model to simulate the displacement processes.

The main focus of Paper C is given to the interaction between the fixed preferential flow-paths defined by the fracture geometry, and the dynamic preferential flow paths given by the viscous fingers. We present the dimensionless numbers that governs the behavior of the system, and identify two distinct flow regimes. In the first regime, the dynamic is given by the viscous instability, while in the second regime the dynamic is given by the geometry of the fracture network. In the cross-over regime, there is a complex interplay between the viscous instabilities and the fracture network giving very different flow patterns, even for small changes to the fracture network geometry.

Paper D

Title:	PorePy: An Open-Source Software for Simulation of Multiphysics Processes in Fractured Porous Media
Authors:	Eirik Keilegavlen, Runar L. Berge, Alessio Fumagalli, Michele Starnoni, Ivar Stefansson, Jhabriel Varela, Inga Berre
Journal:	*Submitted to Computational Geosciences*
arXiv:	1908.09869 [math.NA]

Computer softwares for simulating flow in porous media have been around for decades. The first simulations were of simple 1d or 2d models of

the porous media, but as the computational resources have increased, so has the sophistication of the softwares. Today, there exist many different frameworks for simulating flow in porous media, some are highly specialized commercial codes, while others are more general finite element codes. What is common for most of these softwares is that they are made for solving problems of a fixed dimension, and the softwares do not necessary fit well into the mixed-dimensional modeling presented within this thesis. In Paper D, we discuss the implementation of mixed-dimensional models, exemplified through the software PorePy. The software is released open-source and can be downloaded from www.github.com/pmgbergen/porepy or from Zenodo [47]. Paper D demonstrates the flexibility of the mathematical framework presented in Chapter 3 by considering several different physical processes, including flow, transport and poroelasticity.

Except from the gridding algorithm presented in Paper E, the computer code developed during this thesis work has been developed and maintained in PorePy. Paper D thus serves as an overview to many of the main ideas of this thesis, and the paper works to some extent as a summary of Part I.

Paper E

Title:	Unstructured Voronoi grids conforming to lower dimensional objects
Authors:	Runar L. Berge, Øystein S. Klemetsdal, Knut-Andreas Lie
Journal:	Computational Geosciences, volume 23, issue 1, pp 169–188, 2019
DOI:	10.1007/s10596-018-9790-0

The generation of meshes that conform to lower-dimensional fractures is often listed as one of the main challenges or drawbacks for the mixed-dimensional DFM model. Due to the complex geometry of fracture networks, the development of fast, robust, and flexible conforming meshing algorithms has been and is a formidable challenge. For subsurface application, polyhedron meshes are usually the mesh type of choice, since finite-volume methods often do not perform well on simplex meshes. For example, the two-point flux approximation, which is the industry standard, is in most cases not consistent on simplices, which can lead to large discretization errors [101, 54]. Paper E aims at constructing unstructured Voronoi meshes (or PEBI-grids, as they are often called in the petroleum industry), that conform to lower-dimensional surfaces. Previously, many different methods for construction conforming Voronoi meshes have been

proposed, however, these have been limited to either 2d [17, 37, 64] or just approximations of the surfaces in 3d [70, 71]. Very recently, Abdelkader et al. [3] presented a similar algorithm to the one in Paper E, however, the focus is rather on the conforming 3d mesh and not the full hierarchy of meshes.

The main idea of the algorithm presented in Paper E is very much inspired by the mixed-dimensional models for fracture porous media presented in Part I and Paper D. The Voronoi meshes are built in ascending order based on the dimension of the subdomains, from the 0d intersections to the 3d mesh. The Voronoi mesh of each subdomain is constructed such that the faces of the mesh conform to the cells of the subdomains of one dimension lower. In this way, we can show under certain assumptions that we not only construct a 3d mesh that conforms to the 2d surfaces, but we build the full hierarchy of meshes, where the 1d meshes conform to the 0d points, the 2d meshes conform to the 1d lines, and the 3d mesh conforms to the 2d surfaces.

In the introduction to this thesis, open-source development is listed as one of the main contributions. The implementation of the meshing algorithms presented in Paper E has been released as a module in MRST [61], and the module is used by a number of other authors, including [55, 5, 75, 62].

5.2 Outlook

The demand for fast, robust, and accurate simulation tools for fractured porous media will continue to grow in the coming years. This thesis has covered a broad range of topics within fractured porous media including poromechanics, unstable displacement processes, and meshing. A great deal can be said about possible continuations of the scientific work, and a selection of these continuations are summarized in this section.

To include thermal effects can be important for the stimulation processes of EGS as cooling of the rock cause it to shrink and cause further slip of the fractures. The discretization of the poroelastic equations with contact mechanics in Paper B can be expanded to include thermoelasticity as the structure of the thermoelastic and poroelastic equations are very similar. A first step towards this direction is done in [93]. One of the advantages of the formulation presented in Paper B is that all non-linearities can be solved in the same Newton iteration. This will be of importance if the method is expanded to more complicated non-linear models, e.g., by including a non-constant coefficient of friction such as the rate and state

model [27]. Combining our discretization with a rate and state model could be used to improve the simulations of the seismic activity related the stimulation of EGS reservoirs.

The study in Paper C demonstrates that the mixed-dimensional framework can be used for complicated physical processes. The results in the paper clearly show that it is crucial to include the geometry of the fracture network in the simulations; the different fracture networks affect the viscous fingering in different ways and create non-trivial flow paths through the porous media. This shows that including the explicit representation of the fractures in simulations is of great importance, as it is very hard to upscale the effects observed in Paper C. Continuations of the work in Paper C include improvements to the quantification of the results to pinpoint where the border between different regimes happens, systematic study of how changes in geometry effects the flow, e.g., by rotating the geometries of the used fracture networks, and study stochastically generated fracture networks.

In Paper E, we give a condition (called the fracture condition) that guarantees a conforming mesh if it is satisfied. The condition is easy to test, however, the condition does not give a solution to how the mesh can be changed if the condition is not met. One way to improve the meshing algorithm would be by including information between the meshes of the same dimension to better estimating the correct local mesh size. A method in 2d is presented in the paper, and this method could be extended to 3d. Another possible extension is to use the refinement method presented by Abdelkader et al. [3] for the Voronoi sites that do not satisfy the fracture condition.

The work of this thesis joins the trend of releasing scientific computer codes open-source. Within the context of porous media, there already exist many open-source initiatives, and the main parts of this thesis have been developed and maintained in the open-source software PorePy. While it requires a large effort to release such a open-source code, it is not only beneficial to the users of the code, but also to the developers and community as a whole.

Sharing code is not the only reason we believe that the number of open-source scientific codes will continue to grow in the future. Another reason, that might be even more important, is reproducibility of scientific results. Using PorePy and fractured porous media as an example, the development of a computer code for the mathematical models presented in Chapter 2 is an enormous effort and cannot be completed by any single PhD-student alone. The development of open-source code is therefore

essential to facilitate reproducibility. If it requires thousands of hours to develop the framework needed to produce the results of a paper, it is (practically) impossible to reproduce the results, unless the framework is publicly available.

As a final note, we also believe (and hope) that in the future it will become more common to also make the examples and numerical experiments presented in papers publicly available. This is not only a matter of releasing the source code, but also cleaning up the code and making it feasible to run. Dependencies on obscure packages and outdated versions can make any installation a pain. From the experiences made during this thesis, tools like Docker can help overcome many of these technical difficulties. Hopefully, we will in the coming years see many more works released open-source for the benefit of other researches and the reproducibility of scientific results.

Bibliography

[1] I. Aavatsmark, T. Barkve, Ø. Bøe, and T. Mannseth. "Discretization on Non-Orthogonal, Quadrilateral Grids for Inhomogeneous, Anisotropic Media". In: *Journal of Computational Physics* 127.1 (1996), pp. 2–14. doi: 10.1006/jcph.1996.0154.

[2] I. Aavatsmark. "An Introduction to Multipoint Flux Approximations for Quadrilateral Grids". In: *Computational Geosciences* 6.3 (2002), pp. 405–432. doi: 10.1023/A:1021291114475.

[3] A. Abdelkader, C. L. Bajaj, M. S. Ebeida, A. H. Mahmoud, S. A. Mitchell, J. D. Owens, and A. A. Rushdi. "VoroCrust: Voronoi Meshing Without Clipping". In: *arXiv e-prints* (2019). arXiv: 1902.08767 [cs.GR].

[4] J.-C. Bacri, N. Rakotomalala, D. Salin, and R. Wouméni. "Miscible viscous fingering: Experiments versus continuum approach". In: *Physics of Fluids A: Fluid Dynamics* 4.8 (1992), pp. 1611–1619. doi: 10.1063/1.858383.

[5] K. Bao, K.-A. Lie, O. Møyner, and M. Liu. "Fully implicit simulation of polymer flooding with MRST". In: *Computational Geosciences* 21.5 (2017), pp. 1219–1244. doi: 10.1007/s10596-017-9624-5.

[6] G. I. Barenblatt, I. P. Zheltov, and I. N. Kochina. "Basic concepts in the theory of seepage of homogeneous liquids in fissured rocks". In: *Journal of Applied Mathematics and Mechanics* 24.5 (1960), pp. 1286–1303. doi: 10.1016/0021-8928(60)90107-6.

[7] Z. P. Bažant, M. Salviato, V. T. Chau, H. Viswanathan, and A. Zubelewicz. "Why Fracking Works". In: *Journal of Applied Mechanics* 81.10 (2014), 101010–1–101010–10. doi: 10.1115/1.4028192.

[8] J. Bear. "1 - Modeling Flow and Contaminant Transport in Fractured Rocks". In: *Flow and Contaminant Transport in Fractured Rock*. Ed. by J. Bear, C.-F. Tsang, and G. de Marsily. Oxford: Academic Press, 1993, pp. 1–37. doi: 10.1016/B978-0-12-083980-3.50005-X.

[9] J. Bear. *Dynamics of Fluids in Porous Media*. Dover Civil and Mechanical Engineering Series. Dover, 1988.

[10] B. Berkowitz. "Characterizing flow and transport in fractured geological media: A review". In: *Advances in Water Resources* 25.8 (2002), pp. 861–884. doi: 10.1016/S0309-1708(02)00042-8.

[11] C. Bernardi, Y. Maday, and A. T. Patera. "A new nonconforming approach to domain decomposition: The mortar element method". In: *Nonlinear Partial Differential Equations and their Applications*. Ed. by H. Brezis and J.-L. Lions. Vol. XI of *Collège de France Seminar*. Pitman, 1994, pp. 13–51.

[12] C. Bernardi, Y. Maday, and A. T. Patera. "Domain Decomposition by the Mortar Element Method". In: *Asymptotic and Numerical Methods for Partial Differential Equations with Critical Parameters*. Ed. by H. G. Kaper, M. Garbey, and G. W. Pieper. Dordrecht: Springer Netherlands, 1993, pp. 269–286.

[13] I. Berre, W. Boon, B. Flemisch, A. Fumagalli, D. Gläser, Keilegavlen, A. Scotti, I. Stefansson, and A. Tatomir. "Call for participation: Verification benchmarks for single-phase flow in three-dimensional fractured porous media". In: *arXiv e-prints* (2018). arXiv: 1809.06926 [math.NA].

[14] M. A. Biot. "General Theory of Three-Dimensional Consolidation". In: *Journal of Applied Physics* 12.2 (1941), pp. 155–164. doi: 10.1063/1.1712886.

[15] D. Boffi, F. Brezzi, and M. Fortin. *Mixed Finite Element Methods and Applications*. Vol. 44. Springer, Berlin, Heidelberg, 2013.

[16] W. M. Boon and J. M. Nordbotten. "Stable Mixed Finite Elements for Linear Elasticity with Thin Inclusions". In: *arXiv e-prints* (2019). arXiv: 1903.01757 [math.NA].

[17] L. Branets, S. S. Ghai, S. L. Lyons, and X.-H. Wu. "Efficient and Accurate Reservoir Modeling Using Adaptive Gridding with Global Scale Up". In: *Proceedings of the SPE Reservoir Simulation Symposium*. The Woodlands, Texas, 2009. doi: 10.2118/118946-MS.

[18] Y. Brenier and J. Jaffrè. "Upstream Differencing for Multiphase Flow in Reservoir Simulation". In: *SIAM Journal on Numerical Analysis* 28.3 (1991), pp. 685–696. doi: 10.1137/0728036.

[19] K. Brenner, J. Hennicker, R. Masson, and P. Samier. "Gradient discretization of hybrid-dimensional Darcy flow in fractured porous media with discontinuous pressures at matrix–fracture interfaces". In: *IMA Journal of Numerical Analysis* 37.3 (2016), pp. 1551–1585. doi: 10.1093/imanum/drw044.

[20] J. Březina and J. Stebel. "Analysis of Model Error for a Continuum-Fracture Model of Porous Media Flow". In: *High Performance Computing in Science and Engineering*. Ed. by T. Kozubek, R. Blaheta, J. Šístek, M. Rozložník, and M. Čermák. Cham: Springer International Publishing, 2016, pp. 152–160.

[21] A. Budek, P. Garstecki, A. Samborski, and P. Szymczak. "Thin-finger growth and droplet pinch-off in miscible and immiscible displacements in a periodic network of microfluidic channels". In: *Physics of Fluids* 27.11 (2015), p. 112109. doi: 10.1063/1.4935225.

[22] T. Cladouhos, S. Petty, G. Foulger, B. Julian, and M. Fehler. "Injection induced seismicity and geothermal energy". In: *GRC Transactions* 34 (2010), pp. 1213–1220.

[23] O. Coussy. *Poromechanics*. Wiley, 2003.

[24] C. D´Angelo and A. Scotti. "A mixed finite element method for Darcy flow in fractured porous media with non-matching grids". In: *ESAIM: M2AN* 46.2 (2012), pp. 465–489. doi: 10.1051/m2an/2011148.

[25] H. Darcy. *Les Fontaines publiques de la ville de Dijon*. Paris: Victor Dalmont, 1856.

[26] N. Deichmann and D. Giardini. "Earthquakes Induced by the Stimulation of an Enhanced Geothermal System below Basel (Switzerland)". In: *Seismological Research Letters* 80.5 (2009), pp. 784–798. doi: 10.1785/gssrl.80.5.784.

[27] J. H. Dieterich. "Earthquake nucleation on faults with rate-and state-dependent strength". In: *Tectonophysics* 211.1 (1992), pp. 115–134. doi: 10.1016/0040-1951(92)90055-B.

[28] P. Dietrich, R. Helmig, M. Sauter, H. Hötzl, J. Köngeter, and G. Teutsch. *Flow and Transport in Fractured Porous Media*. Springer, Berlin, Heidelberg, 2005. doi: 10.1007/b138453.

[29] A. Dogru, L. Fung, U. Middya, T. Alshaalan, and J. Alberto Pita. "A Next-Generation Parallel Reservoir Simulator for Giant Reservoirs". In: *SPE/EAGE Reservoir characterization and simulation conference* (2009). doi: 10.2118/119272-MS.

[30] M. G. Edwards and C. F. Rogers. "Finite volume discretization with imposed flux continuity for the general tensor pressure equation". In: *Computational Geosciences* 2.4 (1998), pp. 259–290. doi: 10.1023/A:1011510505406.

[31] M. T. Elenius, J. M. Nordbotten, and H. Kalisch. "Convective mixing influenced by the capillary transition zone". In: *Computational Geosciences* 18.3 (2014), pp. 417–431. doi: 10.1007/s10596-014-9415-1.

[32] B. Flemisch et al. "DuMux: DUNE for multi-{phase,component,scale,physics,...} flow and transport in porous media". In: *Advances in Water Resources* 34.9 (2011), pp. 1102–1112. doi: 10.1016/j.advwatres.2011.03.007.

[33] B. Flemisch, I. Berre, W. Boon, A. Fumagalli, N. Schwenck, A. Scotti, I. Stefansson, and A. Tatomir. "Benchmarks for single-phase flow in fractured porous media". In: *Advances in Water Resources* 111 (2018), pp. 239–258. doi: 10.1016/j.advwatres.2017.10.036.

[34] L. Formaggia, A. Fumagalli, A. Scotti, and P. Ruffo. "A reduced model for Darcy's problem in networks of fractures". In: *ESAIM: Mathematical Modelling and Numerical Analysis* 48.4 (2014), pp. 1089–1116. doi: 10.1051/m2an/2013132.

[35] N. Frih, V. Martin, J. E. Roberts, and A. Saâda. "Modeling fractures as interfaces with nonmatching grids". In: *Computational Geosciences* 16.4 (2012), pp. 1043–1060. doi: 10.1007/s10596-012-9302-6.

[36] A. Fumagalli and A. Scotti. "An Efficient XFEM Approximation of Darcy Flows in Arbitrarily Fractured Porous Media". In: *Oil and Gas Science Technology - Rev. IFP Energies nouvelles* 69.4 (2014), pp. 555–564. doi: 10.2516/ogst/2013192.

[37] L. S. K. Fung, X. Y. Ding, and A. H. Dogru. "Unconstrained Voronoi Grids for Densely Spaced Complex Wells in Full-Field Reservoir Simulation". In: *SPE Journal* 19.5 (2014), pp. 803–815. doi: 10.2118/163648-PA.

[38] T. T. Garipov, M. Karimi-Fard, and H. A. Tchelepi. "Discrete fracture model for coupled flow and geomechanics". In: *Computational Geosciences* 20.1 (2016), pp. 149–160. doi: 10.1007/s10596-015-9554-z.

[39] D. Gaston, C. Newman, G. Hansen, and D. Lebrun-Grandié. "MOOSE: A parallel computational framework for coupled systems of nonlinear equations". In: *Nuclear Engineering and Design* 239.10 (2009), pp. 1768–1778. doi: 10.1016/j.nucengdes.2009.05.021.

[40] C. Geuzaine and J.-F. Remacle. "Gmsh: A 3-D finite element mesh generator with built-in pre- and post-processing facilities". In: *International Journal for Numerical Methods in Engineering* 79.11 (2009), pp. 1309–1331. doi: 10.1002/nme.2579.

[41] Y. Guglielmi, F. Cappa, J.-P. Avouac, P. Henry, and D. Elsworth. "Seismicity triggered by fluid injection–induced aseismic slip". In: *Science* 348.6240 (2015), pp. 1224–1226. doi: 10.1126/science.aab0476.

[42] G. E. Hammond, P. C. Lichtner, and R. T. Mills. "Evaluating the performance of parallel subsurface simulators: An illustrative example with PFLOTRAN". In: *Water Resources Research* 50.1 (2014), pp. 208–228. doi: 10.1002/2012WR013483.

[43] G. M. Homsy. "Viscous Fingering in Porous Media". In: *Annual Review of Fluid Mechanics* 19.1 (1987), pp. 271–311. doi: 10.1146/annurev.fl.19.010187.001415.

[44] S. Hüeber, G. Stadler, and B. Wohlmuth. "A Primal-Dual Active Set Algorithm for Three-Dimensional Contact Problems with Coulomb Friction". In: *SIAM Journal on Scientific Computing* 30.2 (2008), pp. 572–596. doi: 10.1137/060671061.

[45] J. Jiang and R. M. Younis. "An improved projection-based embedded discrete fracture model (pEDFM) for multiphase flow in fractured reservoirs". In: *Advances in Water Resources* 109 (2017), pp. 267–289. doi: 10.1016/j.advwatres.2017.09.017.

[46] M. Karimi-Fard, L. J. Durlofsky, and K. Aziz. "An Efficient Discrete-Fracture Model Applicable for General-Purpose Reservoir Simulators". In: *SPE Journal* 9 (2 2004), pp. 227–236. doi: 10.2118/88812-PA.

[47] E. Keilegavlen, R. L. Berge, A. Fumagalli, M. Starnoni, I. Stefansson, J. Varela, and I. Berre. *PorePy, software released on Zenodo*. 2018. doi: 10.5281/zenodo.1287643.

[48] E. Keilegavlen, A. Fumagalli, R. Berge, and I. Stefansson. "Implementation of Mixed-Dimensional Models for Flow in Fractured Porous Media". In: *Numerical Mathematics and Advanced Applications ENUMATH 2017*. Ed. by F. A. Radu, K. Kumar, I. Berre, J. M. Nordbotten, and I. S. Pop. Cham: Springer International Publishing, 2019, pp. 573–580. doi: 10.1007/978-3-319-96415-7_52.

[49] E. Keilegavlen and J. M. Nordbotten. "Finite volume methods for elasticity with weak symmetry". In: *International Journal for Numerical Methods in Engineering* 112.8 (2017), pp. 939–962. doi: 10.1002/nme.5538.

[50] A.-R. Khaled and K. Vafai. "The role of porous media in modeling flow and heat transfer in biological tissues". In: *International Journal of Heat and Mass Transfer* 46.26 (2003), pp. 4989–5003. doi: 10.1016/S0017-9310(03)00301-6.

[51] N. Kikuchi and J. Oden. *Contact problems in elasticity: A study of variational inequalities and finite element methods*. SIAM studies in applied mathematics 8, 1988.

[52] M. King Hubbert and W. W. Rubey. "Role of Fluid Pressure in Mechanics of Overthrust Faulting: I. Mechanics of Fluid-Filled Porous Solids and its Application to Overthrust Faulting". In: *GSA Bulletin* 70.2 (1959), pp. 115–166.

[53] R. A. Klausen and R. Winther. "Convergence of multipoint flux approximations on quadrilateral grids". In: *Numerical Methods for Partial Differential Equations* 22.6 (2006), pp. 1438–1454. doi: 10.1002/num.20158.

[54] Ø. S. Klemetsdal, R. L. Berge, K.-A. Lie, H. M. Nilsen, and O. Møyner. "Unstructured Gridding and Consistent Discretizations for Reservoirs with Faults and Complex Wells". In: *SPE Reservoir Simulation Conference, 20-22 February, Montgomery, Texas, USA* (2017). doi: /10.2118/182666-MS.

[55] Ø. S. Klemetsdal, A. F. Rasmussen, O. Møyner, and K.-A. Lie. "Efficient reordered nonlinear Gauss–Seidel solvers with higher order for black-oil models". In: *Computational Geosciences* (2019). doi: 10.1007/s10596-019-09844-5.

[56] M. Köppel, V. Martin, and J. E. Roberts. "A stabilized Lagrange multiplier finite-element method for flow in porous media with fractures". In: *GEM - International Journal on Geomathematics* 10.7 (2019). doi: 10.1007/s13137-019-0117-7.

[57] S. E. Laubach. "Practical approaches to identifying sealed and open fractures". In: *AAPG Bulletin* 87.4 (2003), pp. 561–579. doi: 10.1306/11060201106.

[58] H. S. Lee and T. F. Cho. "Hydraulic Characteristics of Rough Fractures in Linear Flow under Normal and Shear Load". In: *Rock Mechanics and Rock Engineering* 35.4 (2002), pp. 299–318. doi: 10.1007/s00603-002-0028-y.

[59] R. J. LeVeque. *Finite Volume Methods for Hyperbolic Problems*. Cambridge Texts in Applied Mathematics. Cambridge University Press, 2002. doi: 10.1017/CBO9780511791253.

[60] L. Li and S. H. Lee. "Efficient Field-Scale Simulation of Black Oil in a Naturally Fractured Reservoir Through Discrete Fracture Networks and Homogenized Media". In: *SPE Journal* 11.04 (2008). doi: 10.2118/103901-PA.

[61] K.-A. Lie. *An Introduction to Reservoir Simulation Using MATLAB/GNU Octave: User Guide for the MATLAB Reservoir Simulation Toolbox (MRST)*. Cambridge University Press, 2019.

[62] K.-A. Lie, O. Møyner, and J. R. Natvig. "Use of Multiple Multiscale Operators To Accelerate Simulation of Complex Geomodels". In: *SPE Journal* 22.06 (2017). doi: 10.2118/182701-PA.

[63] E. L. Majer, R. Baria, M. Stark, S. Oates, J. Bommer, B. Smith, and H. Asanuma. "Induced seismicity associated with Enhanced Geothermal Systems". In: *Geothermics* 36.3 (2007), pp. 185–222. doi: 10.1016/j.geothermics.2007.03.003.

[64] S. Manzoor, M. G. Edwards, A. H. Dogru, and T. M. Al-Shaalan. "Interior boundary-aligned unstructured grid generation and cell-centered versus vertex-centered CVD-MPFA performance". In: *Computational Geosciences* (2017), pp. 195–230. doi: 10.1007/s10596-017-9686-4.

[65] V. Martin, J. Jaffré, and J. Roberts. "Modeling Fractures and Barriers as Interfaces for Flow in Porous Media". In: *SIAM Journal on Scientific Computing* 26.5 (2005), pp. 1667–1691. doi: 10.1137/S1064827503429363.

[66] N. S. Martys and C. F. Ferraris. "Capillary transport in mortars and concrete". In: *Cement and Concrete Research* 27.5 (1997), pp. 747–760. doi: 10.1016/S0008-8846(97)00052-5.

[67] M. W. McClure and R. N. Horne. "Investigation of injection-induced seismicity using a coupled fluid flow and rate/state friction model". In: *Geophysics* 76.6 (2011), pp. 181–198. doi: 10.1190/geo2011-0064.1.

[68] M. McClure and R. Horne. "Discrete fracture modeling of hydraulic stimulation in enhanced geothermal systems". In: *Thirty-Fifth Workshop on Geothermal Reservoir Engineering*. Standford University, 2010.

[69] M. McClure and R. Horne. "Numerical and analytical modeling of mechanisms of induced seismicity during fluid injection". In: *Geothermal Resources Council Transactions* 34 (2010), pp. 381–396.

[70] R. Merland, G. Caumon, B. Lévy, and P. Collon-Drouaillet. "Voronoi grids conforming to 3D structural features". English. In: *Computational Geosciences* 18.3-4 (2014), pp. 373–383. doi: 10.1007/s10596-014-9408-0.

[71] R. Merland, B. Lévy, and G. Caumon. "Building PEBI Grids Conforming To 3D Geological Features using Centroidal Voronoi Tessellation". In: *Proceedings of IAMG*. Ed. by R. Marschallinger and R. Zolb. Salzburg, 2011, pp. 254–265.

[72] A. Mikelić, M. F. Wheeler, and T. Wick. "Phase-field modeling of a fluid-driven fracture in a poroelastic medium". In: *Computational Geosciences* 19.6 (2015), pp. 1171–1195. doi: 10.1007/s10596-015-9532-5.

[73] A. Moinfar, K. Sepehrnoori, R. T. Johns, and A. Varavei. "Coupled Geomechanics and Flow Simulation for an Embedded Discrete Fracture Model". In: *SPE Reservoir Simulation Symposium* (2013). doi: 10.2118/163666-MS.

[74] O. Møyner. "Next Generation Multiscale Methods for Reservoir Simulation". PhD thesis. Norwegian University of Science and Technology, 2016. doi: 11250/2431831.

[75] O. Møyner and H. A. Tchelepi. "A Mass-Conservative Sequential Implicit Multiscale Method for Isothermal Equation-of-State Compositional Problems". In: *SPE Journal* 23.06 (2018), pp. 2376–2393. doi: 10.2118/182679-PA.

[76] S. P. Neuman. "Trends, prospects and challenges in quantifying flow and transport through fractured rocks". In: *Hydrogeology Journal* 13.1 (2005), pp. 124–147. doi: 10.1007/s10040-004-0397-2.

[77] K. Nikitin, K. Terekhov, and Y. Vassilevski. "A monotone nonlinear finite volume method for diffusion equations and multiphase flows". In: *Computational Geosciences* 18.3 (2014), pp. 311–324. doi: 10.1007/s10596-013-9387-6.

[78] J. Nordbotten. "Stable Cell-Centered Finite Volume Discretization for Biot Equations". In: *SIAM Journal on Numerical Analysis* 54.2 (2016), pp. 942–968. doi: 10.1137/15M1014280.

[79] J. M. Nordbotten, W. M. Boon, A. Fumagalli, and E. Keilegavlen. "Unified approach to discretization of flow in fractured porous media". In: *Computational Geosciences* 23.2 (2019), pp. 225–237. doi: 10.1007/s10596-018-9778-9.

[80] J. M. Nordbotten and M. A. Celia. *Geological Storage of CO2: Modeling Approaches for Large-Scale Simulation*. John Wiley and Sons, Ltd, 2011.

[81] A. Ouenes and L. Hartley. "Integrated Fractured Reservoir Modeling Using Both Discrete and Continuum Approaches". In: *SPE Annual Technical Conference and Exhibition, 1-4 October, Dallas, Texas* (2000). doi: 10.2118/62939-MS.

[82] P.-O. Persson and G. Strang. "A simple mesh generator in MATLAB". In: *Siam Review* 46.2 (2004), pp. 329–345. doi: 10.1137/S0036144503429121.

[83] K. Pruess. "A Practical Method for Modeling Fluid and Heat Flow in Fractured Porous Media". In: *Society of Petroleum Engineers* 25.01 (1985), pp. 14–26. doi: 10.2118/10509-PA.

[84] M. K. Rahman, M. M. Hossain, and S. S. Rahman. "A shear-dilation-based model for evaluation of hydraulically stimulated naturally fractured reservoirs". In: *International Journal for Numerical and Analytical Methods in Geomechanics* 26.5 (2002), pp. 469–497. doi: 10.1002/nag.208.

[85] V. Reichenberger, H. Jakobs, P. Bastian, and R. Helmig. "A mixed-dimensional finite volume method for two-phase flow in fractured porous media". In: *Advances in Water Resources* 29.7 (2006), pp. 1020–1036. doi: 10.1016/j.advwatres.2005.09.001.

[86] C. E. Renshaw. "On the relationship between mechanical and hydraulic apertures in rough-walled fractures". In: *Journal of Geophysical Research: Solid Earth* 100.B12 (1995), pp. 24629–24636. doi: 10.1029/95JB02159.

[87] M. Sahimi. *Flow and Transport in Porous Media and Fractured Rock: From Classical Methods to Modern Approaches*. John Wiley and Sons, 2011. doi: 10.1002/9783527636693.

[88] T. Sandve, I. Berre, and J. Nordbotten. "An efficient multi-point flux approximation method for Discrete Fracture Matrix simulations". In: *Journal of Computational Physics* 231.9 (2012), pp. 3784–3800. doi: 10.1016/j.jcp.2012.01.023.

[89] T. H. Sandve. "Multiscale simulation of flow and heat transport in fractured geothermal reservoirs". PhD thesis. The University of Bergen, 2013.

[90] N. Schwenck, B. Flemisch, R. Helmig, and B. I. Wohlmuth. "Dimensionally reduced flow models in fractured porous media: crossings and boundaries". In: *Computational Geosciences* 19.6 (2015), pp. 1219–1230. doi: 10.1007/s10596-015-9536-1.

[91] B. Singhal and R. Gupta. *Applied Hydrogeology of Fractured Rocks*. 2nd ed. Springer Netherlands, 2010. doi: 10.1007/978-90-481-8799-7.

[92] I. Stefansson, I. Berre, and E. Keilegavlen. "Finite-Volume Discretisations for Flow in Fractured Porous Media". In: *Transport in Porous Media* 124.2 (2018), pp. 439–462. doi: 10.1007/s11242-018-1077-3.

[93] I. Stefansson, R. Berge, I. Berre, and E. Keilegavlen. "Modelling of Thermally Induced Fracture Slip caused by Fluid Injection During Geothermal Production". In: *Proceedings of World Geothermal Congress 2020*. Submitted. Reykjavik, Iceland, April 26 – May 2, 2020.

[94] K. Terzaghi. "Theory of Consolidation". In: *Theoretical Soil Mechanics*. John Wiley and Sons, Ltd, 1943. Chap. 13, pp. 265–296. doi: 10.1002/9780470172766.ch13.

[95] The CGAL Project. *CGAL User and Reference Manual*. 4.14. CGAL Editorial Board, 2019. URL: https://doc.cgal.org/4.14/Manual/packages.html.

[96] E. Ucar, I. Berre, and E. Keilegavlen. "Three-Dimensional Numerical Modeling of Shear Stimulation of Fractured Reservoirs". In: *Journal of Geophysical Research: Solid Earth* 123.5 (2018), pp. 3891–3908. DOI: 10.1029/2017JB015241.

[97] W. Wang and O. Kolditz. "Object-oriented finite element analysis of thermo-hydro-mechanical (THM) problems in porous media". In: *International Journal for Numerical Methods in Engineering* 69 (2007), pp. 162–201. DOI: 10.1002/nme.1770.

[98] S. Whitaker. "The Forchheimer equation: A theoretical development". In: *Transport in Porous Media* 25 (1996), pp. 27–61. DOI: 10.1007/BF00141261.

[99] B. Wohlmuth. "Variationally consistent discretization schemes and numerical algorithms for contact problems". In: *Acta Numerica* 20 (2011), pp. 569–734. DOI: 10.1017/S0962492911000079.

[100] P. Wriggers. *Computational Contact Mechanics*. 2nd ed. Springer, Berlin, Heidelberg, 2006. DOI: 10.1007/978-3-540-32609-0.

[101] X.-H. Wu and R. Parashkevov. "Effect of Grid Deviation on Flow Solutions". In: *SPE Journal* 14.01 (2009), pp. 67–77. DOI: 10.2118/92868-PA.

[102] Y. Xiong, P. Fakcharoenphol, S. Wang, P. H. Winterfeld, K. Zhang, and Y.-S. Wu. *User's guide of TOUGH2-EGS-MP: A Massively Parallel Simulator with Coupled Geomechanics for Fluid and Heat Flow in Enhanced Geothermal Systems*. 2013. DOI: 10.2172/1136244.

[103] J. H. Zhang, Z. H. Liu, and S. X. Qu. "Simulational Study of Viscous Fingering in Fractured Reservoirs". In: *Proceedings of International Oil and Gas Conference and Exhibition*. 2-6 November, Beijing, China, 1998. DOI: 10.2118/50906-MS.

[104] R. W. Zimmerman and I.-W. Yeo. "Fluid Flow in Rock Fractures: From the Navier-Stokes Equations to the Cubic Law". In: *Dynamics of Fluids in Fractured Rock*. American Geophysical Union (AGU), 2000, pp. 213–224. DOI: 10.1029/GM122p0213.

Part II

Scientific results

Paper B

B

Finite volume discretization for poroelastic media with fractures modeled by contact mechanics

Runar L. Berge, Inga Berre, Eirik Keilegavlen, Jan-Martin Nordbotten, Barbara Wohlmuth

Accepted to International Journal for Numerical Methods in Engineering
DOI: 10.1002/nme.6238

Finite volume discretization for poroelastic media with fractures modeled by contact mechanics

Runar L. Berge[1], Inga Berre[1,2], Eirik Keilegavlen[1], Jan M. Nordbotten[1], and Barbara Wohlmuth[3]

[1] *Department of Mathematics, University of Bergen, Norway*
[2] *NORCE, Norway*
[3] *Department of Mathematics, Technische Universität München, Germany*

Abstract

A fractured poroelastic body is considered where the opening of the fractures is governed by a nonpenetration law while slip is described by a Coulomb-type friction law. This physical model results in a nonlinear variational inequality problem. The variational inequality is rewritten as a complementary function, and a semismooth Newton method is used to solve the system of equations. For the discretization, we use a hybrid scheme where the displacements are given in terms of degrees of freedom per element, and an additional Lagrange multiplier representing the traction is added on the fracture faces. The novelty of our method comes from combining the Lagrange multiplier from the hybrid scheme with a finite volume discretization of the poroelastic Biot equation, which allows us to directly impose the inequality constraints on each subface. The convergence of the method is studied for several challenging geometries in 2d and 3d, showing that the convergence rates of the finite volume scheme do not deteriorate when it is coupled to the Lagrange multipliers. Our method is especially attractive for the poroelastic problem because it allows for a straightforward coupling between the matrix deformation, contact conditions, and fluid pressure.

1 Introduction

Slip and opening of fractures due to fluid injection is of relevance to a number of subsurface engineering processes. In hydraulic reservoir stimulation, the effect is deliberately induced, while in storage operations and wastewater disposal, avoiding reactivation and opening of fractures is important for preserving caprock integrity. In any circumstance, triggering of larger slip events in the form of elevated levels of seismicity must be avoided. The mathematical model of fracture resistance, slip and opening results in a strongly coupled nonlinear variational inequality, which requires advanced numerical schemes to solve. The purpose of this work is to describe and implement a numerical method to solve this problem considering a poroelastic matrix. The fractures are a set of predefined surfaces in the domain, and the nucleation or growth of fractures is not considered.

The flow and mechanics of poroelastic media and the contact mechanics of elastic bodies are well-developed research fields. For a porous or poroelastic medium, we refer to the classical textbooks [12, 4]. There exists an extensive number of discretizations for the elliptic equations describing fluid flow in a porous medium, and they all have different merits. The most popular discretizations are the so-called locally conservative discretizations [42], which include mixed finite elements [41], control-volume finite elements [11], and finite volume methods [1]. For the coupled poroelastic problem, without considering fractures, it is known that a naive discretization of the coupling terms of the fluid pressure and the solid displacement leads to stability issues for finite element schemes [46]. Several different methods have been proposed to remove these oscillations [21, 36, 2]. Recently, a finite volume method called the multipoint stress approximation was introduced for elastic deformations [38, 26]. This method has been extended to the poroelastic Biot equations and shown to be stable without adding any artificial stabilization terms in the limit of incompressible fluids and small time steps [37].

The contact mechanics problem, i.e., contact between two elastic bodies, is also the topic of several textbooks [27, 48]. A widely used solution strategy for the nonlinear variational inequalities resulting from the mathematical formulation is the penalty method [28]. The basic idea is to penalize a violation of the inequality by adding extra energy to the system. The solution depends then, in a very sensitive way, on the choice of the penalty

parameter. If the value of the parameter is too small, the condition number of the algebraic system is extremely poor, and the nonlinear solver converges slowly. If the value is too large, the accuracy of the solution is very poor, and unphysical approximations can be obtained. Therefore, variationally consistent hybrid formulations have gained interest recently. The hybrid formulations are based on the discretization of additional unknown Lagrange multipliers added to the contact region. This method has been applied to, among others, the Signorini problem [5], frictional contact [33], and large deformations [40]; see the survey contribution [47] and the references therein.

For a poroelastic domain including fractures, different models for the contact problem are developed [35, 34, 20, 17]. Most of these models, however, do not take into account the contact problem either by assuming the fractures stick together [35] or that the fluid pressure inside the fractures is so large that the fracture surfaces are never in contact [34, 20]. The full contact problem for a fractured poroelastic domain is considered by Garipov et al [17], where they applied the penalty method to solve the nonlinear variational inequalities resulting from the contact problem.

In the current work, we present a different numerical solution approach for poroelastic media with contact mechanics. The discretization is based on a finite volume method for poroelasticity [37] combined with a variationally consistent hybrid discretization [22, 47]. The hybrid formulation considered in this work can be regarded as a mortar formulation [8] using matching meshes with the displacement as the primal variable and the surface traction as the dual variable. The finite volume scheme has previously been extended to fracture deformation by adding additional displacement unknowns on the fracture faces [45]. This formulation was successfully used to implement a fixed-point type iteration to approximate the friction bound [43]; however, this formulation suffers from the fact that a step length parameter needs to be tuned and that it might require many iterations to converge [6]. An advantage of the scheme used in this work, where the Lagrange multiplier of the hybrid formulation is coupled with the surface traction obtained from the finite volume scheme, is that it gives a natural formulation of the contact condition per subface. This formulation allows us to rapidly solve the resulting nonlinear inequality problem by applying a semismooth Newton method; see the work by Hüeber et al [22], among others [47, 23].

The remainder of this paper is structured as follows. First, we state the problem and give the governing equations. Then, the discretization is presented, which is divided into two parts: (i) the finite volume discretization for the Biot equations and (ii) the discrete hybrid formulation for the contact problem. We present four numerical examples. The first two consider the dry case where the coupling between fluid pressure and deformation of the rock is disregarded. The last two examples solves the poroelastic deformation of a 2d and 3d domain where the deformation of fractures is governed by a Coulomb friction law. Finally, we give concluding remarks.

2 Problem statement

Let Ω be a fractured deformable porous body. The boundaries of the domain $\partial\Omega$ are divided into three disjoint open sets, Γ_D, Γ_N, and Γ_C, as illustrated in Figure 1: for the first set, a Dirichlet boundary condition is assigned; for the second, a Neumann boundary condition is assigned; and the last is the internal fracture boundary. We consider the Biot model for a poroelastic medium [9]:

$$
\begin{aligned}
-\nabla\cdot\sigma &= \boldsymbol{f}_u && \text{in } \Omega,\\
\mathcal{C}:(\nabla\boldsymbol{u}+(\nabla\boldsymbol{u})^\top)/2-\alpha pI &= \sigma && \text{in } \Omega,\\
c_0\dot{p}+\alpha\nabla\cdot\dot{\boldsymbol{u}}+\nabla\cdot\boldsymbol{q} &= f_p && \text{in } \Omega,\\
\boldsymbol{q} &= -\mathcal{K}\nabla p && \text{in } \Omega,\\
\boldsymbol{u} &= \boldsymbol{g}_{u,D} && \text{on } \Gamma_{u,D},\\
\sigma\cdot\boldsymbol{n} &= \boldsymbol{g}_{u,N} && \text{on } \Gamma_{u,N},\\
p &= g_{p,D} && \text{on } \Gamma_{p,D},\\
\boldsymbol{q}\cdot\boldsymbol{n} &= g_{p,N} && \text{on } \Gamma_{p,N}.
\end{aligned}
\tag{1}
$$

The variables $\dot{p}$ and $\dot{\boldsymbol{u}}$ are the time derivatives of the pressure and displacement, respectively. Throughout this paper we apply a backward Euler time stepping, and $\dot{p}$ and $\dot{\boldsymbol{u}}$ should be interpreted as the discrete derivatives

$$
\dot{p}=\frac{p-p^i}{\Delta t},\quad \dot{\boldsymbol{u}}=\frac{\boldsymbol{u}-\boldsymbol{u}^i}{\Delta t},
\tag{2}
$$

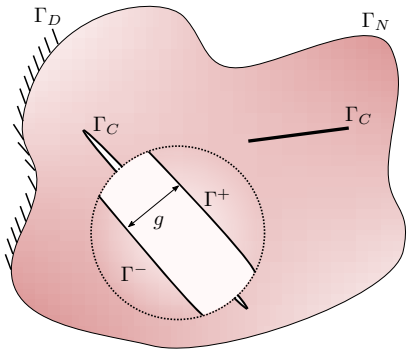

Figure 1: A domain Ω where the external boundary is divided into two parts: Γ_D and Γ_N. Included in the domain are two internal boundaries, or fractures, Γ_C. The two sides of the internal boundaries are labeled Γ^+ and Γ^-, as shown in the magnified circular region of the domain. The function $g(\boldsymbol{x}), \boldsymbol{x} \in \Gamma^+$ gives the initial gap between the two fracture sides. The left fracture has an initial gap $g > 0$, while the top right fracture has an initial gap $g = 0$.

for the previous time iterate i and time step length Δt. Note that we have dropped the index for the current time iterate, $i + 1$. All parameters are, in general, functions of space, e.g., $\mathcal{C} = \mathcal{C}(\boldsymbol{x})$, $\boldsymbol{x} \in \Omega$; however, the explicit dependence is suppressed to keep the notation simple. Parameters associated with the pressure p and displacement $\boldsymbol{u}$ are given a subscript with the same symbol. The vector $\boldsymbol{f}_u$ is a given body force, while f_p is a given source term. The stiffness tensor is denoted $\mathcal{C}$, the Biot coupling coefficient α, the storage coefficient c_0, and the permeability $\mathcal{K}$. Indicated by subscripts, $\boldsymbol{g}$ represents Dirichlet and Neumann boundary conditions for displacement and pressure, while $\boldsymbol{n}$ is the outwards pointing normal vector. In this work, we use $\mathcal{C} : (\nabla \boldsymbol{u} + (\nabla \boldsymbol{u})^\top)/2 = G(\nabla \boldsymbol{u} + (\nabla \boldsymbol{u})^\top) + \Lambda \text{tr}(\nabla \boldsymbol{u}) I$, where G and Λ are the Lamé parameters. Traction can also be derived for other material laws.

The fracture boundary, Γ_C, is divided into a positive side Γ^+ and a negative side Γ^+. The choice of which side is positive and which is negative is arbitrary and will only make a difference in the implementation. For the fracture segments, a nonpenetration condition is enforced in the normal direction, meaning that the positive and negative sides cannot penetrate each other. In the tangential direction, a Coulomb friction law divides the contact region into a sliding part and a sticking part. To formulate these contact conditions, the normal vector for the contact region is defined as the normal vector of the positive side $\boldsymbol{n}(\boldsymbol{x}) = \boldsymbol{n}^+(\boldsymbol{x})$. Further, let

$$R : \Gamma^+ \to \Gamma^- \tag{3}$$

be a mapping that projects a point from the positive boundary onto the negative boundary as given by the normal vector. The gap function, which will appear in the nonpenetration condition, is then defined as

$$g(\boldsymbol{x}) = \|\boldsymbol{x} - R(\boldsymbol{x})\| \quad \boldsymbol{x} \in \Gamma^+,$$

where $\|\cdot\|$ is the Euclidean norm. Due to Newton's third law, the surface traction, $\boldsymbol{T} = \sigma \cdot \boldsymbol{n}$, on the contact boundaries must be equal up to the sign

$$\boldsymbol{T}^+(\boldsymbol{x}) = -\boldsymbol{T}^-(R(\boldsymbol{x})) \qquad \boldsymbol{x} \in \Gamma^+, \tag{4}$$

and we use the notation $\boldsymbol{T}_C = \boldsymbol{T}^+$. The surface traction is divided into a normal and tangential part by

$$T_n(\boldsymbol{x}) = \boldsymbol{T}_C(\boldsymbol{x}) \cdot \boldsymbol{n}(\boldsymbol{x}), \quad \boldsymbol{T}_\tau(\boldsymbol{x}) = \boldsymbol{T}_C(\boldsymbol{x}) - T_n(\boldsymbol{x})\boldsymbol{n}(\boldsymbol{x}) \qquad \boldsymbol{x} \in \Gamma^+, \tag{5}$$

and the displacement jump is defined as $[\boldsymbol{u}(\boldsymbol{x})] = \boldsymbol{u}(\boldsymbol{x}) - \boldsymbol{u}(R(\boldsymbol{x}))$ for $\boldsymbol{x} \in \Gamma^+$. The normal and tangential displacement jump is defined analogously to Equation (5):

$$[\boldsymbol{u}(\boldsymbol{x})]_n = [\boldsymbol{u}(\boldsymbol{x})] \cdot \boldsymbol{n}(\boldsymbol{x}), \quad [\boldsymbol{u}(\boldsymbol{x})]_\tau = [\boldsymbol{u}(\boldsymbol{x})] - [\boldsymbol{u}(\boldsymbol{x})]_n \boldsymbol{n}(\boldsymbol{x}) \qquad \boldsymbol{x} \in \Gamma^+.$$

The nonpenetration condition can now be formulated as

$$\begin{cases} [\boldsymbol{u}(\boldsymbol{x})]_n - g(\boldsymbol{x}) \leq 0 \\ T_n(\boldsymbol{x})([\boldsymbol{u}(\boldsymbol{x})]_n - g(\boldsymbol{x})) = 0 \\ T_n(\boldsymbol{x}) \leq 0 \end{cases} \qquad \boldsymbol{x} \in \Gamma^+, \tag{6}$$

where the first condition ensures that the two sides of the fracture cannot penetrate, the second ensures that either the normal traction is zero or the fracture sides are in contact, and the last enforces a negative normal component of the surface traction.

The tangential part of the surface traction is governed by a Coulomb friction law:

$$\begin{cases} \|\boldsymbol{T}_\tau(\boldsymbol{x})\| & \leq F(\boldsymbol{x})|T_n(\boldsymbol{x})| \\ \|\boldsymbol{T}_\tau(\boldsymbol{x})\| & < F(\boldsymbol{x})|T_n(\boldsymbol{x})| \ \rightarrow [\dot{\boldsymbol{u}}(\boldsymbol{x})]_\tau = 0 \\ \|\boldsymbol{T}_\tau(\boldsymbol{x})\| & = F(\boldsymbol{x})|T_n(\boldsymbol{x})| \ \rightarrow \exists\, \zeta \in \mathbb{R} : \boldsymbol{T}_\tau(\boldsymbol{x}) = -\zeta^2[\dot{\boldsymbol{u}}(\boldsymbol{x})]_\tau \end{cases} \qquad \boldsymbol{x} \in \Gamma^+, \tag{7}$$

where F is the coefficient of friction, and $\dot{\boldsymbol{u}}$ is the displacement velocity approximated by the backward Euler scheme, as given by Equation (2). The first equation gives the friction bound, the second ensures that if the friction bound is not reached, then the surface is sticking, and the last equation ensures that if the friction bound is reached, then the tangential sliding velocity is parallel to the tangential traction. In the static case, e.g., for the purely mechanical problem when $\alpha = 0$, the notion of a velocity does not exist. For these cases, it is common to replace the sliding velocity, $[\dot{\boldsymbol{u}}]_\tau$, by the displacement jump, $[\boldsymbol{u}]_\tau$, in Equation (7) [47].

For the fluid, the fractures are modeled as impermeable. This means that the fluid cannot flow in or across the fractures, i.e., $\boldsymbol{q}(\boldsymbol{x}) \cdot \boldsymbol{n}(\boldsymbol{x}) = 0,\ \boldsymbol{x} \in \Gamma_C$. To avoid excessive model complexity, we have chosen a model with impermeable fractures. For possible methods to extend this work to include fracture flow, we refer to the work by Dietrich et al [14], among others [44, 17, 32, 13].

3 Discretization

We define the triplet $(\mathcal{T}, \mathcal{F}, \mathcal{V})$ as the cells, faces and vertices of our mesh. It is assumed that the mesh conforms to the fractures; that is, the positive and negative sides of the fractures are tessellated by a subset of the faces of the mesh. Before the discretization is described, we need to define some notation, and we start by giving the relation between cells, faces and vertices using the standard notation for finite-volume methods [15, 37]:

- For a cell $K \in \mathcal{T}$, we denote its faces by $\mathcal{F}_K$ and its vertices by $\mathcal{V}_K$.
- For a face $\pi \in \mathcal{F}$, we denote the neighboring cells as $\mathcal{T}_\pi$ and its vertices as $\mathcal{V}_\pi$.
- For a vertex $v \in \mathcal{V}$, we denote the adjacent cells by $\mathcal{T}_v$ and the adjacent faces by $\mathcal{F}_v$.

In addition to the mesh triplet $(\mathcal{T}, \mathcal{F}, \mathcal{V})$, we define the so-called subcells and subfaces illustrated in Figure 2:

- For a vertex $v \in \mathcal{V}_K$, we define a subcell of K identified by (K, v) with a volume m_K^v such that $\sum_{v \in \mathcal{V}_K} m_K^v = m_K = \int_K \mathrm{d}\boldsymbol{x}$.
- For a vertex $v \in \mathcal{V}_\pi$, we associate a subface identified by (π, v) with an area m_π^v such that $\sum_{v \in \mathcal{V}_\pi} m_\pi^v = m_\pi = \int_\pi \mathrm{d}\boldsymbol{x}$.

The subfaces cannot be chosen arbitrary but should correspond to faces of the subcells; for the triplet (v, π, K), the intersection of the boundary of the subcell (K, v) and the face π should equal the subface $(\pi, v) = \partial(K, v) \cap \pi$. Further, all subcells and subfaces are assumed to have a positive measure. Note that in an abuse of notation, we use K for both indexing and the geometric object so that both $\mathcal{V}_K$ and $\int_K \mathrm{d}\boldsymbol{x}$ make sense. All subfaces $(\pi, v),\ \pi \in \mathcal{F},\ v \in \mathcal{V}_\pi$ are divided into three disjoint sets $\mathcal{P}, \mathcal{N}$, and $\mathcal{R}$, where $\mathcal{P}$ contains all subfaces located on the positive boundary Γ^+, $\mathcal{N}$ contains all subfaces located on the negative boundary Γ^-, and $\mathcal{R}$ contains the remaining subfaces.

Finally, for each element $K \in \mathcal{T}$, a cell center $\boldsymbol{x}_K \in K$ is defined, and for each subface (π, v), we associate a continuity point $\boldsymbol{x}_\pi^v$ located at any point on the subface, (π, v), however, the distance to the vertex v must be

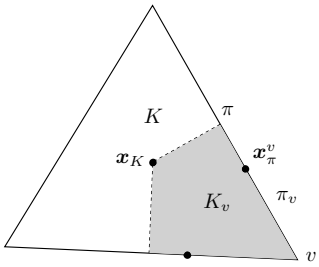

Figure 2: Notation used to describe the mesh. For a cell K, face π and vertex v of the mesh, we associate a subcell (K, v) and subface (π, v), as well as a cell center $\boldsymbol{x}_K$ and continuity point $\boldsymbol{x}_\pi^v$. In this figure, the cell is the full triangle, and the subcell is given by the gray area.

greater than zero. The unit normal for each face is denoted by $\boldsymbol{n}_\pi$, which is equal to the subface normal of the face $\boldsymbol{n}_\pi^v$. When it is necessary to distinguish the direction of the normal, it is defined as the outward pointing normal $\boldsymbol{n}_K^\pi$ of a cell $K \in \mathcal{T}_\pi$. Note that for a face π, we have $\mathcal{T}_\pi = \{K, L\}$, $\boldsymbol{n}_K^\pi = -\boldsymbol{n}_L^\pi$.

In the implementation used in the examples of this paper, the following construction is employed: The face- and cell-centers are chosen as the centroid of the corresponding face and cell. In 2d, the subface (π, v) is defined by the convex-hull of the vertex v and the face-center $\boldsymbol{x}_\pi$. In 3d, the subface is in addition defined by the midpoints of the edges of the face π that are connected to v. For simplices, this construction partition each face into a set of subfaces of equal area. The subcell (K, v) is defined by the convex-hull of the cell-center $\boldsymbol{x}_K$ and the subfaces $(\pi, v),\ \pi \in \mathcal{F}_v \cap \mathcal{F}_K$. The continuity point, $\boldsymbol{x}_\pi^v$, is taken to be one third the distance from the face-center to the vertex, $\boldsymbol{x}_\pi^v = \boldsymbol{x}_\pi - (\boldsymbol{x}_\pi - v)/3$. An example of this construction is shown in Figure 2.

3.1 Finite volume discretization

We use a finite volume discretization [37] to discretize the Biot Equations (1). This is based on two discrete variables, $\boldsymbol{u}_K$ and p_K, which are the cell-centered displacement and pressure, respectively. Within each subcell $(K, v),\ K \in \mathcal{T},\ v \in \mathcal{V}_K$, it is assumed that the displacements and pressures are linear in each subcell, and the discrete gradients are denoted by $(\bar{\nabla}\boldsymbol{u})_K^v$ and $(\bar{\nabla}p)_K^v$, where the bar over the gradient operator is added to distinguish it from the continuous gradients. For the mechanical stress, we adapt the notion of weak symmetry [26]; given the volume weighted average

$$\langle \Xi \rangle_v = \frac{1}{\sum_{K \in \mathcal{T}_v} m_K^v} \sum_{K \in \mathcal{T}_v} m_K^v \Xi_K^v,$$

associated with a vertex v, the discrete weakly symmetric mechanical stress is given by

$$\boldsymbol{\theta}_K^v = \mathcal{C}_K : (\bar{\nabla}\boldsymbol{u})_K^v - \frac{\left\langle \mathcal{C} : (\bar{\nabla}\boldsymbol{u}) \right\rangle_v - \left\langle \mathcal{C} : (\bar{\nabla}\boldsymbol{u}) \right\rangle_v^\top}{2}. \tag{8}$$

This is referred to as weak symmetry because

$$\left\langle \boldsymbol{\theta} - \boldsymbol{\theta}^\top \right\rangle_v = 0.$$

To simplify notation, the tensor $\mathcal{C}_K^v$ is referred to as the stress tensor, which acts to weakly symmetrize the stress:

$$\boldsymbol{\theta}_K^v = C_K^v : (\bar{\nabla}\boldsymbol{u})_K^v.$$

The expression $C_K^v : (\bar{\nabla}\boldsymbol{u})_K^v$ should not be interpreted as a single tensor vector product but as a weighted sum of products given by Equation (8).

Using the weak symmetry, the flux and traction over each subface given by the discrete variables can be stated as

$$q_{K,\pi}^v = -m_\pi^v \mathcal{K}_K (\bar{\nabla}p)_K^v \cdot \boldsymbol{n}_K^\pi, \tag{9}$$

$$\boldsymbol{T}_{K,\pi}^v = m_\pi^v (\mathcal{C}_K^v : (\bar{\nabla}\boldsymbol{u})_K^v - \alpha p_K I) \cdot \boldsymbol{n}_K^\pi. \tag{10}$$

For a spatially varying permeability and stress tensor, we use the cell-center value to evaluate the parameters $\mathcal{K}_K = \mathcal{K}(\boldsymbol{x}_K)$ for each cell.

The finite-volume scheme will be constructed such that the gradient unknowns can be eliminated by performing a local static condensation. The following presentation on how we obtain the numerical gradients is designed to reflect the computer implementation. This presentation is different from most classical papers on the used finite-volume discretization [1], however, it is mathematically equivalent. After the numerical gradients are expressed in terms of the cell-center unknowns, the finite volume structure of the discretization is obtained by enforcing mass/momentum conservation for each cell. The final scheme will be locally conservative and given by the cell-centered displacement and pressure. A detail that will be important when we introduce the hybrid discretization is the possibility of exactly reconstructing the discrete gradients, and thus also the flux and traction, from the cell-centered variables $\boldsymbol{u}$ and p.

The discrete fluid flux given in Equation (9) does not contain any dependence on the displacement, and it is identical to the fluid flux for the uncoupled fluid pressure, i.e., $\alpha = 0$. To discretize the flux, we use the MPFA-O scheme for simplices [30, 16]. Each subcell gradient $(\bar{\nabla} p)_K^v$ is associated with a fluid flux as given in (9). Conservation of mass is enforced for each internal subface. This requires the fluid flux for cells $(K, L) \in \mathcal{T}_\pi$ sharing a face π to be equal and opposite over each of their shared subfaces; that is,

$$- m_\pi^v \mathcal{K}_K (\bar{\nabla} p)_K^v \cdot \boldsymbol{n}_K^\pi = m_\pi^v \mathcal{K}_L (\bar{\nabla} p)_L^v \cdot \boldsymbol{n}_L^\pi. \tag{11}$$

The pressure is not required to be continuous across the whole subface. Instead, pressure continuity is enforced at the continuity points, $\boldsymbol{x}_\pi^v$, that is,

$$p_K + (\bar{\nabla} p)_K^v \cdot (\boldsymbol{x}_\pi^v - \boldsymbol{x}_K) = p_L + (\bar{\nabla} p)_L^v \cdot (\boldsymbol{x}_\pi^v - \boldsymbol{x}_L). \tag{12}$$

Here, we have made use of the assumption that the pressure is linear in each subcell to write the pressure at the continuity point $\boldsymbol{x}_\pi^v$ as a function of the cell center pressure p_K and gradient $(\bar{\nabla} p)_K^v$. If a subface is on the Neumann boundary, $\pi \subset \Gamma_{p,N}$, the flux over the subface is given by evaluating the boundary condition at the continuity point and multiply the value with the subface area:

$$- m_\pi^v \mathcal{K}_K (\bar{\nabla} p)_K^v \cdot \boldsymbol{n}_K^\pi = m_\pi^v g_{p,N}(\boldsymbol{x}_\pi^v). \tag{13}$$

If a subface is on the Dirichlet boundary, $\pi \subset \Gamma_{p,D}$, the pressure on the subface is given by

$$p_K + (\bar{\nabla} p)_K^v \cdot (\boldsymbol{x}_\pi^v - \boldsymbol{x}_K) = g_{p,D}(\boldsymbol{x}_\pi^v). \tag{14}$$

Faces on the fracture boundary, $(\pi, v) \subset \Gamma^+ \cup \Gamma^-$, is given a zero Neumann boundary condition as we have assumed impermeable fractures.

Around each vertex v we can now form a local linear system of equations from which the gradients $(\bar{\nabla} p)_K^v$, $K \in \mathcal{T}_v$ can be eliminated:

$$(\bar{\boldsymbol{\nabla}} \boldsymbol{p})_v = \begin{bmatrix} Q_p \\ D_{p,G} \end{bmatrix}^{-1} \left(\begin{bmatrix} \boldsymbol{g}_{p,N} \\ \boldsymbol{g}_{p,D} \end{bmatrix} - \begin{bmatrix} 0 \\ D_p \end{bmatrix} \boldsymbol{p} \right). \tag{15}$$

The first block $Q_p(\bar{\boldsymbol{\nabla}} \boldsymbol{p})_v = \boldsymbol{g}_{p,N}$ in this linear system is the collection of all flux balance Equations (11) and (13) for the vertex v. The next block $D_{p,G}(\bar{\boldsymbol{\nabla}} \boldsymbol{p})_v = \boldsymbol{g}_{p,D} - D_p \boldsymbol{p}$ collects all the pressure continuity Equations (12) and (14). Thus, $(\bar{\boldsymbol{\nabla}} \boldsymbol{p})_v$ is the vector of the subcell gradients $(\bar{\nabla} p)_K^v$, the matrix Q_p represents products of the form $m_\pi^v \boldsymbol{n}_K^\pi \mathcal{K}_K$, the matrix $D_{p,G}$ represents the distances $\boldsymbol{x}_\pi^v - \boldsymbol{x}_K$, the vectors $\boldsymbol{g}_{p,N}$ and $\boldsymbol{g}_{p,D}$ are possible boundary conditions, and D_p has entries 1 for p_K^v and -1 for p_L^v.

The elimination of the displacement gradients $(\bar{\nabla} \boldsymbol{u})_K^v$ is similar to the elimination of the pressure gradients $\bar{\nabla} p_K^v$. First, the continuity of traction gives us for each internal subface

$$m_\pi^v (\mathcal{C}_K^v : (\bar{\nabla} \boldsymbol{u})_K^v - \alpha p_K I) \cdot \boldsymbol{n}_K^\pi = -m_\pi^v (\mathcal{C}_L^v : (\bar{\nabla} \boldsymbol{u})_L^v - \alpha p_L I) \cdot \boldsymbol{n}_L^\pi. \tag{16}$$

It is worth pointing out that, for internal faces, the averaging part of the operator $\mathcal{C}_K^v : (\bar{\nabla} \boldsymbol{u})_K^v$ is the same on the right- and left-hand sides. Thus, the balance of traction can be written as

$$m_\pi^v (\mathcal{C}_K : (\bar{\nabla} \boldsymbol{u})_K^v - \alpha p_K I) \cdot \boldsymbol{n}_K^\pi = -m_\pi^v (\mathcal{C}_L : (\bar{\nabla} \boldsymbol{u})_L^v - \alpha p_L I) \cdot \boldsymbol{n}_L^\pi.$$

However, for boundary faces, the complete Equation (16) must be used. Unlike the fluid fluxes in (9), the traction is different from the uncoupled system due to the term $\alpha p_K I$. It is important to include the Biot stress in the local systems to obtain the correct force balance in our method [37]. We will see later that this approach also gives a higher-order term in the mass balance for the fluid, which acts analogously to the stabilization terms in other colocated schemes. For the fluid pressure, displacement continuity is enforced at the continuity points $\boldsymbol{x}_\pi^v$:

$$\boldsymbol{u}_K + (\bar{\nabla}\boldsymbol{u})_K^v(\boldsymbol{x}_\pi^v - \boldsymbol{x}_K) = \boldsymbol{u}_L + (\bar{\nabla}\boldsymbol{u})_L^v(\boldsymbol{x}_\pi^v - \boldsymbol{x}_L). \tag{17}$$

For a subface on the Neumann boundary, $(\pi, v) \subset \Gamma_{u,N}$, the boundary condition is evaluated at the continuity point and multiplied with the subface area:

$$m_\pi^v(\mathcal{C}_K^v : (\bar{\nabla}\boldsymbol{u})_K^v - \alpha p_K I) \cdot \boldsymbol{n}_K^\pi = m_\pi^v \boldsymbol{g}_{u,N}(\boldsymbol{x}_\pi^v), \tag{18}$$

For a subface on the Dirichlet boundary $(\pi, v) \subset \Gamma_{u,D}$ the displacement vector at the continuity point is given:

$$\boldsymbol{u}_K + (\bar{\nabla}\boldsymbol{u})_K^v(\boldsymbol{x}_\pi^v - \boldsymbol{x}_K) = \boldsymbol{g}_{u,D}(\boldsymbol{x}_\pi^v). \tag{19}$$

Subfaces on the fracture boundary is given a Neumann condition defined by the Lagrange multiplier:

$$\begin{aligned} m_\pi^v(\mathcal{C}_K^v : (\bar{\nabla}\boldsymbol{u})_K^v - \alpha p_K I) \cdot \boldsymbol{n}_K^\pi &= m_\pi^v \boldsymbol{\lambda}_\pi^v && (\pi, v) \in \mathcal{P}, \\ m_\pi^v(\mathcal{C}_K^v : (\bar{\nabla}\boldsymbol{u})_K^v - \alpha p_K I) \cdot \boldsymbol{n}_K^\pi &= -m_\pi^v \boldsymbol{\lambda}(R^{-1}(\boldsymbol{x}_\pi^v)) && (\pi, v) \in \mathcal{N}. \end{aligned} \tag{20}$$

The contribution to the negative side $-\boldsymbol{\lambda}(R^{-1}(\boldsymbol{x}_\pi^v))$ is just the mapping onto the Lagrange multiplier on the corresponding positive subface as given by Equation (3).

A local elimination of the displacement gradients $(\bar{\nabla}\boldsymbol{u})_K^v$ can now be done around each vertex to express them in terms of the cell-center displacement and pressure:

$$(\bar{\boldsymbol{\nabla}}\boldsymbol{u})_{\boldsymbol{v}} = \begin{bmatrix} Q_u \\ D_{u,G} \end{bmatrix}^{-1} \left(\begin{bmatrix} \boldsymbol{g}_{u,N} \\ \boldsymbol{g}_{u,D} \end{bmatrix} - \begin{bmatrix} P & 0 & -M_\pm \\ 0 & D_U & 0 \end{bmatrix} \begin{bmatrix} \boldsymbol{p} \\ \boldsymbol{u} \\ \boldsymbol{\lambda} \end{bmatrix} \right), \tag{21}$$

The variable $(\bar{\boldsymbol{\nabla}}\boldsymbol{u})_{\boldsymbol{v}}$ is the vector of the displacement gradients, $(\bar{\nabla}\boldsymbol{u})_K^v$, around the vertex v, the matrix Q_u represents products of the form $m_\pi^v \boldsymbol{n}^\top \mathcal{C}_K^v$, the matrix $D_{u,G}$ represents the same distance vectors as in (15), the vectors $\boldsymbol{g}_{u,N}$ and $\boldsymbol{g}_{u,D}$ are possible boundary conditions, and D_u is a matrix with entries ± 1. The term P is the only difference between the coupled and uncoupled system and contains products of the form $m_\pi^v \alpha I \boldsymbol{n}_\pi^v$, and the matrix $M_\pm$ contains the positive areas m_π^v for the positive subfaces and the negative areas $-m_\pi^v$ for the negative subfaces and represents the Lagrange multiplier contribution to the traction balance in Equation (20).

The finite-volume discretization of fluid flow is then obtained by expressing the fluid mass conservation over each cell K in terms of the discrete variables,

$$\sum_{\pi \in \mathcal{F}_K} \sum_{v \in \mathcal{V}_\pi} -m_\pi^v \mathcal{K}_K (\bar{\nabla} p)_K^v \cdot \boldsymbol{n}_K^\pi + \sum_{v \in \mathcal{V}_K} [m_K^v \alpha (\bar{\nabla} \cdot \dot{\boldsymbol{u}})_K^v + c_0 m_K^v \dot{p}_K] = \int_K f_p \, \mathrm{d}\boldsymbol{x}. \tag{22}$$

The pressure gradient $(\bar{\nabla} p)_K^v$ and displacement divergence $(\bar{\nabla} \cdot \boldsymbol{u})_K^v = \mathrm{tr}(\bar{\nabla}\boldsymbol{u})_K^v$ are obtained as linear functions of the cell-centered pressures and displacements and Lagrange multipliers from the local systems given in (15) and (21). The appearance of the pressure in the discrete displacement divergence is essential for the consistency of the method and is similar to the artificially introduced stability terms in other methods; see, e.g., Gaspar et al [18].

For the mechanics, momentum is conserved for all cells K,

$$-\sum_{\pi \in \mathcal{F}_K} \sum_{v \in \mathcal{V}_\pi} m_\pi^v \mathcal{C}_K^v : (\bar{\nabla}\boldsymbol{u})_K^v \cdot \boldsymbol{n}_K^\pi = \int_K \boldsymbol{f} \, \mathrm{d}V. \tag{23}$$

Note that the term $\alpha p_K I$ from the Biot stress in (10) sums to zero over a cell due to Gauss's theorem; however, the pressure dependence on the subcell gradients gives the correct fluid pressure contribution to the mechanics. Similarly, the dependence of the Lagrange multiplier on the subcell gradients gives the correct force contribution to the momentum balance.

To summarize, the finite volume scheme is constructed by defining a set of discrete pressure and displacement gradients for each subcell. Flux and pressure continuity is enforced over each subface for the fluid, and traction and displacement continuity is enforced for each subface for the solid. This defines a small local system around each node from which the pressure and displacement gradients can be expressed as a linear combination of the cell-centered pressure and displacement, and Lagrange multiplier and then eliminated. A stable coupling between the fluid and solid is achieved by considering the Biot stress, i.e., $\mathcal{C} : (\nabla \boldsymbol{u} + (\nabla \boldsymbol{u})^\top)/2 - \alpha p I$, for traction balance of the local systems.

3.2 Hybrid formulation

To solve the contact conditions (6) and (7), we apply the active-set strategy, which is equivalent to a semismooth Newton method described by Hüeber et al [22]. See also the paper by Wohlmuth [47]. We recapitulate the solution strategy in this section for the completeness of this paper. The main difference in our approach is how the Lagrange multipliers, which represent the surface traction, are coupled to the displacement unknowns in the surrounding domain. In our finite volume scheme, the Lagrange multipliers enter into the local equations for the displacement gradients.

A set of Lagrange multipliers is defined on the positive subface boundaries

$$\boldsymbol{\lambda}_\pi^v = \sigma_\pi^v \cdot \boldsymbol{n}_\pi^v, \qquad (\pi, v) \in \mathcal{P}.$$

The normal $\lambda_{\pi n}^v$ and tangential $\boldsymbol{\lambda}_{\pi\tau}^v$ components of the Lagrange multiplier are defined analogously to (5). The displacement on the subfaces, $\boldsymbol{u}_\pi^v$, is obtained as in Equation (19) for local systems.

The discrete formulation of the nonpenetration condition (6) can for each subface be written as

$$\begin{cases} [\boldsymbol{u}_\pi^v]_n - g_\pi^v \le 0 \\ \lambda_{\pi n}^v([\boldsymbol{u}_\pi]_n^v - g_\pi^v) = 0 \\ \lambda_{\pi n}^v \le 0 \end{cases} \qquad (\pi, v) \in \mathcal{P}, \tag{24}$$

and the static Coulomb friction (7) as

$$\begin{cases} \|\boldsymbol{\lambda}_{\pi\tau}^v\| & \le F_\pi^v |\lambda_{\pi n}^v| \\ \|\boldsymbol{\lambda}_{\pi\tau}^v\| & < F_\pi^v |\lambda_{\pi n}^v| \ \rightarrow [\dot{\boldsymbol{u}}_\pi^v]_\tau = 0 \\ \|\boldsymbol{\lambda}_{\pi\tau}^v\| & = F_\pi^v |\lambda_{\pi n}^v| \ \rightarrow \exists \zeta \in \mathbb{R} : \boldsymbol{\lambda}_{\pi\tau}^v = -\zeta^2 [\dot{\boldsymbol{u}}_\pi^v]_\tau \end{cases} \qquad (\pi, v) \in \mathcal{P}. \tag{25}$$

Recall that for the static case, the sliding velocity is replaced by the displacement jump, $[\boldsymbol{u}_\pi^v]_\tau$. We define $b_\pi^{v,k} = F_\pi^v(-\lambda_{\pi n}^{v,k} + c([\boldsymbol{u}_\pi^{v,k}]_n - g_\pi^v))$, which can be interpreted as the friction bound. The nonpenetration condition can now be rewritten as the nonlinear complementary function

$$C_n([\boldsymbol{u}_\pi^v]_n, \lambda_{\pi n}^v) = -\lambda_{\pi n}^v - \frac{1}{F_\pi^v} \max\{0, b_\pi^{v,k}\}, \tag{26}$$

where $c > 0$ is a given numerical parameter and $\max\{\cdot,\cdot\}$ is the maximum function. Similarly, we can now rewrite the Coulomb friction as the complementary function

$$\boldsymbol{C}_\tau([\dot{\boldsymbol{u}}_\pi^v], \boldsymbol{\lambda}_{\pi\tau}^v) = \max\{b_\pi^{v,k}, \|-\boldsymbol{\lambda}_{\pi\tau}^v + c[\boldsymbol{u}_\pi^v]_\tau\|\}(-\boldsymbol{\lambda}_{\pi\tau}^v) - \max\{0, b_\pi^{v,k}\}(-\boldsymbol{\lambda}_{\pi\tau}^v + c[\dot{\boldsymbol{u}}_\pi^v]_\tau). \tag{27}$$

The solution pair $(\boldsymbol{u}_\pi^v, \boldsymbol{\lambda}_\pi^v)$ satisfies the nonpenetrating condition (24) and Coulomb law (25) if and only if $C_n([\boldsymbol{u}_\pi^v]_n, \lambda_{\pi n}^v) = 0$ and $\boldsymbol{C}_\tau([\dot{\boldsymbol{u}}_\pi^v], \boldsymbol{\lambda}_\pi^v) = \boldsymbol{0}$. We apply a semismooth Newton method to this problem, which results in an active set method. Given the solution $(\boldsymbol{u}^k, \boldsymbol{\lambda}^k)$ from the previous Newton iteration, we divide the contact subfaces into three disjoint sets:

$$\begin{aligned} \mathcal{I}_n^{k+1} &= \{(\pi, v) \in \mathcal{P} : b_\pi^{v,k} \le 0\} \\ \mathcal{I}_\tau^{k+1} &= \{(\pi, v) \in \mathcal{P} : \|-\boldsymbol{\lambda}_{\pi\tau}^{v,k} + c[\dot{\boldsymbol{u}}_\pi^{v,k}]_\tau\| - b_\pi^{v,k} < 0\} \\ \mathcal{A}^{k+1} &= \{(\pi, v) \in \mathcal{P} : \|-\boldsymbol{\lambda}_{\pi\tau}^{v,k} + c[\dot{\boldsymbol{u}}_\pi^{v,k}]_\tau\| \ge b_\pi^{v,k} > 0\}. \end{aligned} \tag{28}$$

The first set contains the subfaces not in contact. The second set contains the subfaces in contact whose friction bound is not reached, i.e., they are sticking. The third set contains the subfaces in contact where the friction bound

is reached, i.e., they are sliding. The new iterates $([\boldsymbol{u}_\pi^{v,k+1}]_\tau, \boldsymbol{\lambda}_{\pi\tau}^{v,k+1})$ in the semismooth Newton scheme are then calculated depending on which set the subface belongs to. The update is found by calculating the derivative of the complementary functions C_n and $\boldsymbol{C}_\tau$ for each of the three sets. For the subfaces not in contact, zero traction is enforced

$$\boldsymbol{\lambda}_\pi^{v,k+1} = \mathbf{0} \qquad (\pi, v) \in \mathcal{I}_n^{k+1}. \tag{29}$$

For the subfaces in contact and sticking, we enforce

$$[u_{\pi n}^{v,k+1}] = g_\pi^v, \qquad [\dot{\boldsymbol{u}}_\pi^{v,k+1}]_\tau + \frac{F_\pi^v [\dot{\boldsymbol{u}}_\pi^{v,k}]_\tau}{b_\pi^{v,k}} \lambda_{\pi n}^{v,k+1} = [\dot{\boldsymbol{u}}_\pi^{v,k}]_\tau \qquad (\pi, v) \in \mathcal{I}_\tau^{k+1}. \tag{30}$$

In the normal direction, this enforces the condition that the negative and positive subfaces must be in contact in the next iteration $k+1$. In tangential direction the enforced condition is dependent on the previous Newton iteration. If the subface sliding velocity was zero in the previous iteration, $[\dot{\boldsymbol{u}}_\pi^{v,k}] = \mathbf{0}$, Equation (30) enforces the condition that the tangential velocity is zero in the next iteration, $[\dot{\boldsymbol{u}}_\pi^{v,k+1}] = \mathbf{0}$. If the subface sliding velocity was different from zero in the previous iteration, the Newton update does not immediately enforce zero sliding velocity, however, as the algorithm converges we have $F_\pi^v \lambda_{\pi n}^{v,k+1} = b_\pi^{v,k}$, and the sliding velocity, $[\dot{\boldsymbol{u}}_\pi^k]$, for the sticking subfaces is set to zero. For subfaces in contact and sliding, we enforce

$$\begin{aligned} [\boldsymbol{u}_\pi^{v,k+1}]_n &= g_\pi^v, \\ \boldsymbol{\lambda}_{\pi\tau}^{v,k+1} + L_\pi^{v,k} [\dot{\boldsymbol{u}}_\pi^{v,k+1}]_\tau + F_\pi^v \boldsymbol{v}_\pi^{v,k} \lambda_{\pi n}^{v,k+1} &= \boldsymbol{r}_\pi^{v,k} + b_\pi^{v,k} \boldsymbol{v}_f^k, \end{aligned} \qquad (\pi, v) \in \mathcal{A}^{k+1}. \tag{31}$$

Again, this enforces the condition that the negative and positive subfaces be in contact at the next iteration $k+1$. In the tangential direction, the condition approximates the sliding direction and distance. The matrices and vectors are:

$$\begin{aligned} L_\pi^{v,k} &= c((I_{d-1} - M_\pi^{v,k})^{-1} - I_{d-1}) \\ \boldsymbol{v}_\pi^{v,k} &= (I_{d-1} - M_\pi^{v,k})^{-1} \frac{-\boldsymbol{\lambda}_{\pi\tau}^{v,k} + c[\dot{\boldsymbol{u}}_\pi^{v,k}]_\tau}{\|-\boldsymbol{\lambda}_{\pi\tau}^{v,k} + c[\dot{\boldsymbol{u}}_\pi^{v,k}]_\tau\|} \\ \boldsymbol{r}_\pi^{v,k} &= -(I_{d-1} - M_\pi^{v,k})^{-1} e_\pi^{v,k} Q_\pi^{v,k} (-\boldsymbol{\lambda}_{\pi\tau}^{v,k} + c[\dot{\boldsymbol{u}}_\pi^{v,k}]_\tau), \end{aligned} \tag{32}$$

where I_{d-1} is the $(d-1 \times d-1)$ identity matrix and $M_\pi^{v,k} = e_\pi^{v,k}(I_{d-1} - Q_\pi^{v,k})$ with

$$Q_\pi^{v,k} = \frac{-\boldsymbol{\lambda}_{\pi\tau}^{v,k}(-\boldsymbol{\lambda}_{\pi\tau}^{v,k} + c[\dot{\boldsymbol{u}}_\pi^{v,k}]_\tau)^\top}{b_\pi^{v,k}\|-\boldsymbol{\lambda}_{\pi\tau}^{v,k} + c[\dot{\boldsymbol{u}}_\pi^{v,k}]_\tau\|}, \qquad e_\pi^{v,k} = \frac{b_\pi^{v,k}}{\|-\boldsymbol{\lambda}_{\pi\tau}^{v,k} + c[\dot{\boldsymbol{u}}_\pi^{v,k}]_\tau\|}.$$

Regularization

For the subfaces in the inactive set $\mathcal{I}_n^{k+1}$, i.e., the subfaces not in contact, the Newton update gives a homogeneous Neumann boundary condition. For the subfaces in the contact sets $\mathcal{I}_\tau^{k+1}$ and $\mathcal{A}^{k+1}$, the Newton update gives a Dirichlet condition in the normal direction and a Robin boundary condition in the tangential direction. This Robin condition guarantees positive definiteness of the system only if $L_\pi^{v,k}$, defined by Equation (32), is positive definite. In the converged limit, the matrix $L_\pi^{v,k}$ is a positive definite matrix [22]. However, during the iterations, there is no guarantee that this will hold. We therefore add a regularization to the Robin conditions by replacing $Q_\pi^{v,k}$ by

$$\tilde{Q}_\pi^{v,k} = \frac{-\boldsymbol{\lambda}_{\pi\tau}^{v,k}(-\boldsymbol{\lambda}_{\pi\tau}^{v,k} + c[\dot{\boldsymbol{u}}_\pi^{v,k}]_\tau)^\top}{\max(b_\pi^{v,k}, \|\boldsymbol{\lambda}_{\pi\tau}^{v,k}\|)\|-\boldsymbol{\lambda}_{\pi\tau}^{v,k} + c[\dot{\boldsymbol{u}}_\pi^{v,k}]_\tau\|},$$

which is only different from $Q_\pi^{v,k}$ when the inequalities in Equation (25) are violated. Further, we define

$$\alpha_\pi^{v,k} = \frac{(-\boldsymbol{\lambda}_{\pi\tau}^{v,k})^\top(-\boldsymbol{\lambda}_{\pi\tau}^{v,k} + c[\dot{\boldsymbol{u}}_\pi^{v,k}]_\tau)}{\|\boldsymbol{\lambda}_{\pi\tau}^{v,k}\|\|-\boldsymbol{\lambda}_{\pi\tau}^{v,k} + c[\dot{\boldsymbol{u}}_\pi^{v,k}]_\tau\|}, \qquad \delta_\pi^{v,k} = \min\left(\frac{\|\boldsymbol{\lambda}_{\pi\tau}^{v,k}\|}{\lambda_{\pi n}^{v,k}}, 1\right),$$

and

$$\beta_\pi^{v,k} = \begin{cases} \frac{1}{1-\alpha_\pi^{v,k}\delta_\pi^{v,k}}, & \text{if } \alpha_\pi^{v,k} < 0 \\ 1, & \text{otherwise.} \end{cases}$$

Using the notation that tilde ($\tilde{\cdot}$) denotes the regularization, we have $\tilde{M}_\pi^{v,k} = e_\pi^{v,k}(I_{d-1} - \tilde{Q}_\pi^{v,k})$ and replace the matrix $L_\pi^{v,k}$ from Equation (32) by

$$\tilde{L}_\pi^{v,k} = c((I_{d-1} - \beta_\pi^{v,k}\tilde{M}_\pi^{v,k}) - I_{d-1}),$$

which guarantees its positive definiteness [22]. As the iterates $(\boldsymbol{u}^k, \boldsymbol{\lambda}^k)$ converge to the solution, the regularization $\tilde{Q}_\pi^{v,k} \to Q_\pi^{v,k}$, $\tilde{L}_\pi^{v,k} \to L_\pi^{v,k}$, and $\beta_\pi^{v,k} \to 1$, and we obtain the original system of equations.

3.3 Discrete system of equations

We end Section 3 with a summary of the discrete system of equations that is solved at each Newton iteration, and we state the discrete linearized version of Equations (1)-(7) as:

$$\begin{aligned} A\boldsymbol{u} + B\boldsymbol{p} + C\boldsymbol{\lambda} &= \boldsymbol{b}_u, \\ D\boldsymbol{u} + E\boldsymbol{p} + F\boldsymbol{\lambda} &= \boldsymbol{b}_p, \\ G\boldsymbol{u} + H\boldsymbol{p} + J\boldsymbol{\lambda} &= \boldsymbol{r}. \end{aligned} \tag{33}$$

The first line is the discrete momentum balance, and the matrices A, B, C, and the vector $\boldsymbol{b}_u$ are obtained by considering Equation (23) for all cells and assembling the coefficients in the global matrices. Similarly, the second row corresponds to the discrete flux balance, and the equation is obtained by considering Equation (22) over all cells and assembling the coefficients in the global matrices. The matrix F appears due to the dependence on $\boldsymbol{\lambda}$ in the local systems for the displacement gradients, as given by Equation (21). It is worth pointing out that the matrices A, B, D, and E are the same matrices as are obtained by the finite-volume scheme in a poroelastic domain without any fractures [37]. The last row of Equation (33) corresponds to the linearization of the complementary functions (26) and (27), and the matrices are obtained by assembling Equations (29)-(31) for each subface on the fracture. The dependence of the pressure in the contact law, given by the matrix H, is due to the pressure dependence on the poroelastic stress (see second row of Equation 1) as well as the pressure dependence on the displacement gradients given by Equation (21).

From a computational point of view, it is worth noting that during the Newton iteration, only the matrices G, H, J, and the vector $\boldsymbol{r}$ will change. This means that updating the discretization is inexpensive as it is only a local update for the subcells bordering the fractures.

4 Numerical examples

Four numerical examples are given. For the first two, we neglect the fluid contribution to the mechanical stress to investigate the performance of the numerical approach for the purely mechanical contact problem, i.e., we set $\alpha = 0$. In all of the examples, Young's modulus is $E_0 = 4$ GPa, the Poisson ratio is $\nu = 0.2$, and the initial gap of the fractures is $g = 0$. In our experience, the algorithm is quite robust with respect to the numerical parameter c, and in the examples, it is fixed to $c = 100$ GPa/m.

We assign a space varying coefficient of friction so that the slip of the fractures will arrest before it reaches the fracture tips. This choice of the friction coefficient is done to obtain a solution with high enough regularity to study the convergence in stress. If the slip of the fractures reaches the fracture tips, the solution will contain singularities in the stress, which reduces the regularity of our solution. Note that our method is not restricted to the regularized solution, as discussed more thoroughly in Appendix A.

The discrete solution is denoted $\boldsymbol{u}_h$, which is interpreted as the piecewise constant function over each cell $K \ni \boldsymbol{x}$ such that $\boldsymbol{u}_h(\boldsymbol{x}) = \boldsymbol{u}_K$. The discrete solution $\boldsymbol{\lambda}_h$ for the Lagrange multiplier is defined as piecewise constant on each face π on Γ^+ and is equal to the area weighted sum of the subface values, $\boldsymbol{\lambda}_h(\boldsymbol{x})m_\pi = \sum_{v\in\mathcal{V}_\pi} m_\pi^v \lambda_\pi^v$, $\boldsymbol{x} \in \pi$. Likewise, the displacement jump is defined as the piecewise constant on each face, π, on Γ^+ corresponding to the subface average, $[\boldsymbol{u}_h(\boldsymbol{x})] = \frac{1}{|\mathcal{V}_\pi|}\sum_{v\in\mathcal{V}_\pi}[\boldsymbol{u}_\pi^v]$, $\boldsymbol{x} \in \pi$, where $|\mathcal{V}_\pi|$ is the number of subfaces of the face, π, which is equal to three if π is a triangle. The continuous solution is denoted by the pair $(\boldsymbol{u}, \boldsymbol{\lambda})$.

We define the relative error of a discrete variable ξ_h in a domain γ as

$$\varepsilon_\gamma(\xi_h, \xi) = \frac{\|\boldsymbol{\xi}_h - \boldsymbol{\xi}\|_\gamma}{\|\boldsymbol{\xi}\|_\gamma}, \tag{34}$$

where ξ is a reference solution and $||\cdot||_\gamma$ is the L_2 norm over the domain γ. The Newton iteration is terminated when the change in the solution is below a given stopping criterion:

$$\varepsilon_\Omega(\boldsymbol{u}_h^{k+1}, \boldsymbol{u}_h^k) < \delta, \tag{35}$$

where k is the Newton iteration index.

To solve the linear system of equations at each Newton iteration, a direct solver is used if the number of degrees of freedom is less than 10 000, else, an iterative solver is used. The iterative solver uses a preconditioned GMRES iteration that is based on a Schur complement strategy, where the mechanics-fluid subsystem is approximated by a single fixed stress iteration, see [29, 10] for details. Within the fixed stress iteration, the mechanics problem is solved by one AMG iteration, as implemented in [39], while a direct solver is applied to the flow problem. In the simpler case of a pure mechanics problem, the fixed stress iteration is replaced with an AMG iteration on the mechanics subproblem.

The computer code has been implemented in the open source Python toolbox PorePy [25], which has an interface for meshing in Gmsh [19]. The run scripts for the examples are open source [7]. ParaView [3] was used to make Figures 3 and 7.

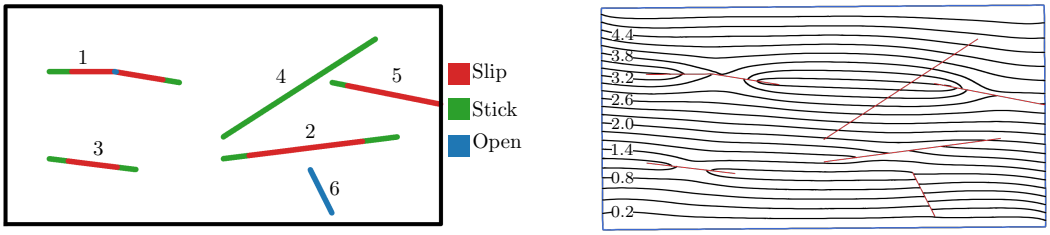

Figure 3: The fractured domain from Example 1. Left: The black box corresponds to the domain boundaries, while the fractures, labeled by a number, are represented by lines. The fractures are colored in three colors; segments that slip are red, segments that stick are green, and segments that open are blue. Right: Contour plot of the x-component of the displacement $\boldsymbol{u}$. The labels on the contours are given in millimeters. The red lines represent the fractures.

4.1 Example 1

The first example is a domain 2 m $\times$ 1 m with six fractures, as depicted in Figure 3. This example includes difficult cases such as a fracture with a kink and a fracture reaching the boundary. An advantage of our finite volume method is that no special treatment is needed to handle these cases because the degrees of freedom are located in the cell and subface centers and not on the nodes. In this example, we do not consider any fluid and solve only for the linear elasticity in Equation (1) coupled to the contact conditions given in Equations (6) and (7). The bottom boundary is fixed, the two vertical boundaries are free, and at the top boundary a Dirichlet condition $\boldsymbol{g}_{u,D} = [0.005, -0.002]^\top$ m is assigned. The initial guess in the Newton iteration is $\boldsymbol{u} = \boldsymbol{0}$ m, $\lambda_n = -100$ Pa and $\boldsymbol{\lambda}_\tau = \boldsymbol{0}$ Pa, i.e., zero displacement and all fractures in contact and sticking. The coefficient of friction is for each fracture $i = 1 \ldots 6$ set to $F_i(\boldsymbol{x}) = 0.5(1 + \exp(-D_i(\boldsymbol{x})^2/0.005\text{m}^2))$, $\boldsymbol{x} \in \Gamma_i^+$, where $D_i(\boldsymbol{x})$ is the distance from $\boldsymbol{x}$ to the tips of fracture i. Note that the bend in Fracture 1 and the right end of Fracture 5 are not considered tips for the distance function D, and thus the coefficient of friction at these points is $F \approx 0.5$.

A contour plot of the solution is shown in Figure 3 where the discontinuous displacement over the sliding or opening fractures can clearly be seen. To better visualize the different behaviors of the fractures, the fracture regions that are slipping, sticking, and opening are plotted in different colors in Figure 3. For Fracture 1, the top boundary is sliding to the right, while the bottom boundary is sliding to the left. This situation causes the fracture to open in a small segment after the bend. Figure 4 shows the shear component of the Lagrange multiplier as well as the friction bound and displacement jump. At the bend of fracture 1, there is a singularity in the stress that causes the sharp increase in the Lagrange multiplier. For Fracture 2, we observe a change in the shear and normal component of the Lagrange multiplier at approximately the midpoint that is caused by the opening of Fracture 6. In the vicinity of the fracture tips, there is a sharp increase in the shear component of the Lagrange multiplier as the fractures change behavior from sliding to sticking.

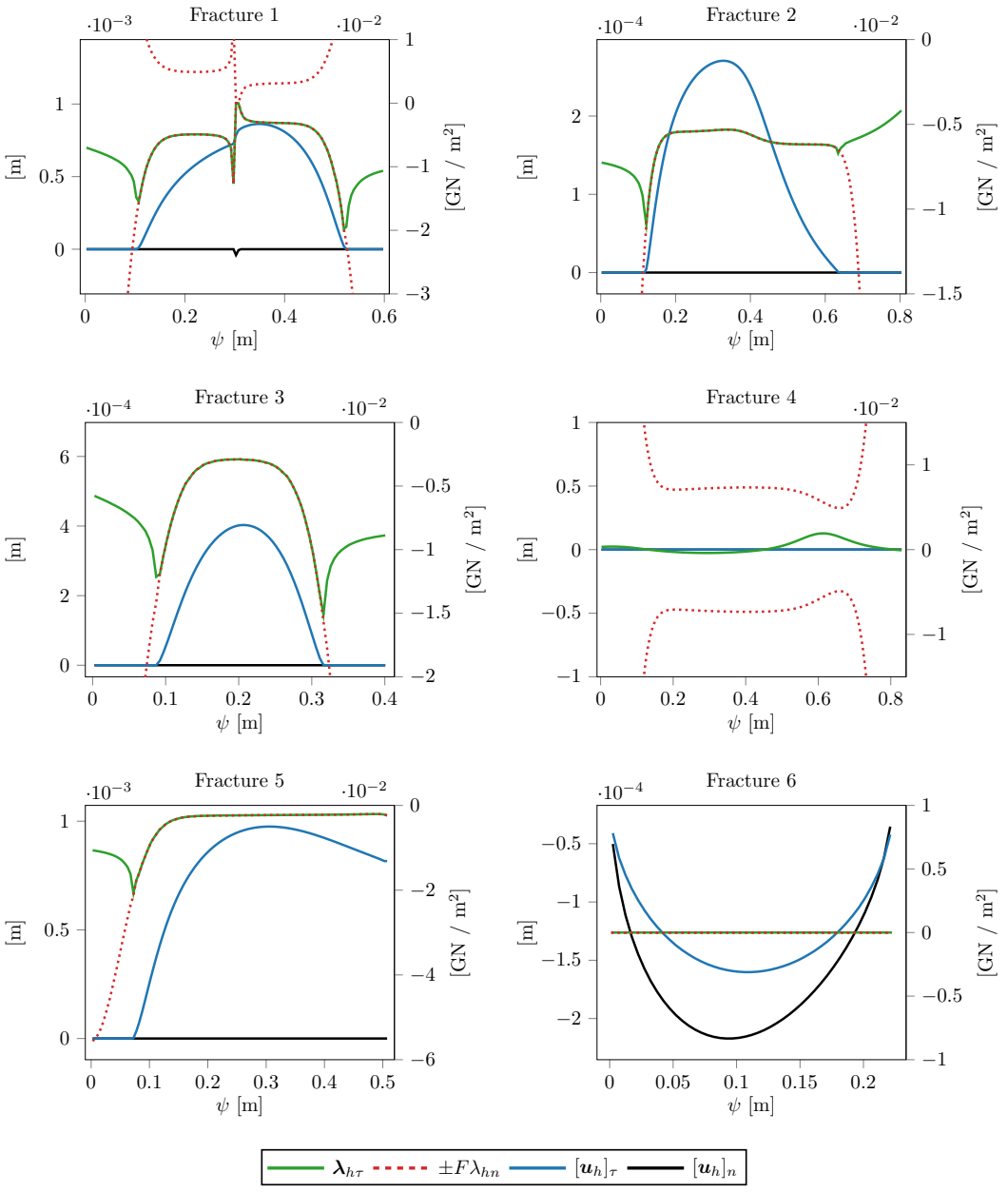

Figure 4: Results from Example 1 showing $\boldsymbol{\lambda}_h$ and $[\boldsymbol{u}_h]$ for the reference solution that has an average of 103 faces along each fracture. The shear component of the Lagrange multiplier $\boldsymbol{\lambda}_{h\tau}$ (green), friction bound $\pm F\lambda_{hn}$ (red dashes), tangential displacement jump $[\boldsymbol{u}_h]_\tau$ (blue), and normal displacement jump $[\boldsymbol{u}_h]_n$ (black) for all fractures. The x-axis shows the distance ψ from the leftmost end of the fracture. The subplots are arranged from top left to bottom right according to the fracture number given in Figure 3.

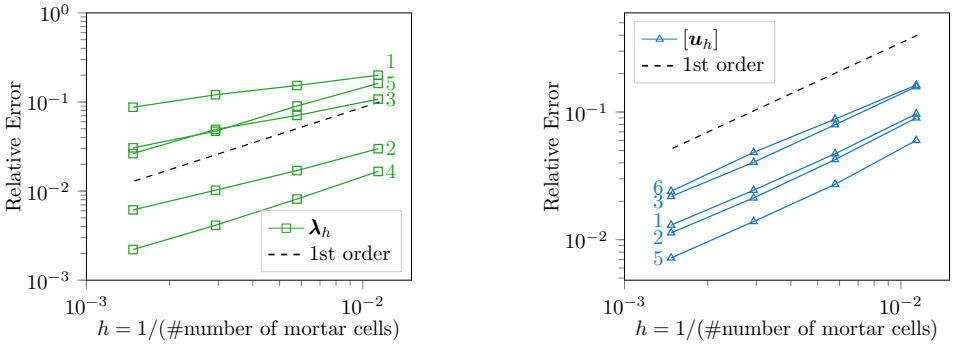

Figure 5: Convergence rates for the Lagrange multiplier $\boldsymbol{\lambda}_h$ (left) and the displacement jump $[\boldsymbol{u}_h]$ (right) for each separate fracture in Example 1. The error is measured as the relative errors $\varepsilon_{\Gamma_i^+}([\boldsymbol{u}_h], [\boldsymbol{u}])$ and $\varepsilon_{\Gamma_i^+}(\boldsymbol{\lambda}_h, \boldsymbol{\lambda})$ for each fracture Γ_i^+. The line numbering corresponds to the fracture numbers given in Figure 3.

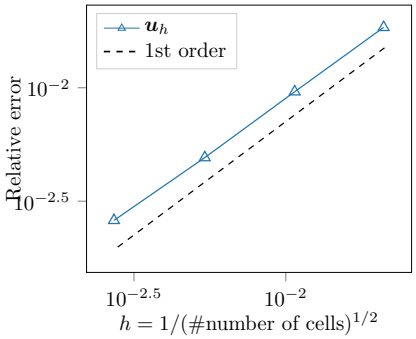

Figure 6: Convergence rates for the cell-centered displacement in Example 1. The error is the relative error $\varepsilon_\Omega(\boldsymbol{u}_h, \boldsymbol{u})$, as defined by Equation (34).

As a reference solution $(\boldsymbol{u}, \boldsymbol{\lambda})$, we use the solution calculated for a fine mesh using 1.7 million degrees of freedom. The second finest mesh has 270 thousand degrees of freedom and is the mesh used for the results in Figure 4 and 3 . In Figure 5, the relative errors $\varepsilon_{\Gamma_i^+}([\boldsymbol{u}_h], [\boldsymbol{u}])$ and $\varepsilon_{\Gamma_i^+}(\boldsymbol{\lambda}_h, \boldsymbol{\lambda})$, given by Equation (34), are plotted for each fracture $i = 1, \ldots, 6$. For the displacement jump, the convergence is of first-order for all fractures except Fracture 4, which is correctly predicted to be sticking (and thus, the error is zero). For the Lagrange multiplier $\boldsymbol{\lambda}_h$, we observe first-order convergence for Fractures 4 and 5, while the error for Fracture 6 is zero. The convergence rates for traction is typically observed to be of first-order in the L_2 norm and second-order in the 2-norm for the finite-volume scheme [26, 37], but the Lagrange multiplier for fractures 1, 2 and 3 shows somewhat lower convergence rates than first-order. However, this is not surprising due to the low regularity of the Lagrange multipliers. Figure 6 shows first-order convergence of the error for the discrete displacement $\boldsymbol{u}_h$ in the 2d domain Ω. Finally, Table 2 shows that the number of Newton iterations do not grow significantly when the mesh is refined.

4.2 Example 2

In this example Ω is a 3d domain $(-200, 300) \times (-200, 300) \times (-300, 300)$ m with two circular fractures approximated by polygons with 10 vertices. The location and geometry of the fractures are given in Table 1. As in the previous example, no fluid is included. The bottom boundary is fixed, the four vertical boundaries are rolling, and at the top

Table 1: Fracture geometry in Example 2 and 3. The strike angle is the rotation from x-axis in the x-y-plane defining the strike line. The dip angle is rotation around the strike line.

	Fracture 1	Fracture 2
Center	$-[10, 30, 80]^\top$ m	$[15, 60, 80]^\top$ m
Radius	150 m	150 m
Strike angle	81.8°	78.3°
Dip angle	43.9°	47.1°

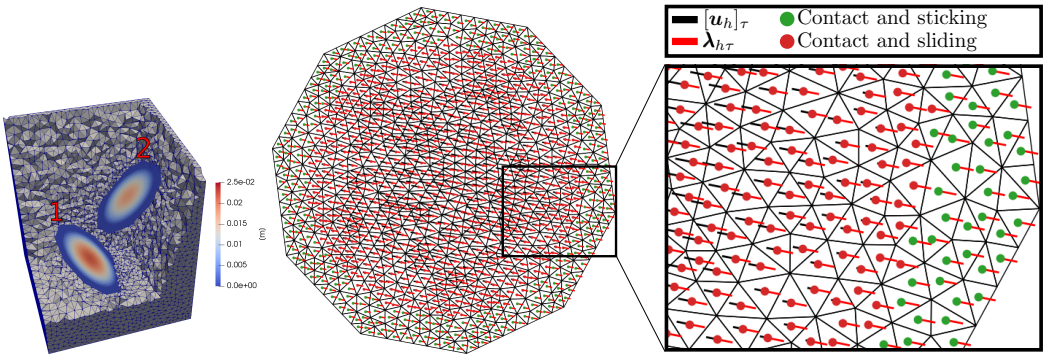

Figure 7: Results from Example 2 using approximately 250 thousand degrees of freedom. Left: Displacement jump $\|[\boldsymbol{u}_h]\|$ for the two fractures indicated by the fracture number. Parts of the 3d mesh are cropped to reveal the fractures. Middle: The surface mesh of Γ^+ of Fracture 1. The red lines show the tangential part of the Lagrange multiplier $\boldsymbol{\lambda}_{h\tau}$ while the black lines show the scaled displacement jumps $400[\boldsymbol{u}_h]_\tau$. Right: Zoomed view of middle figure.

boundary, a load is applied downwards by enforcing a Neumann condition $\boldsymbol{g}_{u,N} = [0, 0, -4.5]^\top$ MPa. The coefficient of friction is for the two fractures, $i = 1, 2$:

$$F_i(\boldsymbol{x}) = 0.5 \exp\left(\frac{10\text{m}}{R_i - D_i(\boldsymbol{x})} - \frac{10\text{m}}{R_i}\right),$$

where R_i is the radius of fracture i and $D_i(\boldsymbol{x})$ the distance from the center of the fracture to $\boldsymbol{x}$.

Figure 7 shows the displacement jump $[\boldsymbol{u}_h]_\tau$ and the shear component of the Lagrange multiplier $\boldsymbol{\lambda}_{h\tau}$. The fractures are in contact, i.e., the normal displacement jump $[\boldsymbol{u}_h]_n = 0$ is zero. Going from two dimensions to three adds an additional challenge to the contact problem as we have to find not only the magnitude of the slip but also the direction. The advantage of the hybrid formulation in combination with a semismooth Newton scheme is that the same computer code can be used for any dimension, and as observed in the figure, the correct sliding direction (parallel to the Lagrange multiplier) is found by the algorithm.

The errors are calculated by comparison to a reference solution that has 500 thousand degrees of freedom. The relative errors $\varepsilon_{\Gamma_i^+}([\boldsymbol{u}_h], [\boldsymbol{u}])$ and $\varepsilon_{\Gamma_i^+}(\boldsymbol{\lambda}_h, \boldsymbol{\lambda})$ for the two fractures, $i = 1, 2$, are shown in Figure 8. We observe first-order convergence for the displacement jump, while the Lagrange multiplier shows a somewhat reduced order of convergence. Finally, Table 2 shows the number of Newton iterations for each mesh, and we do not observe any significant increase in the number of Newton iterations as the mesh is refined.

4.3 Example 3

In this example, we consider the same domain and material parameters as in Example 1, but add a fluid. The permeability of the fluid is $\mathcal{K} = 10^{-8}$ m^{2}Pa^{-1}s^{-1}, the storage coefficient is $c_0 = 1 \cdot 10^{-10}$ Pa^{-1}, and the Biot

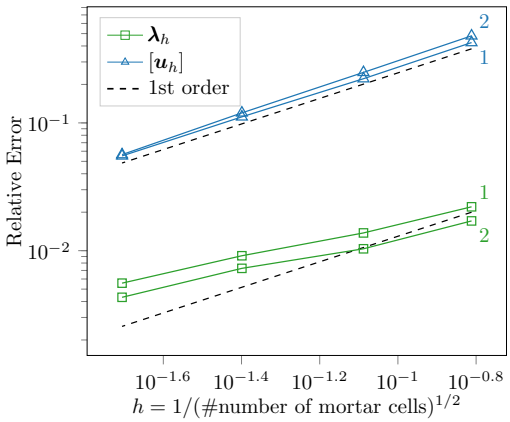

Figure 8: Convergence rates for the two fractures in Example 2. The error is measured as the relative errors, $\varepsilon_{\Gamma_i^+}([\boldsymbol{u}_h], [\boldsymbol{u}])$ and $\varepsilon_{\Gamma_i^+}(\boldsymbol{\lambda}_h, \boldsymbol{\lambda})$, for each fracture, Γ_i^+, as given in Equation 34. The numbering of the lines correspond to the fracture number.

Table 2: The number of Newton iterations used for the different mesh sizes in Example 1 and 2. The number of fracture faces and number of cells are given in the table.

Example 1			Example 2		
# fracture faces	# cells	# iterations	# fracture faces	# cells	# iterations
176	4538	5	126	449	3
346	17482	4	450	1878	3
682	68330	5	1884	11825	3
1356	270756	7	7728	160417	4

coefficient is $\alpha = 1$. The initial displacement and pressure is set to zero, and the end time of the simulation is set to $T = 5c_0H^2/\mathcal{K}$, where $H = 1$ m is the height of the domain. For the fluid, we enforce homogeneous Neumann conditions on all sides except the left boundary, where a zero pressure condition is given. For the mechanics, the left and the right boundaries are given a homogeneous Neumann condition, and the bottom boundary is given a zero Dirichlet condition. The top boundary is given a time varying boundary condition given by

$$\boldsymbol{g}_{u,D}(\boldsymbol{x}, t) = \begin{cases} [0.005 \text{ m}, -0.002 \text{ m}]^\top 2t/T, & t < T/2 \\ [0.005 \text{ m}, -0.002 \text{ m}]^\top, & t \geq T \end{cases} \quad \boldsymbol{x} \text{ on top boundary.}$$

This condition enforces a linear increase of the boundary condition values in the first half of the simulation, and after the boundary condition reaches the same value as in Example 1 we keep it constant for the remainder of the simulation.

In the first half of the simulation, the domain is compressed and the fluid pressure in the domain increases. In Figure 9, we plot the regions of the fractures that slip, stick and open for the two times $t = T/2$ and $t = T$. At the time $t = T/2$, the boundary condition for the mechanics is the same as in Example 1, however, we see considerable differences in the fracture displacement (compared to Figure 3) that are due to the introduction of the fluid. After $t = T/2$ the displacement boundary condition is fixed at $[0.005, -0.002]^\top$ m, and the fluid pressure decrease due to the zero pressure condition on the left boundary. This causes further deformation of the fractures, and at the end of the simulation the pressure in the whole domain is relatively close to zero, and the solution is approximately equal the solution in Example 1.

The number of Newton iterations for each time step is shown in Figure 10. For most iterations, the Newton solver converges in three iterations. The increase in the number of iterations needed at time $t/T = 0.65$ is believed

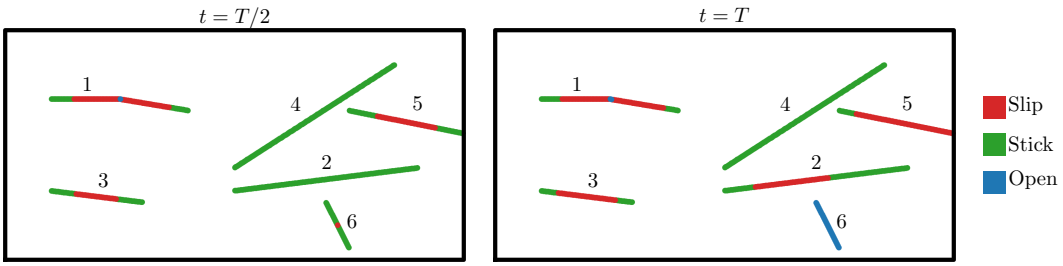

Figure 9: The fractured domain from Example 3. The black box corresponds to the domain boundaries, while the fractures, labeled by a number, are represented by lines. The fractures are colored in three colors; segments that slip are red, segments that stick are green, and segments that open are blue. The left figure shows the deformation half-way through the simulation, while the right figure, shows the deformation at the end time of the simulation.

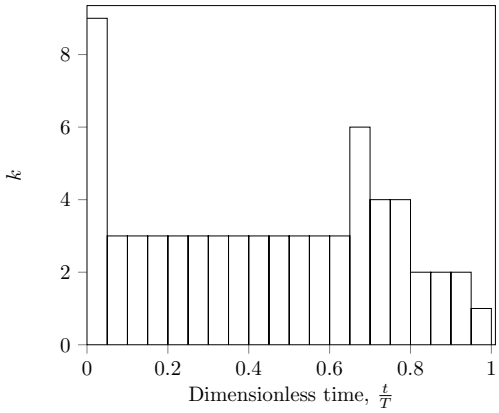

Figure 10: The number of Newton iterations at each time step for the simulation in Example 3.

to be related to Fracture 6 changing behavior from sliding to opening. At the end of the simulation the system is close to steady state, and the Newton solver converges in one iteration.

4.4 Example 4

In this example, the same setup as in Example 2 is used, but a fluid is included. The domain is sealed for the fluid, i.e., homogeneous Neumann conditions, for all sides except the top boundary, which is given a Dirichlet condition $g_{p,D} = 0$ Pa. The permeability is $\mathcal{K} = 10^{-8}$ m^{2}Pa^{-1}s^{-1}, the storage coefficient $c_0 = 1 \cdot 10^{-10}$ Pa^{-1}, and the Biot coefficient $\alpha = 1$. The initial displacement and pressure is set to zero.

Without the fractures, this setup is equivalent to a consolidation problem, which can be found in standard textbooks [24]. When the load is applied to the top surface at time $t = 0$, there is an instantaneous increase in the pore pressure in the domain. The fluid will then drain slowly out from the top surface and finally relax back to the initial condition. As this process occurs, the domain will continue to deform vertically increasing the mechanical load on the fractures, which causes them to slip. Twenty time steps are taken, and the simulation is stopped after 625 minutes, at which time, for practical purposes, equilibrium is reached.

The slip over time is plotted in Figure 11. Initially, the pore pressure carries most of the applied load, and the fractures are not sliding. As the fluid drains and the domain deforms, the tangential part of the Lagrange multiplier on the fractures increases, and after approximately 150 minutes, the fractures start to slide. The sliding

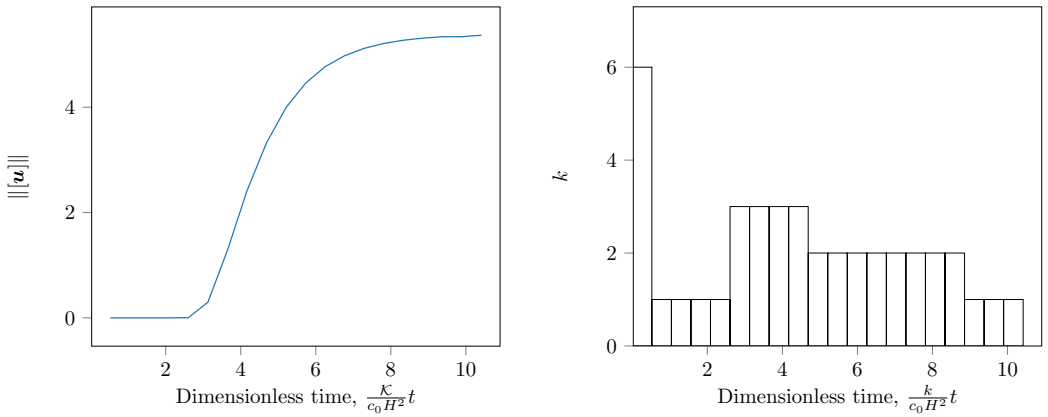

Figure 11: Results from Example 4. The length scale $H = 600$ m is the height of the domain. Left: Slip distance as a function of time. Right: Convergence of the Newton solver. Each time step is represented by a rectangle, and the y-axis shows the number of Newton iterations needed until the convergence tolerance is reached.

then gradually slows down and qualitatively reaches the solution of the drained medium, i.e., the solution from Example 2. There are small differences between the solution from this example at the final time and the solution of Example 2, which are caused by the use of a dynamic friction model in this example and a static friction model in Example 2.

The number of iterations needed for convergence of the Newton solver at each time step is shown in Figure 11. For the first time step, 6 Newton iterations are needed, which is twice as many as for any of the other time steps. It is well known that the Newton strategy is very sensitive to the initial guess. A naive choice generally results in an increase in the required number of Newton iterations for smaller mesh sizes. However, either in a dynamic or a multilevel context, there are good options to set the initial guess [22, 47]. In this case, the initial condition at $t = 0$ is ($\boldsymbol{\lambda} = \mathbf{0}$ and $\boldsymbol{u} = \mathbf{0}$), which assigns all subfaces to the noncontact set, $\mathcal{I}_n$, while those at the first time step belong to the sticking set $\mathcal{I}_\tau$ (see Equation (28)). During the dynamic sliding, the initial guess (the solution from the previous time step) gives a good approximation of the solution in the current time step, and thus, fewer iterations are needed. As the fractures start to slide at time step six, a few Newton iterations are needed for convergence. However, when approaching steady state, the algorithm predicts the correct slip in just one iteration.

5 Conclusion

In this paper, we present an approach for solving the poroelastic Biot equations in a fractured domain. A classical hybrid formulation for contact mechanics is combined with a finite volume discretization for poroelasticity. The fractures are modeled as internal contact boundaries and are governed by a nonpenetration condition in the normal direction and a Coulomb friction law in the tangential direction. The inequalities in the contact conditions are handled by a semismooth Newton method. The finite volume discretization has several advantages for these types of problems. The cell-center colocation of the discrete displacement and pressure variables gives a sparse linear system, efficient data structures, and no need for staggered grids. Moreover, the contact conditions are obtained naturally in the discretization as a condition per subface in the local systems. Thus, these conditions can be treated in an equivalent manner to boundary conditions on the external boundary. Finally, there is no need for special treatment of the contact conditions in the poroelastic case versus the purely elastic case, as the correct pressure contribution to the effective stress is obtained in the local system.

We showed that the hybrid formulation coupled with the finite volume discretization handles a given spatially varying coefficient of friction. The formulation is also suitable for other friction models such as rate and state friction or temperature-dependent coefficient of friction.

Four numerical examples illustrate the method's robustness and applicability to difficult cases. By comparison

to a reference solution, the discrete solution shows first-order convergence in displacements and slightly less than first-order convergence for the Lagrange multipliers. We also show that the method handles singularity in the solution resulting from a piecewise linear fracture with a kink. Finally, a 3d example is presented where we study the effect of the fluid pressure on the solution.

The model presented in this work is limited to fluid flow in the matrix. A natural extension is to include fluid flow also in the fractures. The fluid pressure in the fracture will then act as a force on the fracture sides, effectively reducing the normal traction. Experiments have also shown that asperities along fracture surfaces can have a very important effect on both the opening and sliding of fractures. These effects can be included by adding a nonlinear deformation model to the fractures. The advantage of our framework is that any nonlinear extensions to the model can be included in the same Newton iteration, which might be crucial for the convergence of the resulting scheme.

References

[1] I. Aavatsmark. "An Introduction to Multipoint Flux Approximations for Quadrilateral Grids". In: *Computational Geosciences* 6.3 (2002), pp. 405–432. DOI: 10.1023/A:1021291114475.

[2] G. Aguilar, F. Gaspar, F. Lisbona, and C. Rodrigo. "Numerical stabilization of Biot's consolidation model by a perturbation on the flow equation". In: *International Journal for Numerical Methods in Engineering* 75.11 (2008), pp. 1282–1300. DOI: 10.1002/nme.2295.

[3] U. Ayachit. *The ParaView Guide: A Parallel Visualization Application*. USA: Kitware, Inc., 2015.

[4] J. Bear. *Dynamics of Fluids in Porous Media*. Dover Civil and Mechanical Engineering Series. Dover, 1988.

[5] F. Ben Belgacem and Y. Renard. "Hybrid finite element methods for the Signorini problem". In: *Math. Comput.* 72 (2003), pp. 1117–1145.

[6] R. L. Berge, I. Berre, and E. Keilegavlen. "Reactivation of Fractures in Subsurface Reservoirs—A Numerical Approach Using a Static-Dynamic Friction Model". In: *Numerical Mathematics and Advanced Applications ENUMATH 2017*. Ed. by F. A. Radu, K. Kumar, I. Berre, J. M. Nordbotten, and I. S. Pop. Cham: Springer International Publishing, 2019, pp. 653–660.

[7] R. L. Berge and E. Keilegavlen. *Finite volume discretization for poroelastic media with fractures modeled by contact mechanics: Code*. Zenodo. 2019. DOI: 10.5281/zenodo.3371373.

[8] C. Bernardi, Y. Maday, and A. T. Patera. "A new nonconforming approach to domain decomposition: The mortar element method". In: *Nonlinear Partial Differential Equations and their Applications*. Ed. by H. Brezis and J.-L. Lions. Vol. XI of *Collège de France Seminar*. Pitman, 1994, pp. 13–51.

[9] M. A. Biot. "General Theory of Three-Dimensional Consolidation". In: *Journal of Applied Physics* 12.2 (1941), pp. 155–164. DOI: 10.1063/1.1712886.

[10] J. W. Both, M. Borregales, J.-M. Nordbotten, K. Kumar, and F. A. Radu. "Robust fixed stress splitting for Biot's equations in heterogeneous media". In: *Applied Mathematics Letters* 68 (2017), pp. 101–108. DOI: 10.1016/j.aml.2016.12.019.

[11] Z. Cai, J. Jones, S. McCormick, and T. Russell. "Control-volume mixed finite element methods". In: *Computational Geosciences* 1.3 (1997), pp. 289–315. DOI: 10.1023/A:1011577530905.

[12] O. Coussy. *Poromechanics*. Wiley, 2003.

[13] C. D´Angelo and A. Scotti. "A mixed finite element method for Darcy flow in fractured porous media with non-matching grids". In: *ESAIM: M2AN* 46.2 (2012), pp. 465–489. DOI: 10.1051/m2an/2011148.

[14] P. Dietrich, R. Helmig, M. Sauter, H. Hötzl, J. Köngeter, and G. Teutsch. *Flow and Transport in Fractured Porous Media*. Springer, Berlin, Heidelberg, 2005. DOI: 10.1007/b138453.

[15] R. Eymard, T. Gallouët, and R. Herbin. "Finite volume methods". In: *Solution of Equation in $\mathbb{R}^n$ (Part 3), Techniques of Scientific Computing (Part 3)*. Vol. 7. Handbook of Numerical Analysis. Elsevier, 2000, pp. 713–1018. DOI: 10.1016/S1570-8659(00)07005-8.

[16] H. Friis, M. Edwards, and J. Mykkeltveit. "Symmetric Positive Definite Flux-Continuous Full-Tensor Finite-Volume Schemes on Unstructured Cell-Centered Triangular Grids". In: *SIAM Journal on Scientific Computing* 31.2 (2009), pp. 1192–1220. DOI: 10.1137/070692182.

[17] T. T. Garipov, M. Karimi-Fard, and H. A. Tchelepi. "Discrete fracture model for coupled flow and geomechanics". In: *Computational Geosciences* 20.1 (2016), pp. 149–160. DOI: 10.1007/s10596-015-9554-z.

[18] F. J. Gaspar, F. J. Lisbona, and C. W. Oosterlee. "A stabilized difference scheme for deformable porous media and its numerical resolution by multigrid methods". In: *Computing and Visualization in Science* 11.2 (2008), pp. 67–76. DOI: 10.1007/s00791-007-0061-1.

[19] C. Geuzaine and J.-F. Remacle. "Gmsh: A 3-D finite element mesh generator with built-in pre- and post-processing facilities". In: *International Journal for Numerical Methods in Engineering* 79.11 (2009), pp. 1309–1331. DOI: 10.1002/nme.2579.

[20] B. Giovanardi, L. Formaggia, A. Scotti, and P. Zunino. "Unfitted FEM for Modelling the Interaction of Multiple Fractures in a Poroelastic Medium". In: *Geometrically Unfitted Finite Element Methods and Applications*. Ed. by S. P. A. Bordas, E. Burman, M. G. Larson, and M. A. Olshanskii. Cham: Springer International Publishing, 2017, pp. 331–352.

[21] J. B. Haga, H. Osnes, and H. P. Langtangen. "On the causes of pressure oscillations in low-permeable and low-compressible porous media". In: *International Journal for Numerical and Analytical Methods in Geomechanics* 36.12 (2012), pp. 1507–1522. DOI: 10.1002/nag.1062.

[22] S. Hüeber, G. Stadler, and B. Wohlmuth. "A Primal-Dual Active Set Algorithm for Three-Dimensional Contact Problems with Coulomb Friction". In: *SIAM Journal on Scientific Computing* 30.2 (2008), pp. 572–596. DOI: 10.1137/060671061.

[23] S. Hüeber. "Discretization techniques and efficient algorithms for contact problems". PhD thesis. Stuttgart: Universität Stuttgart, 2008.

[24] J. Jaeger, N. Cook, and R. Zimmerman. *Fundamentals of rock mechanics*. 4th ed. Wiley-Blackwell, 2007, pp. 189–194.

[25] E. Keilegavlen, A. Fumagalli, R. Berge, I. Stefansson, and I. Berre. "PorePy: An Open-Source Simulation Tool for Flow and Transport in Deformable Fractured Rocks". In: *arXiv* (2017). arXiv: 1712.00460.

[26] E. Keilegavlen and J. M. Nordbotten. "Finite volume methods for elasticity with weak symmetry". In: *International Journal for Numerical Methods in Engineering* 112.8 (2017), pp. 939–962. DOI: 10.1002/nme.5538.

[27] N. Kikuchi and J. Oden. *Contact problems in elasticity: A study of variational inequalities and finite element methods*. SIAM studies in applied mathematics 8, 1988.

[28] N. Kikuchi and Y. Joon Song. "Penalty/finite-element approximation of a class of unilateral problems in linear elasticity". In: *Quarterly of Applied Mathematics* 39 (1981). DOI: 10.1090/qam/613950.

[29] J. Kim, H. Tchelepi, and R. Juanes. "Stability and convergence of sequential methods for coupled flow and geomechanics: Fixed-stress and fixed-strain splits". In: *Computer Methods in Applied Mechanics and Engineering* 200.13 (2011), pp. 1591–1606. DOI: 10.1016/j.cma.2010.12.022.

[30] R. A. Klausen, F. A. Radu, and G. T. Eigestad. "Convergence of MPFA on triangulations and for Richards' equation". In: *International Journal for Numerical Methods in Fluids* 58.12 (2008), pp. 1327–1351. DOI: 10.1002/fld.1787.

[31] P. Lazzarin and R. Tovo. "A unified approach to the evaluation of linear elastic stress fields in the neighborhood of cracks and notches". In: *International Journal of Fracture* 78.1 (1996), pp. 3–19. DOI: 10.1007/BF00018497.

[32] V. Martin, J. Jaffré, and J. Roberts. "Modeling Fractures and Barriers as Interfaces for Flow in Porous Media". In: *SIAM Journal on Scientific Computing* 26.5 (2005), pp. 1667–1691. DOI: 10.1137/S1064827503429363.

[33] T. W. McDevitt and T. A. Laursen. "A mortar-finite element formulation for frictional contact problems". In: *International Journal for Numerical Methods in Engineering* 48.10 (2000), pp. 1525–1547. DOI: 10.1002/1097-0207(20000810)48:10<1525::AID-NME953>3.0.CO;2-Y.

[34] A. Mikelić, M. F. Wheeler, and T. Wick. "Phase-field modeling of a fluid-driven fracture in a poroelastic medium". In: *Computational Geosciences* 19.6 (2015), pp. 1171–1195. DOI: 10.1007/s10596-015-9532-5.

[35] A. Moinfar, K. Sepehrnoori, R. T. Johns, and A. Varavei. "Coupled Geomechanics and Flow Simulation for an Embedded Discrete Fracture Model". In: *SPE Reservoir Simulation Symposium* (2013). DOI: 10.2118/163666-MS.

[36] M. A. Murad and A. F. D. Loula. "On stability and convergence of finite element approximations of Biot's consolidation problem". In: *International Journal for Numerical Methods in Engineering* 37.4 (1994), pp. 645–667. DOI: 10.1002/nme.1620370407.

[37] J. Nordbotten. "Stable Cell-Centered Finite Volume Discretization for Biot Equations". In: *SIAM Journal on Numerical Analysis* 54.2 (2016), pp. 942–968. DOI: 10.1137/15M1014280.

[38] J. M. Nordbotten. "Cell-centered finite volume discretizations for deformable porous media". In: *International Journal for Numerical Methods in Engineering* 100.6 (2014), pp. 399–418. DOI: 10.1002/nme.4734.

[39] L. N. Olson and J. B. Schroder. *PyAMG: Algebraic Multigrid Solvers in Python v4.0*. Release 4.0. 2018. URL: https://github.com/pyamg/pyamg.

[40] M. A. Puso and T. A. Laursen. "A mortar segment-to-segment frictional contact method for large deformations". In: *Computer Methods in Applied Mechanics and Engineering* 193.45 (2004), pp. 4891–4913. DOI: 10.1016/j.cma.2004.06.001.

[41] P. A. Raviart and J. M. Thomas. "A mixed finite element method for 2-nd order elliptic problems". In: *Mathematical Aspects of Finite Element Methods*. Ed. by I. Galligani and E. Magenes. Berlin, Heidelberg: Springer Berlin Heidelberg, 1977, pp. 292–315.

[42] T. F. Russell. "Relationships among Some Conservative Discretization Methods". In: *Numerical Treatment of Multiphase Flows in Porous Media*. Ed. by Z. Chen, R. E. Ewing, and Z.-C. Shi. Berlin, Heidelberg: Springer Berlin Heidelberg, 2000, pp. 267–282.

[43] E. Ucar, I. Berre, and E. Keilegavlen. "Postinjection Normal Closure of Fractures as a Mechanism for Induced Seismicity". In: *Geophysical Research Letters* 44.19 (2017), pp. 9598–9606. DOI: 10.1002/2017GL074282.

[44] E. Ucar, I. Berre, and E. Keilegavlen. "Three-Dimensional Numerical Modeling of Shear Stimulation of Fractured Reservoirs". In: *Journal of Geophysical Research: Solid Earth* 123.5 (2018), pp. 3891–3908. DOI: 10.1029/2017JB015241.

[45] E. Ucar, E. Keilegavlen, I. Berre, and J. M. Nordbotten. "A finite-volume discretization for deformation of fractured media". In: *Computational Geosciences* 22.4 (2018), pp. 993–1007. DOI: 10.1007/s10596-018-9734-8.

[46] P. A. Vermeer and A. Verruijt. "An accuracy condition for consolidation by finite elements". In: *International Journal for Numerical and Analytical Methods in Geomechanics* 5.1 (1981), pp. 1–14. DOI: 10.1002/nag.1610050103.

[47] B. Wohlmuth. "Variationally consistent discretization schemes and numerical algorithms for contact problems". In: *Acta Numerica* 20 (2011), pp. 569–734. DOI: 10.1017/S0962492911000079.

[48] P. Wriggers. *Computational Contact Mechanics*. 2nd ed. Springer, Berlin, Heidelberg, 2006. DOI: 10.1007/978-3-540-32609-0.

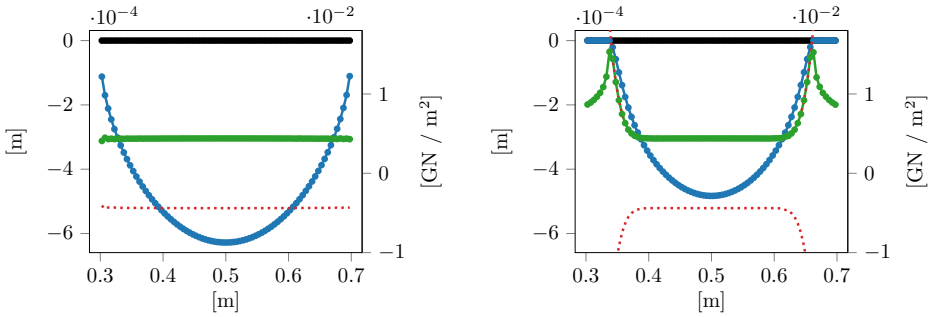

Figure 12: The shear component $\boldsymbol{\lambda}_\tau$ (green), friction bound $\pm F\lambda_n$ (red dashes), tangential displacement jump $[\boldsymbol{u}]_\tau$ (blue), and normal displacement jump $[\boldsymbol{u}]_n$ (black) for the fracture. The dots correspond to the face-centered values. Left: Constant friction coefficient. Right: Regularized coefficient.

Appendix A

When a fracture slides or opens, the linear elastic stress will contain a singularity at the fracture tips [31], which causes challenges for any numerical method. We illustrate this in Figure 12, where we plot the typical stress and displacement profiles for a sliding fracture and a constant friction coefficient $F = 0.5$. We observe small oscillations in the Lagrange multiplier around the tips of the fracture. The issue is that as we approach the fracture tips, an infinitesimal change in the displacement jump will induce an infinite change in the stress. These oscillations are reflected in the errors plotted in Figure 13, where the error rate for the Lagrange multiplier deteriorates. Convergence is not seen in the Lagrange multiplier. Because the face traction values away from the fracture tips are almost constant, the error in this region is very small, and thus, the error in the Lagrange multiplier is completely dominated by the oscillations near the tips. Note that the convergence rates for the displacement jump is of order 1, as expected. To study the convergence of the Lagrange multiplier, we can regularize the solution by increasing the friction bound smoothly in a small region around the tips. In this example, this is done by setting

$$F(\boldsymbol{x}) = 0.5(1 + 10\exp(-800\ \mathrm{m}^{-2} D(\boldsymbol{x})^2)) \qquad \boldsymbol{x} \in \Gamma^+,$$

where $D(\boldsymbol{x})$ is the distance from $\boldsymbol{x}$ to the tips of the fracture. As seen in Figure 12, this arrests the fracture before the tip, and the added regularity gives first-order convergence in both the Lagrange multiplier and displacements, as shown in Figure 13.

The worst oscillations that we have encountered in 3d using our finite volume scheme coupled with the hybrid formulation are shown in Figure 14. The setup in this example is the same as the setup in Section 4.2 but with only Fracture 1 and a constant coefficient of friction, $F = 0.5$. Thus, we have sliding reaching the tip of the fractures. The oscillations have an amplitude of approximately 5 percent from the mean traction and grow larger as we approach the fracture tips. As in the 2d case, the displacement jump $[\boldsymbol{u}_h]$ is not effected significantly by these oscillations.

Note that the singularity at the fracture tips is a challenge for any numerical method. Similar oscillations for first- and second-order Galerkin finite elements are reported, for example, by Garipov et al [17]· Fig. 8, for a setup where they study a single sliding fracture.

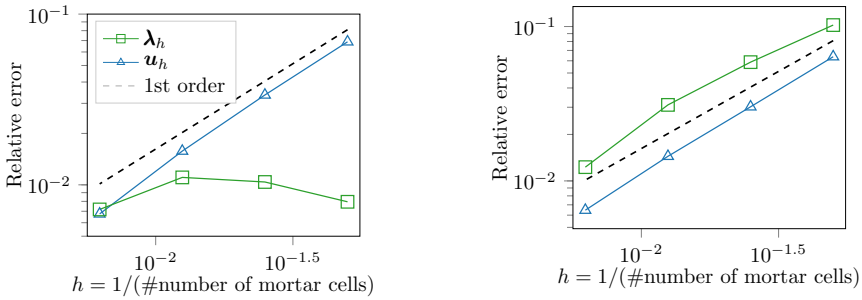

Figure 13: Convergence rates for the jump $[\boldsymbol{u}_h]$ and Lagrange multiplier $\boldsymbol{\lambda}_h$ on Γ^+. The y-axis shows the relative error $\|\boldsymbol{v}_h - \boldsymbol{v}\|_{\Gamma^+} / \|\boldsymbol{v}\|_{\Gamma^+}$, $\boldsymbol{v} \in \{[\boldsymbol{u}], \boldsymbol{\lambda}\}$. Left: The convergence of the unregularized solution. Right: The convergence of the regularized solution.

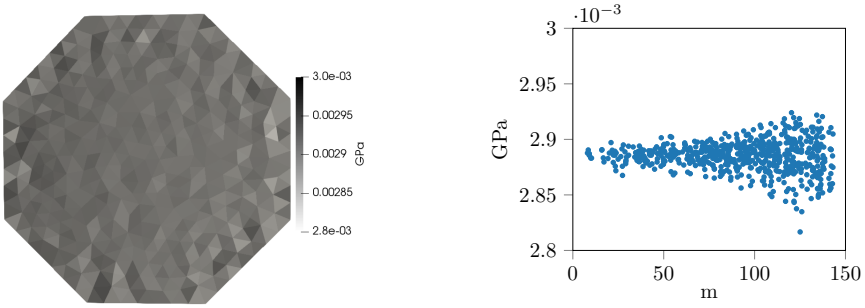

Figure 14: Oscillations in the normal component of the Lagrange multiplier. Left: The negative normal component of the Lagrange multiplier $-\boldsymbol{\lambda}$ on the fracture. Right: The negative normal component of the Lagrange multiplier $-\boldsymbol{\lambda}$, where the x-axis is the radial distance from the fracture center, i.e., the center is at $x = 0$, while the tip is at $x \approx 150$ m..

Paper D

PorePy: An Open-Source Software for Simulation of Multiphysics Processes in Fractured Porous Media

Eirik Keilegavlen, Runar L. Berge, Alessio Fumagalli, Michele Starnoni, Ivar Stefansson, Jhabriel Varela, Inga Berre

D

Submitted to Computational Geosciences
arXiv:1908.09869 [math.NA]

PorePy: An Open-Source Software for Simulation of Multiphysics Processes in Fractured Porous Media

Eirik Keilegavlen[1], Runar Berge[1], Alessio Fumagalli[1], Michele Starnoni[1], Ivar Stefansson[1], Jhabriel Varela[1], Inga Berre[1]
[1]Department of Mathematics, University of Bergen.

Corresponding author: Eirik.Keilegavlen@uib.no, Department of Mathematics, University of Bergen, Pb 7800, 5020 Bergen, Norway.

Abstract

Development of models and dedicated numerical methods for dynamics in fractured rocks is an active research field, with research moving towards increasingly advanced process couplings and complex fracture networks. The inclusion of coupled processes in simulation models is challenged by the high aspect ratio of the fractures, the complex geometry of fracture networks and the crucial impact of processes that completely change characteristics on the fracture-rock interface. This paper provides a general discussion of design principles for introducing fractures in simulators, and defines a framework for integrated modeling, discretization and computer implementation. The framework is implemented in the open-source simulation software PorePy, which can serve as a flexible prototyping tool or multiphysics problems in fractured rocks. Based on a representation of the fractures and their intersections as lower-dimensional objects, we discuss data structures for mixed-dimensional meshes, formulation of multiphysics problems and discretizations that utilize existing software. We further present the implementation of these concepts in the PorePy open-source software tool, which is aimed at coupled simulation of flow and transport in three-dimensional fractured reservoirs as well as deformation of fractures and the reservoir in general. We present validation by benchmarks for flow, poroelasticity and fracture deformation in fractured porous media. The flexibility of the framework is then illustrated by simulations of non-linearly coupled flow and transport and of injection driven deformation of fractures. All results reported herein can be reproduced by openly available simulation scripts.

Keywords: Fractured reservoirs; mixed-dimensional geometry; numerical simulations; multiphysics; discrete fracture matrix models; open-source software; reproducible science.

1. Introduction

Simulation of flow, transport and deformation of fractured rocks is of critical importance to several applications such as subsurface energy extraction and storage and waste disposal. While the topics have received considerable attention the last decade, the development of reliable simulation tools remains a formidable challenge. Many reasons can be given for this, we here pinpoint four possible causes: First, while natural fractures are thin compared to the characteristic length of the domains of interest, their extent can span through the domain of interest [1]. The high aspect ratios make the geometric

representation of fractures in the simulation model challenging. Second, the strongly heterogeneous properties of fractures compared to the matrix with respect to flow and mechanics call for methods that can handle strong parameter discontinuities as well as different governing physics for the fractures and the matrix, *e.g.* [2]–[4]. Third, phenomena of practical interest tend to involve multiphysics couplings, such as interaction between flow, temperature evolution, geo-chemical effects and fracture deformation [5]. Correspondingly, there is an ongoing effort to develop and introduce multiphysics couplings within simulation models [6]. Fourth, fracture networks have highly complex intersection geometries, which must be accounted for in the simulation models. We emphasize that, although the geometry of the walls of individual fractures can be complex by themselves, we will not consider this in any detail, but rather assume that averaged apertures etc. are available at the scale of discretizations.

Traditionally, simulation of flow-driven dynamics in fractured media has been based on two conceptual models: First, in an upscaled representation, the fracture network geometry and dynamical processes taking place in the network are replaced by equivalent continuum models, which resemble those used in non-fractured porous media. As these models do not resolve the fracture geometry, they are computationally efficient, and have been extended to cover a wide range of multiphysics couplings, as exemplified by the TOUGH2 family of codes [7], PFLOTRAN [8], and also *e.g*. [9]. The accuracy of the simulation is however highly dependent on the quality of the upscaled model, which in turn depends on the fractured domain's resemblance of a continuous medium with respect to the nature of the physical processes. In practice, the upscaling process ranges from treatable by analytical means for simple fracture geometries and dynamics [10], [11], to extremely challenging in the case of multiphysics couplings and complex fracture geometries [12], [13] .

The second traditional class of models, known as the discrete fracture network (DFN) models, is constructed using an explicit representation of the fracture network in the simulation model, while ignoring the surrounding rock mass. The models combine highly accurate representation of dynamics in the fractures with computational efficiency from not having to deal with the rock matrix, which is highly desirable *e.g*. for fast model evaluation. DFN simulation models with a high level of sophistication have been developed, notably for coupled flow and transport, see for instance [14]–[16]. By themselves, DFN models cannot represent processes outside the fracture network; however, the models can be combined with continuum models to achieve fracture-matrix couplings.

The respective limitations of upscaled and DFN approaches have over the last decade led to an increased interest in the class of discrete fracture matrix (DFM) models. In DFM models, the fractures are sorted in two classes according to their importance for the dynamics in question [17]. The most important fractures are represented explicitly, while upscaled models are applied for the remaining fractures and the host rock. As such, DFM models represent a flexible compromise between upscaling and explicit representations. The models can represent governing equations in the rock matrix, fractures, and generally also in the intersections between fractures. For computational efficiency, it is common to represent fractures and their intersections as lower-dimensional objects embedded in the three-dimensional rock matrix [18], [19]. We refer to this as a mixed-dimensional model [20], and conversely refer to a model of a domain where only a single dimension is considered as fixed-dimensional.

DFM models can further be divided into two subgroups, according to whether they explicitly represent the fracture surfaces in the computational grid [17]. Models that apply non-conforming meshing include

the Embedded Discrete Fracture Matrix model (EDFM) [21], and extended finite element methods (XFEM) [22], [23]. These methods avoid the complexities of conforming mesh generation discussed below, but must instead incorporate the fracture-matrix interaction in what becomes complex modifications of the numerical method for XFEM [24], or by constructing upscaled representation reminiscent of the challenge in continuum-type models [25]. For this reason, our interest herein is DFM methods with conforming meshes. By now, this type of DFM models have been developed for flow and transport, as well as mechanics and poroelasticity. Simulation models that incorporate DFM principles include DuMuX [26], CSMP [27], MOOSE-FALCON [28], [29], OpenGeoSys [30] and Flow123d [31].

The utility of a rapid prototyping framework is illustrated by the wide usage of the Matlab Reservoir Simulation Toolbox (MRST) [32], [33], mainly for non-fractured porous media. Similarly, research into strongly coupled processes in mixed-dimensional geometries will benefit from software of similar flexibility and with a structure tailored to the specific challenges related to fractured porous media.

The goal of this paper is two-fold: First, we review challenges related to design of simulation frameworks for multiphysics couplings in mixed-dimensional geometries. Our aim is to discuss design choices that must be made in the implementation of any DFM simulator, including data structures for mixed-dimensional geometries, and representation and discretization of multiphysics problems. Second, we describe a framework for integrated modeling, discretization and implementation, and an open-source software termed PorePy adhering to this framework. Key to our approach is a decomposition of the geometry into separate objects for rock matrix, individual fractures and fracture intersections. Governing equations can then be defined separately on each geometric object, as well as on the connection between the objects. This allows for significant code reuse from the discretization of fixed-dimensional problems; thus, our design principles are also applicable to more general PDE software frameworks, such as FEniCS [34], Dune [35] and FireDrake [36]. Furthermore, for scalar and vector elliptic problems (flow and deformation) the models rest on a solid mathematical formulation [37]–[39].

Built on the object-based mixed-dimensional geometry, PorePy offers several discretization schemes for mathematical models of common processes, such as flow, transport and mechanical deformation. Multiphysics couplings are easily formulated, and their discretization depends on the availability of appropriate discretization schemes. Moreover, the framework allows for different geometric objects to have different primary variables and governing equations. The software can be used for linear and non-linear problems, with the latter treated by automatic differentiation. For DFM models that explicitly represent the fractures in the computational grid, meshing is a major technical challenge, in particular for 3d problems. PorePy offers automatic meshing of fractured domains in 2d and 3d, relying on the third-party software Gmsh to construct the mesh [40]. The software is fully open-source (see www.github.com/pmgbergen/porepy) and is released under the GNU General Public License (GPL).

The paper is structured as follows: In Section 2, we present the principles whereupon we have built the mixed-dimensional framework in PorePy. Section 3 deals with modeling and discretization of physical processes central to fractured porous media: single-phase flow, heat transport, poroelastic rock deformation, and fracture deformation modeled by contact mechanics. In Section 4, we benchmark our approach and the library PorePy by well-established test cases. In Section 5, we present two complex examples to illustrate the potential of the framework with respect to advanced physical processes, followed by conclusions in Section 6.

2 Design principles for mixed-dimensional simulation tools

A simulation model for a specific dynamical process in mixed-dimensional media requires three main ingredients: A representation of the mixed-dimensional geometry, governing equations for dynamics within and between the geometric objects (rock matrix, fractures, their intersections), and a strategy for discretization and assembly of the equations on the geometry. On the more fundamental level of simulator design, important questions to clarify include how much of the mixed-dimensional geometry to include, which type of couplings between different geometric objects to permit, and how to establish communication between the geometric objects.

In this section, we discuss principles for process couplings in a general context of fractured rocks, together with representation of the geometry in a continuous and discrete setting. As we will see, the design choices cannot be done independently, for instance the coupling structure puts constraints on the representation and data structure for the geometry. We further present the specific models underlying PorePy, including mesh generation, construction of projection operators between geometric entities, and discretization and assembly on mixed-dimensional geometries. The general discussion herein is supplemented by concrete examples of modeling and discretization of important governing processes presented in Section 3.

2.1 Representation of a mixed-dimensional geometry

We consider the geometry of a fracture network embedded in a 3d domain; 2d domains are treated by the natural simplification. In general, the geometry formed by the fracture network consists of objects of dimension 2 (the fractures), 1 (fracture intersections) and 0 (intersections of intersection lines), in addition to the 3d domain itself. An important decision for the modeling of dynamics in the domain is which parts of the geometry to represent in the model. We emphasize that as our focus herein is DFM models, it is assumed that at least the fractures in question will be explicitly represented in the simulation model, and furthermore that the simulation grid will conform to the fractures.

We differ between two approaches to representation of the fracture geometry: The first explicitly represents the full hierarchy of geometric objects (3d-0d) as described above. However, for many processes, one can to a good approximation assume that the main dynamics take place in the matrix or in the fractures, while objects of co-dimension more than 1 (intersection lines and points) mainly act as transition zones between fractures. This observation motivates the second approach: The matrix and fractures are represented explicitly, together with some model for direct fracture-fracture interaction.

Representation only of matrix and fractures and not the intersections in some sense constitutes the minimal modification to an existing fixed-dimensional model and has been a popular choice *e.g.* for flow and transport problems [41]. The strategy has also been taken a long way towards practical applications, see for instance [42]. There are however drawbacks, notably in the treatment of fracture intersections: Without explicit access to the intersection objects, modeling of interaction between two fractures can be challenging. Significantly, the difficulties tend to increase with increasing complexity of the dynamics, such as countercurrent flow due to gravity and capillary forces, and when transitioning from 2d domains to 3d (i.e. the dimension of the intersections increases from zero to one). This has important consequences for model and method development, as issues related to *ad hoc* treatment of intersection dynamics may not manifest until relatively late in the development process.

Our preferred solution is to apply an equal representation of all geometric objects, independent of their dimension. This allows for flexible modeling of dynamics within all objects, and as we will see below, the implementation of couplings between geometric objects can be made independent of the objects' dimensions. The design choice has further advantages in terms of reuse of discretizations, as will be discussed in Section 3. In this framework, variables follow the domain decomposition approach and are associated with single subdomains or interfaces. This is followed through in our implementation, where the solution vectors in different subdomains are represented by different objects, even if they represent parts of the same physical quantity, for instance pressure or temperature.

Our approach to the geometry representation is illustrated in Figure 1, which shows the decomposition of a mixed-dimensional geometry into a hierarchy of geometric objects with accompanying meshes.

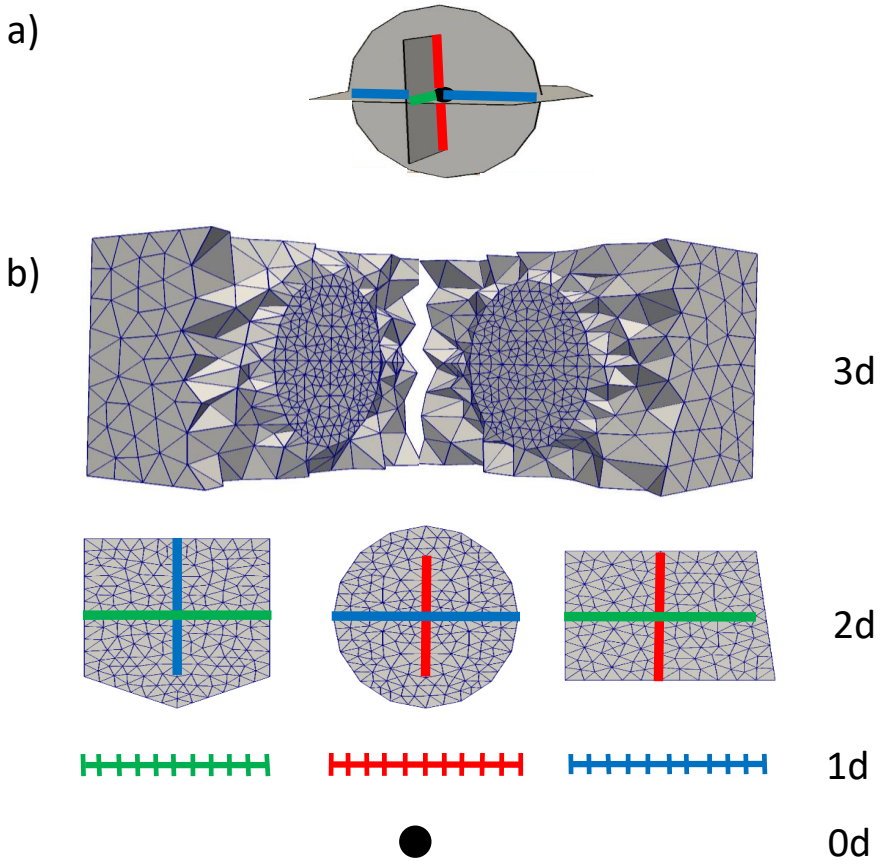

Figure 1: Conceptual illustration of a fracture network, including meshing and lower-dimensional representation. a) Fracture network, the rock matrix is not visualized. b) Meshes of all subdomains. Fracture intersections (1d) are represented by colored lines, the 0d grid by a black circle. The 3d mesh is cut to expose the circular fracture.

2.2 Permissible coupling structures between geometric objects

For modeling purposes, and for the choice of data structures discussed next, it is important to establish which types of couplings between subdomains are permitted. In our framework we impose the following constraints on the modeling:

1. Only coupling between subdomains that are exactly one dimension apart is allowed.
2. Interaction between subdomains should be formulated as models associated with the interface between the subdomains. This requires interface variables that represent the interaction between the subdomains.
3. An interface law can depend on variables on the interface and the immediate subdomain neighbors, but not on variables associated with other subdomains or interfaces.

These choices have several important consequences: First, our framework explicitly rules out direct 3d-1d couplings. Although some of the ingredients presented herein could be of interest for such high dimensional gaps, notably a modified version of the mixed-dimensional grid structure presented below, the mathematical structure of the two problems is significantly different, and we have therefore not pursued a unified treatment. Second, our model does not permit direct coupling between objects of the same dimension, say, two fractures; the communication must go via a lower- or higher-dimensional object. Third, the restriction that couplings should be formulated in terms of interface variables makes the structure of the equations on a subdomain relatively simple, as the dynamics depends only on variables internal to the subdomain and on neighboring interfaces.

2.3 Data structure for geometry and data

The restrictions put on the coupling structure between subdomains give important guidance on the definition of a data structure for the compound mixed-dimensional grid, consisting of all subdomains and interfaces. As subdomains should only see neighboring interfaces, and the interfaces only communicate with their two neighboring subdomains, the grid can be represented in the simulation model as a graph, with the subdomains forming nodes, while interfaces are edges.

The graph is now the natural place to store all kind of data relating to the simulation including grids, parameters and variables, as well as information on which equations to solve in each subdomain, and which discretization schemes to apply. The data structure is thus a natural framework for defining advanced simulation models, examples will be shown in Sections 4 and 5. While this flexibility can be gained by applying domain decomposition to any problem [43], for fractured domains it comes as an added feature from what is already a natural data structure for the geometry.

2.4 Meshing and projections

Having defined the data structure for the mixed-dimensional geometry, we proceed to discussing meshing of the geometric objects and establishing projection operators for communication between the objects.

2.4.1 Mesh construction in mixed-dimensional geometries

A major technical difficulty of conforming DFM models is the construction of meshes. Obtaining meshes that conform to all geometric objects requires first, identification of all intersection lines and points, then meshing of objects of all dimensions, and finally identification of neighboring cells and faces on different domains, so that inter-object interaction can be modeled. In principle, the computation of

fracture intersections is straightforward, following for instance [44]. In practice, this requires (automatic) decisions on when two objects should be considered distinct in the computational mesh; for complex networks this can be rather challenging. Notably, the question of whether objects should be considered spatially separated must be seen in connection with the prescribed mesh size, which puts practical constraints on how fine details can be resolved.

From a geometric description with all intersections identified, meshes of all objects can be constructed; in PorePy this is handled by a backport to Gmsh [40]. As post processing of the Gmsh output, standard simulation meshes are generated for all subdomains: The mesh for the 3d subdomain consists of all 3d cells, while for each fracture a mesh is composed of all faces of the 3d grid that lie on the surface of the fracture. Similarly, meshes for 1d intersection lines are formed by edges of the 3d grid that coincide with the line, while point meshes for 0d intersections are identified by nodes in the 3d grid. For 2d domains with 1d fractures and 0d intersections, the construction is similar. We emphasize that each of the meshes is implemented as a standard fixed-dimensional mesh, so that when a discretization scheme is applied to a subdomain, this is indistinguishable from the traditional fixed-dimensional operation. In this spirit, the grid structure used for individual meshes is agnostic to spatial dimension, with an implementation heavily inspired by that of MRST [33]. This grid structure in many cases facilitates an implementation of discretization schemes which is independent of dimension.

The meshes generated by Gmsh match between the subdomains. Moreover, the PorePy interface to Gmsh is restricted to simplex cells as these are most relevant for complex geometries. Non-matching grids can be introduced to PorePy by replacing meshes on individual subdomains; examples of computations on non-matching grids are given in Sections 4.1 and 5.1.

We finally note that tuning of mesh sizes in parts of the domain so that the resulting grid both resolves the local geometry and provides the desired accuracy for numerical computations can be a delicate task. Within PorePy, we attempt to handle this by setting a minimal mesh size and target mesh sizes for the fractures and the global boundary (far-field conditions). Based on these three user-provided entries, mesh size parameters are computed for all points in the fracture geometry and provided as guidance to Gmsh. In practice, Gmsh may override the settings, but nevertheless, the mesh size tuning combined with the automatic processing of the fracture geometry is a major capability of PorePy.

2.4.2 Mortar grids and projection operators

In addition to meshing on the subdomains, the interfaces are assigned separate meshes. These are used for discretization of the interface variables and serve as mortar grids for the coupling between the subdomains. Specifically, as the mortar grids allow for non-matching grids between subdomains, computational speedups can be achieved by combining fine grids in fractures, which are often the main venue for dynamical processes, with relatively coarse grids in the matrix. When using mortar technology to combine non-matching grids, non-uniform discretizations or physics, it is important to carefully design the mortar space so that the coupling does not introduce instabilities, see *e.g.* [45].

Transfer of variables between an interface and its neighboring subdomain is handled by projection operators. In the subsequent parts we will apply four different classes of projections. We have the mapping from an interface to the related subdomains indicated with Ξ, with a subscript indicating the index of the interface and a superscript the index of the subdomain, see Figure 2 for an illustration. We also introduce the projection operators from neighboring subdomains of an interface to the interface

itself, denoted by the symbol Π with the same convention as before for sub- and superscripts. The actual definition of these objects is scope dependent and it will be specified when needed. In our implementation, we have only considered projections of lowest order which can be constructed by identifying overlapping areas between cells in the interface grid and faces and cells in the neighboring meshes. The actual construction of the projection needs to consider the nature of the variable to project, being of intensive or extensive kind.

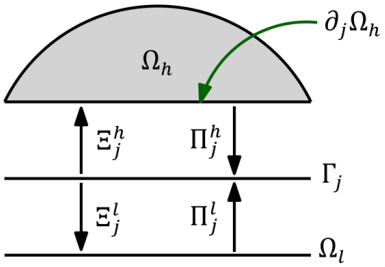

Figure 2: Generic geometry of a coupling between subdomains: An interface Γ_j is coupled to a higher-dimensional subdomain Ω_h and a lower-dimensional subdomain Ω_l. The projection operators between interfaces and subdomains are denoted by Π (interface to subdomain) and Ξ (subdomain to interface) with subscripts indicating the interface and superscript indicating the subdomain. In practice, Γ_j will coincide with an internal boundary of Ω_h, which we will refer to as $\partial_j\Omega_h$.

2.5 Governing equations and discretization

With the above framework, the task of defining governing equations and their discretization is split into two operations that to a large degree are independent, although this naturally depends on the physical process to be modeled. First, on the subdomains, the governing equations can often be defined (and to a large degree discretized) as if the problem were fixed-dimensional, while interaction with the interface variables takes the form of boundary conditions and source terms or body forces. These are terms that can be handled by any standard numerical method, and so the coupling structure paves the way for considerable reuse of existing simulation code designed for fixed-dimensional problems. The second operation involves coupling conditions on the interface, including projections of variables on the neighboring subdomains. This operation generally has no clear parallels for fixed-dimensional problems.

The details of the discretization can vary substantially depending on the governing equations and designated discretization schemes. We will give several examples of this in Section 3.

2.6 Global assembly

A global system of equations can be assembled from the components on individual subdomains and interfaces. The form and proper treatment of these equations differ according to whether the problem is stationary or time-dependent, linear or non-linear, but some ingredients of the implementation and structure of the problem are common. Specifically, for multiphysics problems with more than one primary variable, the global system of equations has a double block structure: One set of blocks stems from the geometric division into subdomains and interfaces. Within each subdomain and interface, there is a second set of blocks, with one block per variable. Access to this information is useful for design of tailored preconditioners and linear solvers, as well as post processing and visualization. PorePy has

implemented a global degree-of-freedom manager, that keeps track of the block structure of the system of equations, as well as the numbering of individual degrees of freedom.

For visualization, an export filter to Paraview [46] is available. To aid analysis of simulation results, the export preserves the link between the data and its associated dimensions.

3 Modeling, discretization and implementation

In this section we apply the general framework presented above to three sets of governing equations, each of which is of high relevance for fractured porous media: The elliptic pressure equation, fully coupled flow and transport, and inelastic deformation of fractures due to poroelastic effects. As most of these processes are well established for fixed-dimensional, partly also for mixed-dimensional, problems, our main purpose is to cast the methodology in the general framework of Section 2, with discussions of modeling, extension of numerical methods designed for fixed-dimensional problems, and implementation aspects. The presentation of the three model problems will emphasize these ingredients in varying degrees, with the aim that the section in total should illustrate the full power of the modeling framework.

The notation used for variables and subdomains is fixed as follows: Let Ω_i denote a generic subdomain, with variables in Ω_i marked by subscript i. A generic interface between two subdomains is represented by Γ_j, with subscript j identifying interface variables. For a subdomain Ω_i, the set of neighboring interfaces is split into interfaces towards subdomains of higher dimensions, denoted $\hat{S}_i$, and interfaces towards subdomains of lower dimensions, represented by $\check{S}_i$, see Figure 3. When discussing subdomain couplings for an interface Γ_j, we let the higher- and lower-dimensional subdomain be represented by Ω_h and Ω_l, respectively, and associate variable subscripts h and l, see Figure 2. Finally, the part of the boundary of Ω_h that coincides with Γ_j is denoted $\partial_j \Omega_h$.

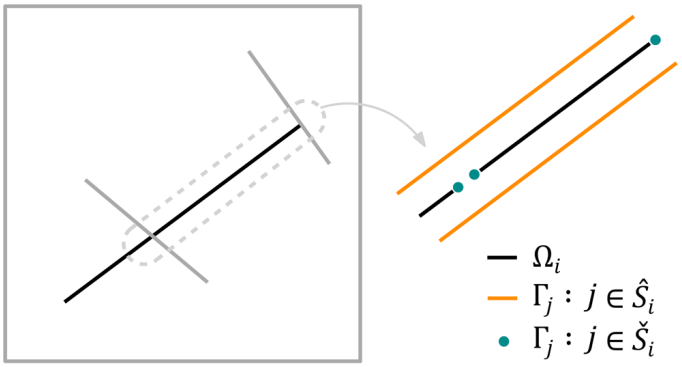

Figure3: Illustration of the interfaces neighboring a 1d fracture subdomain Ω_i. Interfaces towards higher-dimensional neighbors are represented by the index set $\hat{S}_i$, while the corresponding index set for lower-dimensional neighbors is denoted $\check{S}_i$.

3.1 Flow in fractured media

We first consider flow in mixed-dimensional geometries, where we assume a Darcy-type relation between flux and pressure gradients in all subdomains. The model has been presented several times before, see *e.g.* [2], [47]; our presentation therefore emphasizes implementational aspects within the framework presented in the previous sections. Moreover, of the model problems considered in this

work, the flow problem by far has the best developed mathematical theory, and we therefore use this section to illustrate both variational and integral approaches to mixed-dimensional modeling and simulation.

3.1.1 Governing equations

To introduce the model, we first consider a domain with a single interface Γ_j, with neighboring subdomains Ω_h and Ω_l, such that Ω_h is of one dimension higher than Γ_j (which thus acts as an internal boundary) and Ω_l geometrically coincides with Γ_j as illustrated in Figure 2. The flow model presented below has been studied *e.g.* in [39], [47]. We denote the flux on Γ_j by λ_j, we can formally write $\lambda_j = \Pi_j^h tr\, q_h \cdot n_h$, with n_h the unit normal of $\partial_j\Omega_h$ pointing from Ω_h to Ω_l and tr a suitable trace operator from Ω_h to $\partial_j\Omega_h$. First consider the strong form of the Darcy problem stated for Ω_l, which reads: find (q_l, p_l) such that

$$\begin{aligned} q_l + \frac{\mathcal{K}_l}{\mu_l}\nabla p_l &= 0, \\ \nabla \cdot q_l - \Xi_j^l \lambda_j &= f_l, \end{aligned} \tag{3.1}$$

where the differential operators are defined on the tangent space of Ω_l and Ξ_j^l maps from Γ_j to Ω_l. We have indicated with f_l a scalar source or sink term, μ_l is the fluid viscosity, while $\mathcal{K}_l$ represents the effective tangential permeability tensor, scaled by aperture, for more information see [48]. An analogous problem is written also for (q_h, p_h), with the exception that $\Xi_j^h \lambda_j$ is mapped to a boundary condition on $\partial_j\Omega_h$,

$$q_h \cdot n_h|_{\partial_j\Omega_h} = \Xi_j^h \lambda_j. \tag{3.2}$$

The flux λ_j is given by an interface condition of Robin-type on Γ_j for Ω_h, which reads

$$\lambda_j + \frac{\kappa_j}{\mu_j}\left(\Pi_j^l p_l - \Pi_j^h tr\, p_h\right) = 0, \tag{3.3}$$

where κ_j indicates the normal effective permeability, and Π_j^l and Π_j^h the normal projection operators to Γ_j from Ω_l and $\partial_j\Omega_h$, respectively. Equation (3.3) can be seen as a Darcy law in the normal direction associated to Γ_j. Several boundary conditions can be imposed on the external boundary of Ω_h and Ω_l, for simplicity we limit ourselves to homogeneous pressure conditions in the following. If Ω_l has a portion of the boundary which does not touch the external boundary, the so-called tip condition will be imposed being null flux. For notational convenience, we consider a unit viscosity for the remainder of this section; the viscosity is reintroduced in Section 3.2.

The extension to problems with many subdomains is now immediate: The interface still relates to its two neighboring subdomains, while for a subdomain Ω_i summation over all neighboring interfaces gives the problem: Find (q_i, p_i) so that

$$\begin{aligned} q_i + \mathcal{K}_i \nabla p_i &= 0, \\ \nabla \cdot q_i - \sum\nolimits_{j \in \hat{S}} \Xi_j^i \lambda_j &= f_i, \end{aligned}$$

$$q_i \cdot n_i|_{\partial_j \Omega_i} = \Xi_j^i \lambda_j \quad \forall j \in \check{S}_i.$$

(3.4)

In the case of $d = 0$, most of the above terms are void, and we are left only with the balance between the source term and fluxes from higher dimensions.

3.1.2 Subdomain variational and integral formulation

To move towards the numerical implementation, we introduce variational and integral formulations of the problem (3.4). Again, we focus on a domain with two subdomains and a single interface; the extension to several subdomains is straightforward.

Let the mortar variable be represented by $\lambda_j \in W(\Gamma_j) = L^2(\Gamma_j)$, in this setting we can define more precisely the projections $\Xi_j^l : L^2(\Gamma_j) \to L^2(\Omega_l)$ and $\Xi_j^h : L^2(\Gamma_j) \to L^2(\partial_j \Omega_h)$ that map interface fluxes to the neighboring subdomains. We note that the fluxes are mapped to the boundary of Ω_h but to the interior of Ω_l, hence λ_j acts as a boundary condition and a source term for the higher- and lower-dimensional subdomain, respectively. We also particularize projections from subdomains to the interface, defined as $\Pi_j^l : L^2(\Omega_l) \to L^2(\Gamma_j)$ and $\Pi_j^h : L^2(\partial_j \Omega_h) \to L^2(\Gamma_j)$; we shall comment on the implied L^2 regularity on $\partial_j \Omega_h$ below.

We first develop a mixed variational formulation of (3.4), introducing the following functional spaces

$$V(\Omega_h) = \{v \in H_{\nabla\cdot}(\Omega_h) : tr\, v \cdot n_h \in L^2(\partial_j \Omega_h)\}, \quad V(\Omega_l) = H_{\nabla\cdot}(\Omega_l) \quad \text{and} \quad Q(\Omega_l) = L^2(\Omega_l).$$

Moreover, let the space $\mathrm{Q}(\Omega_h)$ be a subspace of $L^2(\Omega_h)$ such that it is possible to define the operator $tr\, p_h$ with range at least in $L^2(\partial_j \Omega_h)$. It is well known that the trace cannot be defined for L^2-functions, however we note that, for example, the space $H^1(\Omega_h)$ fulfils the requirements. The extra request for $\boldsymbol{V}(\Omega_h)$ on the interface is due to the low regularity of the trace on $H_{\nabla\cdot}(\Omega_h)$, which is related to the Robin-type nature of the coupling condition, see [2], [49].

The weak formulation of the mixed-dimensional Darcy problem reads: find $(q_h, p_h, q_l, p_l, \lambda_j) \in V(\Omega_h) \times Q(\Omega_h) \times V(\Omega_l) \times Q(\Omega_l) \times W(\Gamma_j)$ such that

$$\begin{aligned}
\left(\mathcal{K}_h^{-1} q_h, v\right)_{\Omega_h} - (p_h, \nabla \cdot v)_{\Omega_h} + \left(\Xi_j^h \lambda_j, tr\, v \cdot n_h\right)_{\partial_j \Omega_h} &= 0 && \forall v \in V(\Omega_h),\\
-(\nabla \cdot q_h, w)_{\Omega_h} &= -(f_h, w)_{\Omega_h} && \forall w \in Q(\Omega_h),\\
\left(K_l^{-1} q_l, v\right)_{\Omega_l} - (p_l, \nabla \cdot v)_{\Omega_l} &= 0 && \forall v \in V(\Omega_l),\\
-(w, \nabla \cdot q_l)_{\Omega_l} + \left(\Xi_j^l \lambda_j, w\right)_{\Omega_l} &= -(f_l, w)_{\Omega_l} && \forall w \in Q(\Omega_l),\\
\left(\kappa_j^{-1} \lambda_j, \mu\right)_{\Gamma_j} + \left(\Pi_j^l p_l, \mu\right)_{\Gamma_j} - \left(\Pi_j^h tr\, p_h, \mu\right)_{\Gamma_j} &= 0 && \forall \mu \in W(\Gamma_j).
\end{aligned}$$

(3.5)

Here $(\cdot,\cdot)_A$ is the L^2-scalar product on the set A. The problem is well posed as shown in [47]. We emphasize that, apart from the extra regularity assumptions on $\partial_j \Omega_h$, the variational formulation for the subdomains have the same structure as a fixed-dimensional problem.

Next, we state an integral formulation for the subdomain problems, expressed in primal form, that is, considering only the pressure variable. To that end, let $\omega_h \subset \Omega_h$ and $\omega_l \subset \Omega_l$ be subdomains (grid cells in the discrete setting) in the higher- and lower-dimensional domains. Likewise, $\omega_\gamma \subset \Gamma_j$ is a subdomain of the interface. In the view of subsequent considerations, we assume that the subdomains ω_h are non-overlapping and fully cover Ω_h, and similarly for ω_l and ω_γ. Additional requests on the shape regularity of ω_h, ω_l and ω_γ depend on the numerical scheme. The integral formulation of (3.4) then reads: find (p_h, p_l, λ_j) such that

$$\begin{aligned}
\int_{\partial\omega_h \setminus \partial_j\Omega_h} \mathcal{K}_h \nabla p_h \cdot n_{\partial\omega_h} \,\mathrm{d}\sigma + \int_{\partial\omega_h \cap \partial_j\Omega_h} \Xi_j^h \lambda_j \,\mathrm{d}\sigma &= \int_{\omega_h} f_h \,\mathrm{d}x && \omega_h \subset \Omega_h, \\
\int_{\partial\omega_l} \mathcal{K}_l \nabla p_l \cdot n_{\partial\omega_l} \,\mathrm{d}\sigma - \int_{\omega_l} \Xi_j^l \lambda_j \,\mathrm{d}x &= \int_{\omega_l} f_l \,\mathrm{d}x && \omega_l \subset \Omega_l, \\
\int_{\omega_\gamma} \kappa_j^{-1} \lambda_j \,\mathrm{d}x + \int_{\omega_\gamma} \Pi_j^l p_l \,\mathrm{d}x - \int_{\omega_\gamma} \Pi_j^h tr\, p_h \,\mathrm{d}x &= 0 && \omega_\gamma \subset \Gamma_j,
\end{aligned} \tag{3.6}$$

where we have indicated with $\mathrm{d}x$ and $\mathrm{d}\sigma$ the infinitesimal measure for equi-dimensional and one co-dimensional integrals, respectively, with respect to the considered cell dimension. The vector $n_{\partial\omega}$ denotes the outward unit normal of ω. The equations are written on all subdomains ω and the global problem is given once the continuity of normal fluxes is imposed on each $\partial\omega$.

We make two remarks related to the discretization of the above equations. First, both the variational and integral formulations are very close to the corresponding fixed-dimensional problems, thus there is considerable scope for reuse of existing software as discussed below. Second, seen from the interface, the subdomain discretization acts as an unspecified Neumann-to-Dirichlet map that converts the interface fluxes into pressures to be projected to the interface. The formulation is independent of the actual discretization on the subdomains, and there is no requirement the same discretization be used on the two neighboring subdomains (of an interface). For more information on the formulation, confer [39].

3.1.3 Implementation

From the variational and integral formulations stated above, we see that for a discretization on a generic subdomain Ω_i to interact with the interface problem, we need to provide operators which:

1) Handle Neumann boundary data on the form $\Xi_j^i \lambda_j$, for all interfaces Γ_j for which Ω_i is the higher-dimensional neighbor.
2) Handle source terms $\Xi_j^i \lambda_j$ from interfaces Γ_j for which Ω_i is the lower-dimensional neighbor.
3) Provide a discrete operator $tr\, p_i$ so that Π_j^i can project the pressure trace from $\partial_j\Omega_i$ to interfaces Γ_j for which Ω_i is the higher-dimensional neighbor.
4) Provide a pressure p_i so that Π_j^i can project the pressure to all Γ_j for which Ω_i is the lower-dimensional neighbor.

Of these, all but the third operation is readily available in any reasonable implementation of a discretization scheme for elliptic equations. For the discrete pressure trace there is some room for interpretation; the simplest approach is to associate the trace with the pressure in cells immediately

next to the interface. Higher-order trace reconstruction operators, utilizing the construction of the discretization scheme at hand, are also possible; our implementation of finite volume methods for flow allows for sub-cell variations in pressure so that the discrete pressure at $\partial_j \Omega_i$ differs from the cell center pressure closest to the boundary.

It is instructive to write out the structure of the coupled system for our case with two subdomains Ω_h and Ω_l separated by an interface Γ_j. Denote by y_h, y_l and ξ_j the vectors of discrete unknowns in Ω_h, Ω_l and on Γ_j, respectively. As we make no assumptions that the same discretization scheme is applied in both subdomains, these may contain different sets of unknowns. Specifically, the unknown can be cell center pressures only, or cell center pressure and face fluxes, depending on the discretization scheme applied. The discrete coupled system can then be represented on the generic form

$$\begin{pmatrix} A_h & 0 & N_h \Xi_j^h \\ 0 & A_l & S_l \Xi_j^l \\ -\Pi_j^h P_h & \Pi_j^l P_l & D_j \end{pmatrix} \begin{pmatrix} y_h \\ y_l \\ \xi_j \end{pmatrix} = \begin{pmatrix} f_h \\ f_l \\ 0 \end{pmatrix}. \tag{3.7}$$

Here, A_h and A_l are the fixed-dimensional discretizations on the subdomains, N_h is the discretization of Neumann boundary conditions on Ω_h, and S_l is the discretization of source terms in Ω_l. Furthermore, P_h provides a discrete representation of the pressure trace operator on Ω_h and P_l gives the pressure unknowns in Ω_l; the latter is an identity operator for the integral formulations presented on primal form and strips away flux unknowns in the dual formulation. Finally, D_j is the discretization of (3.3). In accordance with the second constraint on mixed-dimensional modeling discussed in Section 2.2, there is no direct coupling between Ω_h and Ω_l. Global boundary conditions are left out of the system; as a technical detail we note that for some discretization schemes, *e.g.* multi-point flux approximation (Mpfa) methods, the global boundary conditions can also give a contribution to the right-hand-side of the interface equation.

The form (3.7) suggests an implementation strategy, based on the graph representation of the mixed-dimensional domain, which also exploits reuse of software for fixed-dimensional problems: On the graph nodes, that is the subdomains, the pressure equation is discretized as if it were a fixed-dimensional problem. The interface law is discretized by traversal of the graph edges; this operation will communicate with the discretizations in the neighboring subdomains to obtain the terms represented in the last column and row of (3.7).

The PorePy implementation of the above method represents the mortar variable by piecewise constant functions. Due to the decoupling, there is no requirement that the same numerical method be used on all subdomains, and indeed PorePy gives complete flexibility in this respect by an implementation of the coupling structure (3.7) which is independent of the individual subdomain discretizations. PorePy offers four discretization schemes for the flow problem: Lowest order Raviart-Thomas mixed finite elements combined with a piecewise constant pressure approximation (RT0-P0) [49], the lowest order mixed virtual element method (Mvem) [50], [51], and two finite volume schemes: the two- and multi-point flux approximations (Tpfa, Mpfa) [52]–[54]. Our implementation for the coupled mixed-dimensional problem relies on the analysis carried out in [39], which provides a theoretical background to obtain a stable global scheme.

3.2 Fully coupled flow and transport

We next turn to simulation of fully coupled flow and transport, as an example of a multiphysics problem with variable couplings within and between subdomains. We consider the mixing of two incompressible and miscible species of different viscosities. We put emphasis on the modeling of the mixed-dimensional dynamics and discuss some implementation aspects. For discretization, we limit ourselves to finite volume methods for the problem written in primal form. We present the governing equations on integral form only with details on how to handle the advective part at the interfaces.

3.2.1 Continuous formulation

We start by considering a single subdomain Ω_i. Denote the pressure in a subdomain $\omega_i \subset \Omega_i$ by p_i. We represent the species evolution by the mass concentration c_i in ω_i. By the incompressibility of the fluids, the conservation of total mass within ω_i can be written as

$$\int_{\partial\omega_i} q_i \cdot n_{\partial\omega_i} \, \mathrm{d}\sigma = \int_{\omega_i} f_i \, \mathrm{d}x, \tag{3.8}$$

where f_i represents the total volumetric sources and sinks. The Darcy flux q_i, depends on both pressure and mass concentration, via the fluid viscosity $\mu = \mu(c_i)$, and is given by

$$q_i + \frac{\mathcal{K}_i}{\mu(c_i)} \nabla p_i = 0. \tag{3.9}$$

Here $\mathcal{K}_i$ denotes the effective tangential permeability of Ω_i. Conservation of mass for each species is expressed by the equation

$$\int_{\omega_i} \phi_i \frac{\partial c_i}{\partial t} \, \mathrm{d}x + \int_{\partial\omega_i} w_i \cdot n_{\partial\omega_i} \, \mathrm{d}\sigma = \int_{\omega_i} g_i \, \mathrm{d}x \tag{3.10}$$

Here, ϕ_i represents the effective porosity, g_i denotes sources and sinks for the species, and the flux w_i is composed by a diffusive and an advective term

$$w_i + \mathcal{D}_i \nabla c_i - c_i q_i = 0, \tag{3.11}$$

where $\mathcal{D}_i$ is the effective diffusivity of Ω_i. We note that the equations are coupled via the concentration dependency of viscosity and the presence of the Darcy flux in the advective transport.

The interaction between two neighboring subdomains Ω_h and Ω_l again goes via the common interface Γ_j. The total flux over Γ_j, denoted by λ_j, is given by (3.3), where the interface viscosity μ_j is modeled as a function of the mean of the concentrations on the two sides,

$$\mu_j = \mu_j \left(\frac{\Pi_j^l c_l + \Pi_j^h tr\, c_h}{2} \right). \tag{3.12}$$

Mass flux over Γ_j is again governed by an advection-diffusion relation: The diffusion term β_j is, in analogy with the corresponding term for the Darcy flux, given by

$$\beta_j + \delta_j\left(\Pi_j^l c_l - \Pi_j^h tr\ c_h\right) = 0, \tag{3.13}$$

with δ_j representing the effective diffusivity over the interface Γ_j. For the advective term η_j, we introduce an upstream-like operator based on the Darcy interface flux:

$$Up\left(c_h, c_l; \lambda_j\right) = \begin{cases} \Pi_j^h tr\ c_h, & \text{if } \lambda_j \geq 0 \\ \Pi_j^l c_l, & \text{if } \lambda_j < 0. \end{cases} \tag{3.14}$$

With this, the advective interface flux η_j is given by the relation

$$\eta_j - \lambda_j Up\left(c_h, c_l; \lambda_j\right) = 0. \tag{3.15}$$

What remains in the problem formulation is to introduce the coupling terms in the subdomain equations and introduce global boundary conditions. As all the interface variables are fluxes, their treatment is analogous to that discussed for the flow problem in Section 3.1. For Ω_h, the interface fluxes enter as flux boundary conditions for the total mass flux (λ_j) and mass concentration (β_j, η_j) conservation equations, while for Ω_l, the fluxes enter as corresponding source terms. Finally, global boundary conditions are imposed in the standard way for elliptic and advection-diffusion problems, see *e.g.* [55]. With few modifications, our formulation can handle a purely advective problem, like transport of a passive scalar. In this case the elliptic operators (interface and mortar law included) are not considered.

The equations (3.8)-(3.15) define the governing equations in all subdomains and on all interfaces. The only exception is 0d domains, wherein the fluid mass and concentration fluxes are void, and the governing equations simply balance the fluxes of neighboring interfaces with possible source terms in the point domain.

3.2.2 Implementation

The equations are discretized with finite volume methods, by letting ω_i represent a computational cell. To discretize the flux expression, we apply single point upstreaming for the advective flux [56] and Mpfa for the diffusive terms both in (3.8)-(3.9) and (3.10)-(3.11), as described in Section 3.1. These operations can be carried out independently on individual subdomains, thus they can readily reuse existing implementations for fixed-dimensional problems.

To discretize the interface laws, we need projection operators for scalar quantities (pressure and mass concentration) from subdomains to interfaces, and projections of fluxes from interfaces back to subdomains. For the diffusive fluxes, the treatment is identical to that described in Section 3.1 for the elliptic equation. Similarly, the advective terms will appear respectively as flux boundaries and source terms for the higher- and lower-dimensional neighbors of an interface. Handling of these extra terms should be straightforward in any existing code for fixed-dimensional problems.

Finally, we note that governing equations are non-linearly coupled via the viscosity and the presence of the Darcy flux in the advective transport terms. A non-linear solver is therefore needed. Within PorePy, this is most easily handled by an automatic differentiation module, which is used for the simulations reported in Section 5.1.

3.3 Poromechanical fracture deformation by contact mechanics

Our final set of model equations considers poroelastic deformation of a fractured medium, where the fractures may open and / or undergo abrupt slip if the frictional forces are insufficient to withstand tangential tractions on the fracture surface. This process is important in applications such as geothermal energy extraction and CO_2 storage. Moreover, modeling of the process leading up to and under sliding is non-trivial due to i) the coupled poreelastic processes, ii) heterogeneous modeling equations between subdomains, iii) the need to use non-standard constitutive laws to relate primary variables during sliding, iv) non-smooth behavior of the constitutive laws in the transition from sticking to sliding of a fracture. Modeling of this process is an active research field, see *e.g.* [57]–[59], and so this is an example where the availability of a flexible prototyping framework for this research is extremely useful.

Herein, we present a set of governing equations which borrows modeling concepts from contact mechanics to describe the sliding problem. Our formulation has no notion of a displacement inside the fracture, instead the fracture deformation is described by the displacement jump over the fracture surface. We show how the model is naturally formulated and implemented in our mixed-dimensional framework, by defining displacement variables on the matrix-fracture interface.

3.3.1 Governing equations

As modeling of deformation of intersecting fractures is non-trivial, we limit our exposition to media with non-intersecting fractures. Flow and deformation in the rock matrix, represented by the subdomain $\Omega_h \in \mathbb{R}^n$, are then governed by Biot's equations for poroelasticity [60]

$$\nabla \cdot (\mathcal{C}_h \nabla_s u_h - \alpha_h p_h I) = b_h, \tag{3.16}$$

$$\alpha_h \frac{\partial (\nabla \cdot \dot{u}_h)}{\partial t} + \theta_h \frac{\partial p_h}{\partial t} - \nabla \cdot \left(\frac{\mathcal{K}_h}{\mu_h} \nabla p_h \right) = f_h.$$

Here, the first equation represents conservation of momentum, with the acceleration term neglected, while the second equation expresses conservation of mass. The primary variables are the displacements, u_h, and the fluid pressure p_h. The stiffness matrix $\mathcal{C}_h$ can for linear isotropic media be expressed purely in terms of the first and second Lamé parameters, and the stress can be computed as $\sigma_h = \mathcal{C}_h \nabla_s u_h$, where ∇_s is the symmetric gradient. Furthermore, α_h is the Biot constant, I the second order identity tensor, b_h denotes body forces, θ_h the effective storage term, $\mathcal{K}_h$ the permeability and μ_h the viscosity. We also assume boundary conditions are given on the global boundary.

Next, consider an interface Γ_j between the higher-dimensional subdomain Ω_h and the lower-dimensional domain Ω_l. Denote the displacement variable on Γ_j by u_j. We emphasize that u_j is a vector in $\mathbb{R}^n$, that is, it represents the displacement in both the tangential and normal direction of Ω_l. We will require continuity between u_h and u_j, expressed as $\Pi_j^h tr\, u_h = u_j$, where we recall that the trace operator maps to $\partial_j \Omega_h$, the part of the boundary of Ω_h that coincides with Γ_j. We also need to introduce the jump in displacement, $[\![u_j]\!]$, between the two interfaces on opposing sides of Ω_l, see Figure 4 for an illustration. The jump is decomposed into the tangential jump $[\![u_j]\!]_\tau$ and the normal jump $[\![u_j]\!]_n$.

The mechanical state in Ω_l is described by the contact pressure σ_l, which again is a vector in $\mathbb{R}^n$, with tangential and normal components $\sigma_{l,n}$ and $\sigma_{l,t}$, respectively. Our model also includes fluid flow in the fracture Ω_l, which is governed by conservation of mass

$$\frac{\partial}{\partial t}\left(a(\llbracket u_j \rrbracket)\right) + \theta_l \frac{\partial p_l}{\partial t} - \nabla \cdot (\mathcal{K}_l \nabla p_l) - \Xi_j^l \lambda_j = f_l. \tag{3.17}$$

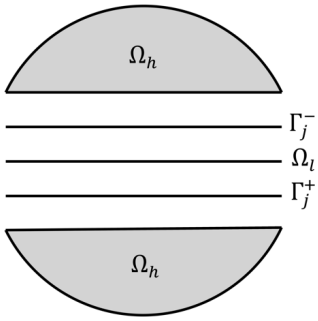

Figure 4: Illustration of a lower-dimensional domain, Ω_l, that has two interfaces, Γ_j^- and Γ_j^+, with a higher dimensional domain, Ω_h. The inerfaces on opposing sides are identified by a positive and negative index.

Here, the time derivative of the aperture $a(\llbracket u_j \rrbracket)$ represents changes in the available volume due to changes in the displacement jump; in general this can be both reversible changes due to normal displacement of the fracture, and irreversible changes caused by shear dilation [3]. In the following, we only consider the normal part, *i.e.* $a(\llbracket u_j \rrbracket) = \llbracket u_j \rrbracket_n$. Similarly, it can be of interest to consider changes in the permeability K_l due to changes in aperture, although we shall not consider this topic herein. Finally, θ_l denotes the effective storage term. As in the previous sections, the relation between the fluid pressures in Ω_h and Ω_l is governed by a flux law of the type (3.3), and we let λ_j denote the interface variable that represents fluid flux between the domains.

The relation between σ_l and $\llbracket u_j \rrbracket$ is modeled by borrowing techniques from contact mechanics as summarized here; for a full discussion see [61]. Balance of forces between the poroelastic stress in Ω_h and the contact pressure in Ω_l is expressed as

$$\Pi_j^h \, n_h \cdot (\sigma_h - \alpha_h p_h I) = \Pi_j^l \sigma_l - \, (\Pi_j^h \, n_h) \, (\Pi_j^l \alpha_l p_l) \quad \text{on } \Gamma_j. \tag{3.18}$$

In the direction normal to Ω_l, the contact stress is zero only when the displacement jump is nonzero, that is

$$\llbracket u_j \rrbracket_n \leq 0, \quad \sigma_{l,n} \leq 0, \quad \llbracket u_j \rrbracket_n \sigma_{l,n} = 0. \tag{3.19}$$

The motion in the tangential direction is controlled by the ratio between the tangential force $\sigma_{l,\tau}$ and the maximum available frictional force $F\sigma_{l,n}$, where F is the friction coefficient. The time derivative of the displacement jump is zero until the frictional force is overcome; for larger tangential forces, the derivative of the displacement jump and tangential force are parallel:

$$\begin{cases} ||\sigma_{l,\tau}|| \leq -F\sigma_{l,n}, \\ ||\sigma_{l,\tau}|| < -F\sigma_{l,n} \rightarrow \llbracket \dot{u}_j \rrbracket_\tau = 0, \\ ||\sigma_{l,\tau}|| = -F\sigma_{l,n} \rightarrow \exists \alpha \in \mathbb{R}, \, \sigma_{l,\tau} = -\alpha^2 \llbracket \dot{u}_j \rrbracket_\tau, \end{cases} \tag{3.20}$$

where $||\cdot||$ represents the Euclidean norm and $[\![\dot{u}_j]\!]_\tau$ represents the sliding velocity. We emphasize that the contact conditions are formulated in terms of the contact pressure σ_l, with no contribution from the fluid pressure p_l.

3.3.2 Implementation in mixed-dimensional framework

It is instructive to discuss implementation of poroelastic contact mechanics within our mixed-dimensional modeling concept, starting from an existing implementation of poroelasticity in the matrix domain. This is a relevant case for many research codes, in particular the PorePy implementation for this problem was extended from a finite volume method, the multipoint stress approximation (Mpsa), originally developed for elastic and poroelastic deformation on a fixed-dimensional domain [62]–[64]. Below, we follow the equations presented above and identify variables and equations to be introduced.

First, the variables p_l and λ_j representing respectively fluid pressure in the fracture Ω_l and the fluid flux on the interface Γ_j between Ω_h and Ω_l, are introduced as discussed in detail in Section 3.1. This implies that $\partial_j\Omega_h$ is a Neumann boundary for fluid flow in Ω_h. We reiterate that the couplings introduced by this approach is standard for any discretization scheme for single-phase flow.

Second, the displacement in Ω_h must be coupled to the mortar displacement u_j on Γ_j. This is achieved by letting $\partial_j\Omega_h$ be a Dirichlet boundary, so that the condition $\Pi_j^h tr\, u_h = u_j$ can be enforced by the imposition of a boundary condition. The poroelastic stress at $\partial_j\Omega_h$ is computed from variables in Ω_h and on Γ_j, according to the discretization scheme applied in Ω_h. We note that mapping of displacements u_j onto the boundary $\partial_j\Omega_h$, and later stresses from $\partial_j\Omega_h$ to Γ_j requires vectorized versions of the projection operators discussed in Section 2.4; this is a straightforward extension.

Finally, the implementation must discretize the stress continuity as expressed by (3.18), and the relation between displacement jumps $[\![u_j]\!]$ and contact pressure σ_l (3.19)-(3.20). Stress continuity is enforced by projecting the discrete representation of the poroelastic stress on $\partial_j\Omega_h$ onto Γ_j, similarly projecting the discrete quantity $\sigma_l - p_l n$ from Ω_l to Γ_j and enforcing equality. The contact conditions are discretized by projecting $[\![u_j]\!]$ onto Ω_l, and then discretizing Equations (3.19) and (3.20). This is a non-linear term, in that the relation between $[\![u_j]\!]$ and σ_j depends on whether the fracture is open, sticking or slipping. In our implementation we use a semi-smooth Newton method to deal with the discontinuities in the solution, for details we refer to [61], [65].

As a final remark on data structures, we note that the full discrete system is rather complex, with different governing equations in different subdomains, and non-trivial couplings between variables that live on different grids. As illustrated by the run scripts for the simulation presented in Section 5.2 (can be downloaded from [66]), the mixed-dimensional grid structure and modeling concept break the implementation into manageable parts. Moreover, due to the strong modularization of the model and implementation, experimentation with model variations etc. is handled with minimal needs for adjustments.

4 Validation

To validate our modeling framework and its implementation in PorePy, we consider three test cases: A benchmark for flow problems in 2d fractured media, Mandel's problem for poroelasticity, and Sneddon's problem for fracture deformation in elastic media. Together, these cases probe a wide range

of the capabilities of the modeling framework and its PorePy implementation, including discretization schemes, multiphysics problems and time-dependent problems. The cases thus supplement previous testing of PorePy, reported in [39], [67]–[69]. The supplementary material provides detailed setups, including parameters for all simulations in Section 4 and 5. Scripts that reproduce all results reported herein can be accessed at [66]; see that reference or the supplementary material for install instructions.

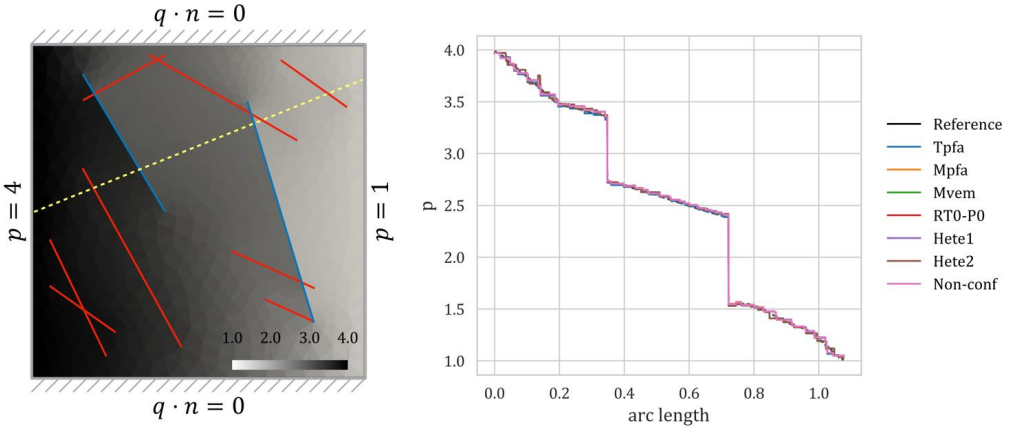

Figure 5: Left: A solution obtained with Mpfa on the coarsest mesh, showing the fracture network and the problem setup. The red lines represent conductive fractures whereas the blue lines are blocking fractures. The yellow line indicates the line of the pressure profile. Right: Pressure profiles for the discretization schemes used in the validation.

4.1 Flow in 2d fractured porous media

To validate the mixed-dimensional flow discretization, we consider Benchmark 3 of [70], which describes an incompressible single-phase flow problem in a fractured domain. The fracture network contains intersecting and isolated fractures; see Figure 5 for an illustration of the domain together with the pressure solution for the Mpfa discretization. The network contains both highly conductive and blocking fractures, see the supplementary material for details. The normal permeability in the fracture intersections is given by the harmonic average of the permeabilities of the intersecting fractures as suggested in [70], [71].

The aim of this case is twofold - we benchmark our code to well-established methods in the literature and present the full capability that our abstract structure can handle. For the latter, we consider four groups of discretization schemes and simulation grids: First, three homogeneous (the same for all the subdomains) discretizations: Tpfa, Mpfa and RT0-P0. Second, a case with the Mvem, where the cells of the rock matrix are constructed by a clustering procedure starting from a more refined simplicial grid, see [68] for details. Third, two heterogeneous discretizations where RT0-P0 and Mvem for the rock matrix are combined with Tpfa for the fractures (labeled Hete1 and Hete2, respectively). Fourth, a case where the fracture grid is twice as fine as the matrix grid, with the mortar grids non-conforming to the surrounding grids (Non-conf). In this case we consider the RT0-P0 scheme. We use simplex grids in all cases that do not involve Mvem.

Figure 5 shows the domain with fractures, boundary conditions and a representative numerical solution. The figure also depicts a plot of the pressure along the line $(0,0.5) - (1,0.9)$, with the reference

solution (equi-dimensional problem computed on a much finer grid) colored in black. We observe good agreement between the solutions obtained in PorePy and the reference solution. We also consider a sequence of grids to compute the error relative to the reference solution, as done in the original benchmark. Figure 6 shows the decay of the normalized L^2 error for the rock matrix and the union of the fracture subdomains. In the former, we notice a first order of convergence for all the considered methods. The convergence rate for the fracture subdomains is sublinear, as was also observed in the original benchmark, see [70].

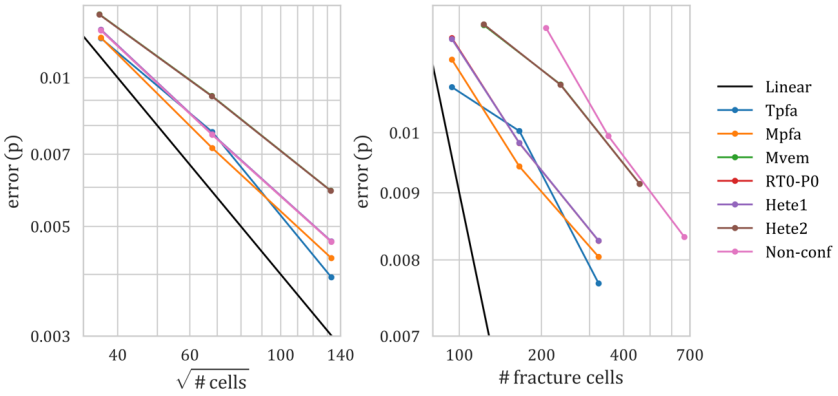

Figure 6: Left: Convergence of the pressure unknown for the matrix subdomain. Right: Convergence for the pressure unknown for the fracture subdomains.

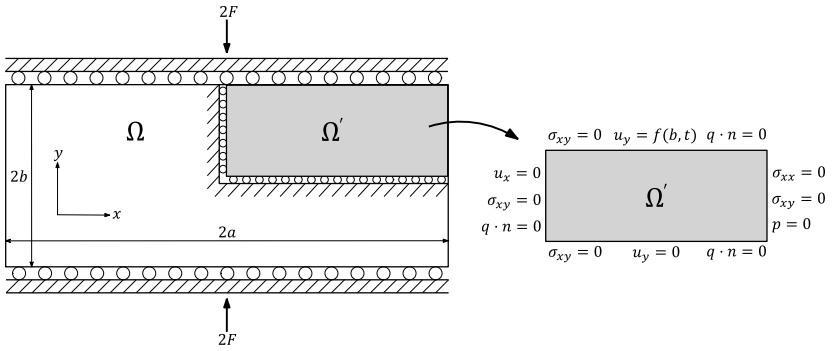

Figure 7: Mandel's problem. Left: Schematic representation of the full and positive quarter domains, Ω and Ω′. Right: Quarter domain showing the boundary conditions.

4.2 Mandel's problem in poroelasticity

The next test case considers a poroelastic material, with a setup defined by Mandel's problem [72], [73], for which an analytical solution is available. While the problem geometry does not include lower-dimensional objects, the case tests the implementation of the poroelastic code and shows the framework's flexibility to deal with coupled problems and time-dependent mixed boundary conditions.

The original problem consists of an isotropic poroelastic slab of width $2a$ and height $2b$ sandwiched by two rigid plates (Figure 7). Initially, two compressive constant loads of intensity $2F$ are applied to the slab at $y = \pm b$. At $x = \pm a$, fluid is free to drain, and edges are stress free. Gravity contributions are neglected.

This problem is modeled using the quasi-static Biot equations, as presented in Section 3.3.1. Exploiting the symmetry of the problem, we focus on the positive quarter domain Ω', rather than the full domain Ω, see Figure 7 for an illustration, and for boundary conditions. Note that the vertical displacement at the top of the domain is time-dependent and given by the exact solution, see [74].

The simulation parameters were taken from [75], see also the supplementary material for details. The coupled problem is discretized in space using Mpsa/Mpfa for the mechanics and flow, respectively. For the time discretization we use implicit Euler. The computational mesh is unstructured and composed by 622 triangular elements. The results are shown in FigureFigure 8 in terms of dimensionless quantities and are in good agreement with [75] for both pressure and displacement.

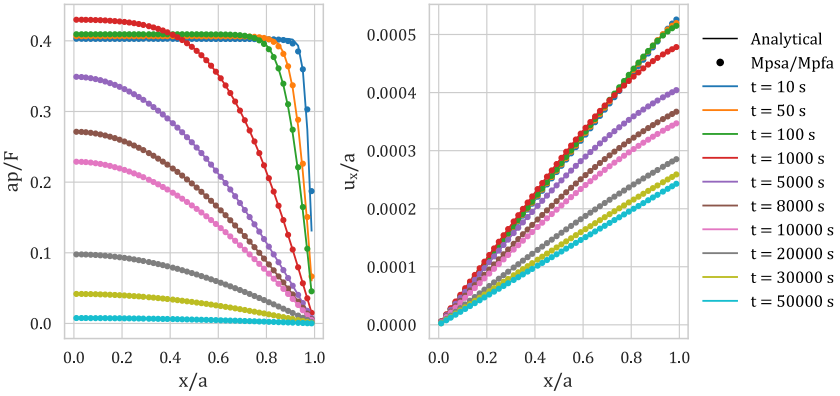

Figure 8: Solutions to Mandel's problem: Dimensionless pressure (left) and horizontal displacement (right) profiles for several times.

4.3 Sneddon's problem of fracture deformation

In this example, a square domain with a single fracture located in the middle is considered. The fracture forms an angle β with the horizontal direction (see Figure 9) and is subjected to a constant pressure p_0 acting on its interior. This pressure can be interpreted as a pair of normal forces acting on either side of the fracture. An analytical solution for the relative normal displacement along the fracture was derived by Sneddon [76] for an infinite domain, and has the following form:

$$[\![u_j]\!]_n(d_f) = \frac{(1-\nu)p_0 L}{G}\sqrt{1-\frac{d_f^2}{\left(\frac{L}{2}\right)^2}} \tag{4.1}$$

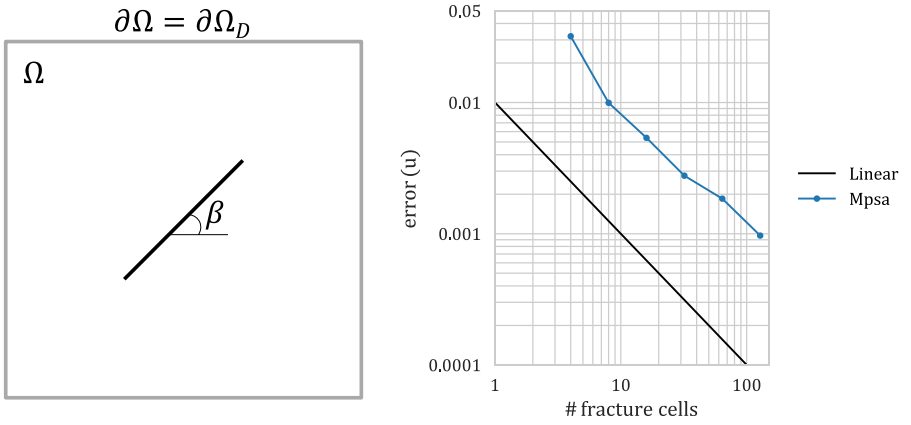

Figure 9: Setup and convergence of Sneddon's problem Left: Schematic representation of the domain. Right: Average convergence behavior of the relative normal displacement along the fracture. Each dot corresponds to the average of 140 simulations.

where ν and G are the Poisson's ratio and shear modulus, respectively, L is the fracture length, and d_f denotes the distance from the center of the fracture.

In our calculations, the conditions of infinite domain are replaced with a Dirichlet boundary, where the prescribed displacement is set equal to the analytical solution calculated using the procedure illustrated in [77]. The accuracy of the numerical solution is very sensitive to the discretization, specifically the cell configuration, at the fracture tips [58]. To reduce the dependency on specific grid realizations, the values of the numerical solution reported in Figure 9 are the average of a group of 20 x 7 = 140 computations per level of grid resolution, with 7 different fracture angles β in the range $0^\circ - 30^\circ$ and 20 grid realizations per fracture. With six levels of grid refinement, the full study contains 20 x 7 x 6 = 840 simulations. Figure 9 summarizes the results in the form of the error in relative normal displacement between the analytical solution (4.1) and the numerical solution as a function of the fracture resolution, i.e. number of fracture elements. The method provides first-order convergence on average.

5 Applications: Multiphysics simulations

Having established the accuracy of PorePy for central test cases that involve mixed-dimensional geometries, we go on to present two multiphysics cases of high application relevance: A non-linearly coupled flow and transport problem, and fracture reactivation caused by fluid injection. The motivation for the simulations is to illustrate further capabilities of the modeling framework and its PorePy implementation, including simulations on complex 3d fracture networks, automatic differentiation applied to non-linear problems, non-matching grids, and simulation of fracture deformation in a poromechanical setting.

5.1 Fully coupled flow and transport

This example has two main purposes. First, we consider a non-linear coupled flow and transport process as described in Section 3.2. We apply the automatic differentiation functionality in PorePy to obtain the Jacobian of the global system of equations, which is then used in a standard Newton method to solve

the non-linear problem. Second, we illustrate the flexibility of the mixed-dimensional approach by using non-matching meshes on a relatively complex fracture network.

We consider the injection of a highly viscous fluid into a domain initially filled with a less viscous fluid. The two fluids are miscible, with their distribution described by the mass concentration $c \in [0, 1]$, and with a viscosity ratio of the two fluids given by $\mu(c) = \exp(c)$. In the parameter regime studied in this example, the transport in the fractures is advection dominated, while the transport in the rock matrix is dominated by diffusion; see the supplementary material for the details about the parameters. We remark that PorePy has also been applied to study unstable displacement in 2d domains, see [78] for details.

The mixed-dimensional domain considered in this example consists of one 3d domain, 15 2d fracture domains, 62 1d domains and 9 0d domains. On this geometry, two computational grids are constructed: The first has matching grids in all dimensions, with in total 20812 cells, out of which 16766 are 3d cells and 3850 are 2d fracture cells. The second mixed-dimensional grid has a 3d grid identical to the first grid, whereas the lower-dimensional objects are assigned refined grids with in total 13839 2d fracture cells, thus the 3d-2d interfaces have non-matching grids. The combination of the non-linearity and the non-matching grids provides a challenging test for the robustness of the PorePy implementation of subdomain couplings and provides an illustration of the framework's flexibility.

Figure 10 shows the average concentration profile in the fractures for the two meshes. There are no significant differences in the average concentration profiles in the two cases, indicating the stability of the implementation of the non-matching case. Figure 11 shows a snapshot of the concentration in the fractures and the rock matrix at time $t = 20$. The diffusive front in the rock matrix has only moved a few grid cells at the break-through, however, due to the diffusion and advection from the fractures to the rock matrix, the concentration has increased in considerable parts of the rock matrix. We observe no irregularities for the solution produced on the non-matching grid, confirming PorePy's ability to deal with non-standard grid couplings also for challenging physical regimes.

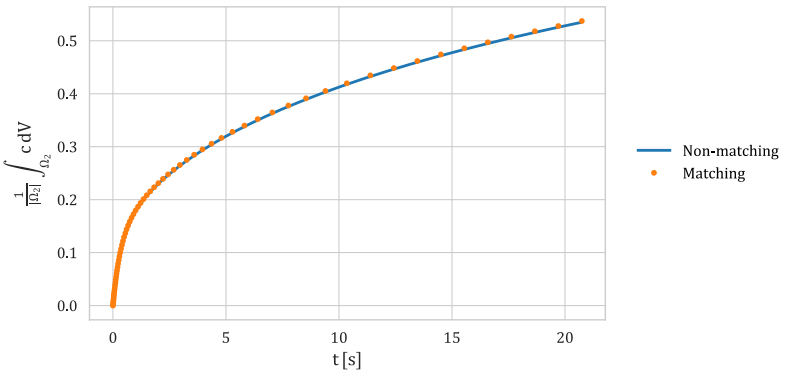

Figure 10. Fully coupled flow and transport: Comparison of average concentration in the fracture network for a simulation with matching meshes and a simulation with non-matching meshes.

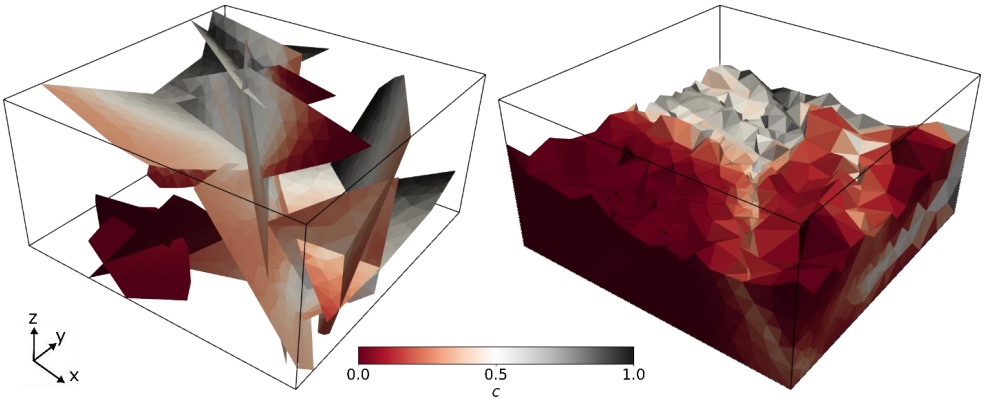

Figure 11. Fully coupled flow and transport: Concentration in the fractures (left) and in the rock matrix (right) for the coupled flow and transport problem given in Section 3.2 at the end time of the simulation (t=20). In the right figure the rock matrix domain is cropped, and the fractures removed to reveal the concentration inside the domain. The black lines indicate the domain boundary. A non-matching mesh is used where the mesh in the fractures are much finer than the mesh in the rock matrix. The increase in the concentration in the rock matrix is mainly due to advection and diffusion from the fractures.

5.2 Poroelasticity and fracture deformation

The final example aims at demonstrating the modelling framework's and PorePy's applicability to non-standard combinations of physical processes in different domains and thereby its potential for method development and prototyping. With the critical events taking place on individual fractures as a result of processes in the rock matrix, it also serves as an example of the importance of incorporating dynamics of both the matrix and explicitly represented fractures, as done in DFM models.

We consider a reservoir of idealized geometry containing three fractures numbered from 1 through 3, whereof the first contains an injection well, see Figure 12. On this geometry, we solve the governing equations presented in Section 3.3. We impose injection over a 25-day period and an anisotropic background stress regime, producing a scenario well suited to demonstrate different fracture dynamics. We investigate the dynamics both during a 25-day injection phase, and during the subsequent 25-day relaxation phase, at the end of which the pressure has almost reached equilibrium once more. The full set of parameters may be found in the supplementary material.

The dynamics on the fractures throughout the simulation are summarized in Figure 12, while the spatial distribution of the fracture displacement jumps at the end of the injection phase is shown in Figure 13. During the injection phase, there are tangential displacement jumps on all three fractures, appearing first on the favorably oriented fractures 2 and 3, and then on fracture 1 (injection). Normal displacement jumps appear on fracture 1 along with the tangential jumps, and on fracture 3 somewhat later. On fracture 2, which is located furthest away from the injection point, no normal displacement jumps appear. During the relaxation phase, we note that while the normal displacement jumps vanish, all tangential jumps remain due to the friction. We also observe a slight increase in tangential displacement jumps on fractures 2 and 3 at the time of shut-in, as the normal jump on fracture 1 vanishes.

The example demonstrates how modeling of complex coupled processes in great detail is possible through the use of DFM models. Furthermore, the structure and modularity of PorePy makes it ideally suited for experimentation with mathematical models, as well as prototyping of simulation approaches.

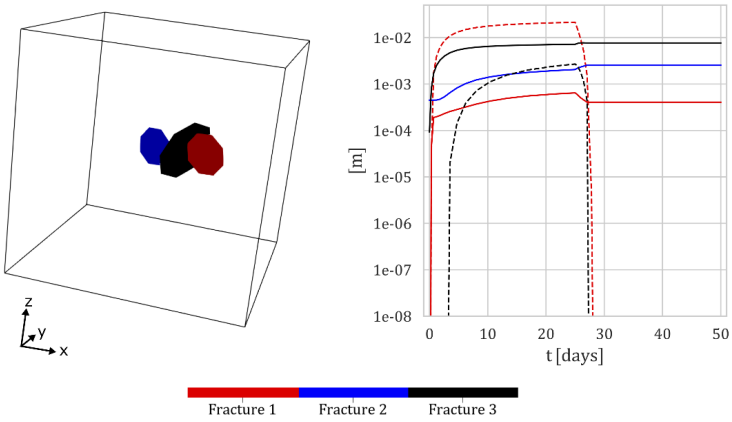

Figure 12: Left: Domain geometry with numbering of the three fractures. Fluid is injected in fracture 1 during the first 25 days, after which the well is shut. Right: L^2norm normalized by fracture area of the normal (dashed lines) and tangential displacement jumps (solid lines) for each fracture.

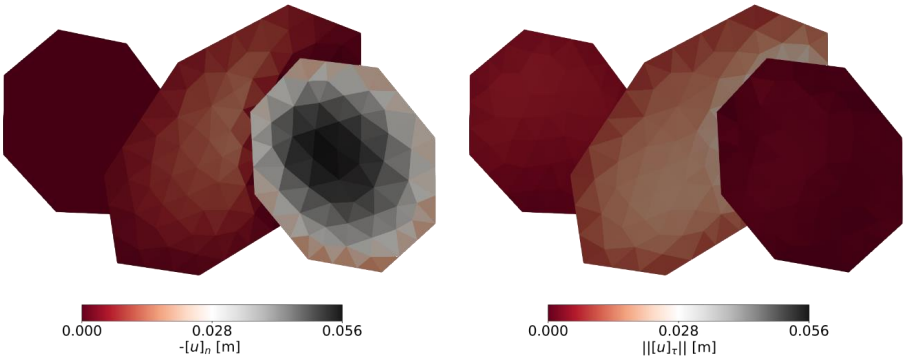

Figure 13: Normal and tangential displacements jumps on the fractures at the end of the injection phase to the left and right, respectively. The orientation of the fracture network corresponds to that in Figure 12, with the injection fracture to the right.

6 Conclusions

The complexity in modeling and simulation of multiphysics processes in fractured porous media, combined with a strong current research focus and corresponding developments, calls for flexible simulation tools that facilitate rapid prototyping of models and discretization methods. This paper presents design principles for simulation software for dynamics in fractured porous media, together with their implementation in the open-source simulation tool PorePy. The combined framework for

modeling and simulation is based on the Discrete Fracture Matrix model, where fractures and their intersections are represented as separate lower-dimensional geometric objects. The framework facilitates flexibility for multiphysics dynamics and reuse of existing code written for non-fractured domains; hence, it is well suited for extending other software packages to mixed-dimensional problems.

The open-source software PorePy demonstrates the capabilities of the suggested framework: It provides automatic meshing of complex fracture networks in two and three dimensions, and contains implemented numerical methods for flow, transport, poroelastic deformation of the rock, and fracture deformation modeled by contact mechanics. The implementation performs well for benchmark problems in flow, poroelastic deformation and fracture deformation. Further, multiphysics simulations of fully coupled flow and non-linear transport, and of fracture deformation under poromechanical deformation of a domain demonstrates the versatility of the software.

Acknowledgements

This work has been funded in part by Norwegian Research Council grant 250223, 244129/E20 and 267908/E20, and by a VISTA Scholarship from the Norwegian Academy of Science and Letters.

References

[1] B. Berkowitz, "Characterizing flow and transport in fractured geological media: A review," *Adv. Water Resour.*, vol. 25, no. 8–12, pp. 861–884, 2002.
[2] V. Martin, J. Jaffré, and J. E. Roberts, "Modeling Fractures and Barriers as Interfaces for Flow in Porous Media," *SIAM J. Sci. Comput.*, vol. 26, no. 5, pp. 1667–1691, 2005.
[3] N. Barton, S. Bandis, and K. Bakhtar, "Strength, deformation and conductivity coupling of rock joints," *Int. J. Rock Mech. Min. Sci. Geomech. Abstr.*, vol. 22, no. 3, pp. 121–140, 1985.
[4] N. Frih, J. E. Roberts, and A. Saada, "Modeling fractures as interfaces: a model for Forchheimer fractures," *Comput. Geosci.*, vol. 12, no. 1, pp. 91–104, 2008.
[5] J. Rutqvist, Y.-S. Wu, C.-F. Tsang, and G. Bodvarsson, "A modeling approach for analysis of coupled multiphase fluid flow, heat transfer, and deformation in fractured porous rock," *Int. J. Rock Mech. Min. Sci.*, vol. 39, no. 4, pp. 429–442, 2002.
[6] J. Burnell *et al.*, "Geothermal Supermodels: the Next Generation of Integrated Geophysical, Chemical and Flow Simulation Modelling Tools," *Proc World Geotherm. Congr.*, p. 7, 2015.
[7] K. Pruess, "TOUGH2: A General Numerical Simulator for Multiphase Fluid and Heat Flow," Report LBL-29400, 1991.
[8] G. E. Hammond, P. C. Lichtner, and R. T. Mills, "Evaluating the performance of parallel subsurface simulators: An illustrative example with PFLOTRAN: Evaluating the Parallel Performance of Pflotran," *Water Resour. Res.*, vol. 50, no. 1, pp. 208–228, 2014.
[9] M. G. Blöcher, M. Cacace, B. Lewerenz, and G. Zimmermann, "Three dimensional modelling of fractured and faulted reservoirs: Framework and implementation," *Geochemistry*, vol. 70, pp. 145–153, 2010.
[10] G. I. Barenblatt, Iu. P. Zheltov, and I. N. Kochina, "Basic concepts in the theory of seepage of homogeneous liquids in fissured rocks [strata]," *J. Appl. Math. Mech.*, vol. 24, no. 5, pp. 1286–1303, 1960.
[11] T. Arbogast, J. Douglas, Jr., and U. Hornung, "Derivation of the Double Porosity Model of Single Phase Flow via Homogenization Theory," *SIAM J. Math. Anal.*, vol. 21, no. 4, pp. 823–836, 1990.

[12] P. Lemonnier and B. Bourbiaux, “Simulation of Naturally Fractured Reservoirs. State of the Art: Part 1 – Physical Mechanisms and Simulator Formulation,” *Oil Gas Sci. Technol. – Rev. L’Institut Fr. Pétrole*, vol. 65, no. 2, pp. 239–262, 2010.
[13] P. Lemonnier and B. Bourbiaux, “Simulation of Naturally Fractured Reservoirs. State of the Art: Part 2 – Matrix-Fracture Transfers and Typical Features of Numerical Studies,” *Oil Gas Sci. Technol. – Rev. L’Institut Fr. Pétrole*, vol. 65, no. 2, pp. 263–286, 2010.
[14] J. D. Hyman, S. Karra, N. Makedonska, C. W. Gable, S. L. Painter, and H. S. Viswanathan, “dfnWorks: A discrete fracture network framework for modeling subsurface flow and transport,” *Comput. Geosci.*, vol. 84, pp. 10–19, 2015.
[15] J. Erhel, J.-R. de Dreuzy, and B. Poirriez, “Flow Simulation in Three-Dimensional Discrete Fracture Networks,” *SIAM J. Sci. Comput.*, vol. 31, no. 4, pp. 2688–2705, 2009.
[16] S. Berrone, S. Pieraccini, and S. Scialò, “On Simulations of Discrete Fracture Network Flows with an Optimization-Based Extended Finite Element Method,” *SIAM J. Sci. Comput.*, vol. 35, no. 2, pp. A908–A935, 2013.
[17] I. Berre, F. Doster, and E. Keilegavlen, “Flow in Fractured Porous Media: A Review of Conceptual Models and Discretization Approaches,” *Transp. Porous Media*, vol. https://doi.org/10.1007/s11242-018-1171-6, 2018.
[18] J. Noorishad and M. Mehran, “An upstream finite element method for solution of transient transport equation in fractured porous media,” *Water Resour. Res.*, vol. 18, no. 3, pp. 588–596, 1982.
[19] R. G. Baca, R. C. Arnett, and D. W. Langford, “Modelling fluid flow in fractured-porous rock masses by finite-element techniques,” *Int. J. Numer. Methods Fluids*, vol. 4, no. 4, pp. 337–348, 1984.
[20] V. Reichenberger, H. Jakobs, P. Bastian, and R. Helmig, “A mixed-dimensional finite volume method for two-phase flow in fractured porous media,” *Adv. Water Resour.*, vol. 29, no. 7, pp. 1020–1036, 2006.
[21] L. Li and S. H. Lee, “Efficient Field-Scale Simulation of Black Oil in a Naturally Fractured Reservoir Through Discrete Fracture Networks and Homogenized Media,” *SPE Reserv. Eval. Eng.*, vol. 11, no. 04, pp. 750–758, 2008.
[22] A. Fumagalli and A. Scotti, “A Reduced Model for Flow and Transport in Fractured Porous Media with Non-matching Grids,” in *Numerical Mathematics and Advanced Applications 2011*, A. Cangiani, R. L. Davidchack, E. Georgoulis, A. N. Gorban, J. Levesley, and M. V. Tretyakov, Eds. Berlin, Heidelberg: Springer Berlin Heidelberg, 2013, pp. 499–507.
[23] B. Flemisch, A. Fumagalli, and A. Scotti, “A Review of the XFEM-Based Approximation of Flow in Fractured Porous Media,” in *Advances in Discretization Methods*, vol. 12, G. Ventura and E. Benvenuti, Eds. Cham: Springer International Publishing, 2016, pp. 47–76.
[24] N. Schwenck, B. Flemisch, R. Helmig, and B. I. Wohlmuth, “Dimensionally reduced flow models in fractured porous media: crossings and boundaries,” *Comput. Geosci.*, vol. 19, no. 6, pp. 1219–1230, 2015.
[25] J. Jiang and R. M. Younis, “An improved projection-based embedded discrete fracture model (pEDFM) for multiphase flow in fractured reservoirs,” *Adv. Water Resour.*, vol. 109, pp. 267–289, 2017.
[26] B. Flemisch *et al.*, “DuMux: DUNE for multi-{phase,component,scale,physics,…} flow and transport in porous media,” *Adv. Water Resour.*, vol. 34, no. 9, pp. 1102–1112, 2011.
[27] S. K. Matthäi *et al.*, “Numerical simulation of multi-phase fluid flow in structurally complex reservoirs,” *Geol. Soc. Lond. Spec. Publ.*, vol. 292, no. 1, pp. 405–429, 2007.
[28] D. Gaston, C. Newman, G. Hansen, and D. Lebrun-Grandié, “MOOSE: A parallel computational framework for coupled systems of nonlinear equations,” *Nucl. Eng. Des.*, vol. 239, no. 10, pp. 1768–1778, 2009.

[29] K. Breede, K. Dzebisashvili, X. Liu, and G. Falcone, “A systematic review of enhanced (or engineered) geothermal systems: past, present and future,” *Geotherm. Energy*, vol. 1, no. 1, p. 4, 2013.
[30] W. Wang and O. Kolditz, “Object-oriented finite element analysis of thermo-hydro-mechanical (THM) problems in porous media,” *Int. J. Numer. Methods Eng.*, vol. 69, no. 1, pp. 162–201, 2007.
[31] J. Březina and J. Stebel, “Analysis of Model Error for a Continuum-Fracture Model of Porous Media Flow,” in *High Performance Computing in Science and Engineering*, vol. 9611, T. Kozubek, R. Blaheta, J. Šístek, M. Rozložník, and M. Čermák, Eds. Cham: Springer International Publishing, 2016, pp. 152–160.
[32] K.-A. Lie, *An Introduction to Reservoir Simulation Using MATLAB/GNU Octave: User Guide for the MATLAB Reservoir Simulation Toolbox (MRST)*, 1st ed. Cambridge University Press, 2019.
[33] K. Lie, S. Krogstad, I. S. Ligaarden, J. R. Natvig, H. M. Nilsen, and B. Skaflestad, “Open-source MATLAB implementation of consistent discretisations on complex grids,” *Comput. Geosci.*, vol. 16, no. 2, pp. 297–322, 2012.
[34] M. Alnæs *et al.*, “The FEniCS Project Version 1.5,” *Arch. Numer. Softw.*, vol. Vol 3, 2015.
[35] M. Blatt *et al.*, “The Distributed and Unified Numerics Environment, Version 2.4,” *Arch. Numer. Softw.*, vol. 4, 2016.
[36] F. Rathgeber *et al.*, “Firedrake: Automating the Finite Element Method by Composing Abstractions,” *ACM Trans. Math. Softw.*, vol. 43, no. 3, pp. 1–27, 2016.
[37] W. M. Boon, J. M. Nordbotten, and J. E. Vatne, “Functional Analysis and Exterior Calculus on Mixed-Dimensional Geometries,” *arXiv:1710.00556*, 2017.
[38] W. M. Boon and J. M. Nordbotten, “Stable Mixed Finite Elements for Linear Elasticity with Thin Inclusions,” *arXiv:1903.01757*, 2019.
[39] J. M. Nordbotten, W. M. Boon, A. Fumagalli, and E. Keilegavlen, “Unified approach to discretization of flow in fractured porous media,” *Comput. Geosci.*, vol. 23, no. 2, pp. 225–237, 2019.
[40] C. Geuzaine and J.-F. Remacle, “Gmsh: A 3-D finite element mesh generator with built-in pre- and post-processing facilities,” *Int. J. Numer. Methods Eng.*, vol. 79, no. 11, pp. 1309–1331, 2009.
[41] M. Karimi-Fard, “An Efficient Discrete-Fracture Model Applicable for General-Purpose Reservoir Simulators,” *SPE J.*, vol. 9, no. 2, 2004.
[42] M.-H. Hui, B. Mallison, and K.-T. Lim, “An Innovative Workflow to Model Fractures in a Giant Carbonate Reservoir,” *Proc Int Pet. Techn Conf*, p. 15, 2008.
[43] A. Quarteroni and A. Valli, *Domain decomposition methods for partial differential equations*. Oxford ; New York: Clarendon Press, 1999.
[44] S. Dong, L. Zeng, P. Dowd, C. Xu, and H. Cao, “A fast method for fracture intersection detection in discrete fracture networks,” *Comput. Geotech.*, vol. 98, pp. 205–216, 2018.
[45] T. Arbogast, L. C. Cowsar, M. F. Wheeler, and I. Yotov, “Mixed Finite Element Methods on Nonmatching Multiblock Grids,” *SIAM J. Numer. Anal.*, vol. 37, no. 4, pp. 1295–1315, 2000.
[46] U. Ayachit, *The ParaView guide: updated for ParaView version 4.3*, Full color version. Los Alamos: Kitware, 2015.
[47] W. M. Boon, J. M. Nordbotten, and I. Yotov, “Robust Discretization of Flow in Fractured Porous Media,” *SIAM J. Numer. Anal.*, vol. 56, no. 4, pp. 2203–2233, 2018.
[48] I. Berre *et al.*, “Call for participation: Verification benchmarks for single-phase flow in three-dimensional fractured porous media,” *arXiv:1809.06926*, 2018.
[49] D. Boffi, F. Brezzi, and M. Fortin, *Mixed Finite Element Methods and Applications*. Berlin, Heidelberg: Springer Berlin Heidelberg, 2013.
[50] L. B. da Veiga, F. Brezzi, L. D. Marini, and A. Russo, “Mixed Virtual Element Methods for general second order elliptic problems on polygonal meshes,” *ESAIM Math. Model. Numer. Anal.*, vol. 50, no. 3, pp. 727–747, 2016.

[51] L. B. da Veiga, F. Brezzi, L. D. Marini, and A. Russo, "$$H({\text {div}})$$ H (div) and $$H(\mathbf{curl})$$ H (curl) -conforming virtual element methods," *Numer. Math.*, vol. 133, no. 2, pp. 303–332, 2016.
[52] I. Aavatsmark, "An Introduction to Multipoint Flux Approximations for Quadrilateral Grids," *Comput. Geosci.*, vol. 6, no. 3–4, pp. 405–432.
[53] R. A. Klausen, F. A. Radu, and G. T. Eigestad, "Convergence of MPFA on triangulations and for Richards' equation," *Int. J. Numer. Methods Fluids*, vol. 58, no. 12, pp. 1327–1351, 2008.
[54] H. A. Friis, M. G. Edwards, and J. Mykkeltveit, "Symmetric Positive Definite Flux-Continuous Full-Tensor Finite-Volume Schemes on Unstructured Cell-Centered Triangular Grids," *SIAM J. Sci. Comput.*, vol. 31, no. 2, pp. 1192–1220, 2009.
[55] A. Quarteroni and A. Valli, *Numerical approximation of partial differential equations*, 2nd, corr. print ed. Berlin ; New York: Springer, 1997.
[56] K. Aziz and A. Settari, *Petroleum Reservoir Simulation*. Applied Science Publishers, 1979.
[57] T. T. Garipov, M. Karimi-Fard, and H. A. Tchelepi, "Discrete fracture model for coupled flow and geomechanics," *Comput. Geosci.*, vol. 20, no. 1, pp. 149–160, 2016.
[58] E. Ucar, E. Keilegavlen, I. Berre, and J. M. Nordbotten, "A finite-volume discretization for deformation of fractured media," *Comput. Geosci.*, vol. 22, no. 4, pp. 993–1007, 2018.
[59] M. W. McClure and R. N. Horne, "An investigation of stimulation mechanisms in Enhanced Geothermal Systems," *Int. J. Rock Mech. Min. Sci.*, vol. 72, pp. 242–260, 2014.
[60] O. Coussy, *Poromechanics*. Chichester, UK: John Wiley & Sons, Ltd, 2003.
[61] R. L. Berge, I. Berre, E. Keilegavlen, J. M. Nordbotten, and B. Wohlmuth, "Finite volume discretization for poroelastic media with fractures modeled by contact mechanics," *arXiv:1904.11916*, 2019.
[62] J. M. Nordbotten, "Convergence of a Cell-Centered Finite Volume Discretization for Linear Elasticity," *SIAM J. Numer. Anal.*, vol. 53, no. 6, pp. 2605–2625, 2015.
[63] J. M. Nordbotten, "Stable Cell-Centered Finite Volume Discretization for Biot Equations," *SIAM J. Numer. Anal.*, vol. 54, no. 2, pp. 942–968, 2016.
[64] E. Keilegavlen and J. M. Nordbotten, "Finite volume methods for elasticity with weak symmetry," *Int. J. Numer. Methods Eng.*, vol. 112, no. 8, pp. 939–962, 2017.
[65] S. Hüeber, G. Stadler, and B. I. Wohlmuth, "A Primal-Dual Active Set Algorithm for Three-Dimensional Contact Problems with Coulomb Friction," *SIAM J. Sci. Comput.*, vol. 30, no. 2, pp. 572–596, 2008.
[66] *PorePy implementation with runscripts. doi:10.5281/zenodo.3374624*. 2019.
[67] A. Fumagalli, E. Keilegavlen, and S. Scialò, "Conforming, non-conforming and non-matching discretization couplings in discrete fracture network simulations," *J. Comput. Phys.*, vol. 376, pp. 694–712, 2019.
[68] A. Fumagalli and E. Keilegavlen, "Dual Virtual Element Methods for Discrete Fracture Matrix models," *Oil Gas Sci. Technol. – Rev. D'IFP Energ. Nouv.*, vol. 74, p. 41, 2019.
[69] I. Stefansson, I. Berre, and E. Keilegavlen, "Finite-Volume Discretisations for Flow in Fractured Porous Media," *Transp. Porous Media*, vol. 124, no. 2, pp. 439–462, 2018.
[70] B. Flemisch *et al.*, "Benchmarks for single-phase flow in fractured porous media," *Adv. Water Resour.*, vol. 111, pp. 239–258, 2018.
[71] L. Formaggia, A. Fumagalli, A. Scotti, and P. Ruffo, "A reduced model for Darcy's problem in networks of fractures," *ESAIM Math. Model. Numer. Anal.*, vol. 48, no. 4, pp. 1089–1116, 2014.
[72] J. Mandel, "Consolidation des sols (étude mathématique)," *Geotechnique*, vol. 3, no. 7, pp. 287–299, 1953.
[73] Y. Abousleiman, A.-D. Cheng, L. Cui, E. Detournay, and J.-C. Rogiers, "Mandel's problem revisited," *Geotechnique*, vol. 46, no. 2, pp. 187–195, 1996.

[74] A. H.-D. Cheng and E. Detournay, “A direct boundary element method for plane strain poroelasticity,” *Int. J. Numer. Anal. Methods Geomech.*, vol. 12, no. 5, pp. 551–572, 1988.
[75] A. Mikelić, B. Wang, and M. F. Wheeler, “Numerical convergence study of iterative coupling for coupled flow and geomechanics,” *Comput. Geosci.*, vol. 18, no. 3–4, pp. 325–341, 2014.
[76] I. N. Sneddon, *Fourier transforms*. New York: Dover Publications, 1995.
[77] S. L. Crouch and A. M. Starfield, *Boundary element methods in solid mechanics: with applications in rock mechanics and geological engineering*. London ; Boston: Allen & Unwin, 1983.
[78] R. L. Berge, I. Berre, E. Keilegavlen, and J. M. Nordbotten, “Viscous fingering in fractured porous media,” *arXiv:1906.10472*, 2019.

Graphic design: Communication Division, UiB / Print: Skipnes Kommunikasjon AS

uib.no

ISBN: 9788230848593 (print)
9788230850527 (PDF)